COMPUTATIONAL STUDY OF LOW-FRICTION QUASICRYSTALLINE COATINGS VIA SIMULATIONS OF THIN FILM GROWTH OF HYDROCARBONS AND RARE GASES

by

Wahyu Setyawan

Department of Mechanical Engineering and Materials Science
Duke University

Date: _____
Approved:

_____
Dr. Stefano Curtarolo, Supervisor

_____
Dr. Teh Y. Tan

_____
Dr. Laurens E. Howle

_____
Dr. Xiaobai Sun

Dissertation submitted in partial fulfillment of the
requirements for the degree of Doctor of Philosophy
in the Department of Mechanical Engineering and Materials Science
in the Graduate School of
Duke University

2008

ABSTRACT

COMPUTATIONAL STUDY OF LOW-FRICTION QUASICRYSTALLINE COATINGS VIA SIMULATIONS OF THIN FILM GROWTH OF HYDROCARBONS AND RARE GASES

by

Wahyu Setyawan

Department of Mechanical Engineering and Materials Science
Duke University

Date: _____

Approved:

_____
Dr. Stefano Curtarolo, Supervisor

_____
Dr. Teh Y. Tan

_____
Dr. Laurens E. Howle

_____
Dr. Xiaobai Sun

An abstract of a dissertation submitted in partial fulfillment of the requirements for the degree of Doctor of Philosophy in the Department of Mechanical Engineering and Materials Science in the Graduate School of Duke University

2008

Abstract

Quasicrystalline compounds (QC) have been shown to have lower friction compared to other structures of the same constituents. The abscence of structural interlocking when two QC surfaces slide against one another yields the low friction. To use QC as low-friction coatings in combustion engines where hydrocarbon-based oil lubricant is commonly used, knowledge of how a film of lubricant forms on the coating is required. Any adsorbed films having non-quasicrystalline structure will reduce the self-lubricity of the coatings. In this manuscript, we report the results of simulations on thin films growth of selected hydrocarbons and rare gases on a decagonal $Al_{73}Ni_{10}Co_{17}$ quasicrystal (d-AlNiCo). Grand canonical Monte Carlo method is used to perform the simulations. We develop a set of classical interatomic many-body potentials which are based on the embedded-atom method to study the adsorption processes for hydrocarbons. Methane, propane, hexane, octane, and benzene are simulated and show complete wetting and layered films. Methane monolayer forms a pentagonal order commensurate with the d-AlNiCo. Propane forms disordered monolayer. Hexane and octane adsorb in a close-packed manner consistent with their bulk structure. The results of hexane and octane are expected to represent those of longer alkanes which constitute typical lubricants. Benzene monolayer has pentagonal order at low temperatures which transforms into triangular lattice at high temperatures. The effects of size mismatch and relative strength of the competing interactions (adsorbate-substrate and between adsorbates) on the film growth and structure are systematically studied using rare gases with Lennard-Jones pair potentials. It is found that the relative strength of the interactions determines the growth mode, while the structure of the film is affected mostly by the size mismatch between adsorbate and substrate's characteristic length. On d-AlNiCo, xenon monolayer un-

dergoes a first-order structural transition from quasiperiodic pentagonal to periodic triangular. Smaller gases such as Ne, Ar, Kr do not show such transition. A simple rule is proposed to predict the existence of the transition which will be useful in the search of the appropriate quasicrystalline coatings for certain oil lubricants.

Another part of this thesis is the calculation of phase diagram of Fe-Mo-C system under pressure for studying the effects of Mo on the thermodynamics of Fe:Mo nanoparticles as catalysts for growing single-walled carbon nanotubes (SWCNTs). Adding an appropriate amount of Mo to Fe particles avoids the formation of stable binary Fe_3C carbide that can terminate SWCNTs growth. Eventhough the formation of ternary carbides in Fe-Mo-C system might also reduce the activity of the catalyst, there are regions in the Fe:Mo which contain enough free Fe and excess carbon to yield nanotubes. Furthermore, the ternary carbides become stable at a smaller size of particle as compared to Fe_3C indicating that Fe:Mo particles can be used to grow smaller SWCNTs.

Contents

List of Figures

List of Tables

Acknowledgements

I would like to thank my advisor, Prof. Stefano Curtarolo for all the academic and financial supports. I wish to thank all collaborators of this work, Prof. Renee D. Diehl, Prof. Milton W. Cole, Prof. L W. Bruch, Dr. Nicola N. Ferralis, and Dr. Andrea Trasca. I thank all my teachers for their mentoring and my committee members, especially Prof. Teh Y. Tan, Prof. Laurens E. Howle, and Prof. Xiaobai Sun for their dedications and insightful advice. I thank all my colleagues, in particular Dr. Neha Awasthi, Dr. Aiqin Jiang, Dr. Roman Chepulskyy for encouragements and valuable discussions, and Dr. Aleksey Kolmogorov for his mentoring and experienced advice on VASP. I also wish to thank all the staff in the department of Mechanical Engineering and Materials Science for the administrative helps.

I thank the National Science Foundation and Honda Research Institute for funding this research. I also thank San Diego Super Computers (SDSC), Texas Advanced Computing Center (TACC), National Center for Supercomputing Applications (NCSA), and Pittsburgh Supercomputing Center (PSC) for all the computing time through Teragrid projects. Thanks also go to Duke Clusters for additional allocations.

I can never thank enough to my father whose talent in numbers has introduced me to math and engineering, my mother and my sisters for their endless prayers, love, and encouragements throughout my life. I am deeply grateful to be blessed with a brilliant, loving, and beautiful wife, Prof. Lisa M. Peloquin, who provides continuous prayers, love, and supports in so many ways. I also thank our friends especially Laura Heymann for her kind helps in many occassions. Thanks also go to Pepito, Clementine, Hamzah, John and other aquatic species for being excellent family members.

Finally, all praises are due to Allah, the Creator (al-Khaliq), the Loving (al-Rahman), and the All Knowing (al-Alim). I am thankful for all the opportunities, health, and blessings that enable me to finish this dissertation. I am deeply humbled by every piece of knowledge that I learned.

Chapter 1

Introduction

Quasicrystals (QCs) were discovered in 1982 by Dr. Shechtman during his X-ray measurements on Al-Mn compounds. Similar to crystals, QCs consist of atoms arranged in regular patterns having long-range order, i.e. the diffraction patterns show discrete spots. However, they do not have any translational periodicities. The discrete spots come from the rotational symmetries. A variety of stable and metastable QCs have been successfully synthesized. Among the first high-quality samples are icosahedral AlCuFe [1], decagonal AlNiCo [2], and icosahedral AlPdMn [3]. Today, hundreds of quasicrystalline phases are known, tens of which are stable [4]. The majority of them are derived from aluminum-transition metal family [5].

QCs have been shown to have lower coefficients of friction than most metals. For example, the static friction μ_s between two clean surfaces of icosahedral AlPdMn is ≈ 0.6 [6], whereas μ_s for Ni(110) and Cu(111) is ≈ 4 [7]. Kinetic friction tests using pin-on-disk technique with diamond pin show that among materials with comparable hardness included in the study, icosahedral AlPdMn exhibits the lowest friction ($\mu = 0.05$), compared to window glass ($\mu = 0.08$), sintered Al_2O_3 ($\mu = 0.13$), or hard Cr-steel ($\mu = 0.13$) [8]. Detailed measurements of friction as a function of structural perfection in icosahedral AlCuFe quasicrystal show that the minimum friction is achieved for sample with the best quasilattice perfection [9]. Decagonal AlNiCoSi has been verified to have lower friction than Cr_2O_3, which represents the most advanced technology for use on piston rings in automotive engines [10]. Further evidence of reduced friction is demonstrated in decagonal AlNiCo, in which the friction on the 2-fold periodic surface is eight times higher than that on the decagonal surface [11]

(Note that in decagonal quasicrystals, there is a direction along which the quasicrystalline surfaces are stacked periodically).

The reduced friction between two quasicrystalline surfaces can be understood by considering the structure commensurability between them. For surfaces with enough hardness, atoms can be regarded as fixed in their position in each material. Within this approximation, it has been theoretically demonstrated that the total interaction energy between the two surfaces is independent of their relative displacement parallel to the interface [12]. Therefore, the frictional force which is the gradient of the energy with respect to the displacement is vanishingly small, a phenomenon known as superlubricity [12]. Superlubricity has been observed experimentally between tungsten and graphite in which certain relative orientations result in nearly zero friction beyond the limit of the instruments [13]. Since any two QCs do not have common periodicities at any length scales, superlubricity is expected.

Another characteristic feature of QCs is their resistance to oxidation, which is quite surprising given that their main constituent, aluminum, is readily oxidized in ambient conditions [5]. The behavior is particularly spectacular in AlCuLi icosahedral phase that resists oxidation very well in humid air [5]. The combination of high hardness, oxidation resistance, and low friction has attracted interests in QCs as coatings to reduce friction and wear in machine parts, e.g. at the piston-cylinder interface and in gear boxes. In such environments, hydrocarbon-based oil lubricant is typically used to overcome the friction caused by surface asperities. Therefore, to yield a synergic performance of self-lubricating QC coating and lubricant, it is important to understand the interactions between them. The lubricant must be able to spread (wet) well on the QC. Furthermore, the structures of the thin film of lubricant formed on the sliding surfaces which will affect the lubricity need to be investigated.

In this work, we study the process of thin film growth of hydrocarbons and rare gases adsorbed on a decagonal $Al_{73}Ni_{10}Co_{17}$ quasicrystal (d-AlNiCo) via computer simulations. A high-quality and large-size single grain d-AlNiCo has been routinely grown, making it an excellent substrate to study adsorption [14, 15, 16]. Chapter 3 is devoted to the adsorptions of rare gases. The absence of chemical reactivity of noble gases will be utilized to elucidate the effects of quasicrytallinity of the substrate on the growth and structure of the adsorbed film. In Chapter 5, the simulation results for selected hydrocarbons are presented. We study the adsorption behaviors of propane, hexane, and octane. From these molecules, we may extrapolate the results for longer alkanes which constitute typical oil lubricants. In addition, methane and benzene are also studied due to their interesting symmetries.

We develop classical many-body interatomic potentials of Al, Ni, Co, C, and H which will be suitable for simulating hydrocarbons adsorptions on Al-Ni-Co involving thousands of atoms. To our knowledge, such potentials have not existed. The potentials are based on the embedded-atom method (EAM) [17] with parameters fitted to electronic energies of various structures evaluated via first principle quantum calculations. The generation of the EAM potentials is presented in Chapter 4. In Chapter 6, we extend the procedures to develop a consistent set of EAM potentials for pure elements in the periodic table. These potentials are also fitted to *ab initio* energies. A consistent set of EAM potentials having the same parametrizations enables one to use the same computer code for different potentials.

This manuscript contains a different reserach which is part of our doctoral work, namely in the field of nanocatalysis for synthesis of single-walled carbon nanotubes (SWCNTs). In Chapter 7, we present the calculation of phase diagram of Fe-Mo-C system under pressure for studying the effects of Mo in the thermodynamics of Fe:Mo nanoparticles as catalysts for growing SWCNTs. The decomposition of two

Fe:Mo particles namely FeMo and Fe_4Mo into various stable phases are analyzed. The implications of the formation of these phases to the growth of SWNCTs as well as the estimated minimum size of nanotubes that can be produced are discussed.

Chapter 2

Methods

2.1 Density functional theory

2.1.1 Born-Oppenheimer approximation

In a calculation of electronic structure of materials, one solves an eigenvalue problem of time-independent Schrödinger equation:

$$H\Psi(\mathbf{R},\mathbf{r}) = E\Psi(\mathbf{R},\mathbf{r}) \tag{2.1}$$

where $\mathbf{R} \in \{\mathbf{R}_n\}$ and $\mathbf{r} \in \{\mathbf{r}_i\}$ are the vector coordinates of the nuclei and electrons, respectively. The energy operator (Hamiltonian), H, is given by

$$H = -\sum_n \frac{\hbar^2}{2M_n}\nabla^2_{\mathbf{R}_n} - \sum_i \frac{\hbar^2}{2m_i}\nabla^2_{\mathbf{r}_i} + \sum_{m<n} \frac{e^2 Z_m Z_n}{|\mathbf{R}_n - \mathbf{R}_m|} + \sum_{i<j} \frac{e^2}{|\mathbf{r}_j - \mathbf{r}_i|} - \sum_{n,i} \frac{e^2 Z_n}{|\mathbf{r}_i - \mathbf{R}_n|} \tag{2.2}$$

The first two terms represent the kinetic energies of the nuclei and the electrons, respectively. The third and fourth terms represent the nucleus-nucleus and electron-electron potential energies. The last term is the nucleus-electron energy. It is computationally beyond the capability of current computers to solve Equation 2.1 using the full Hamiltonian. An approximation, known as Born-Oppenheimer approximation, is made by realizing that nuclei are significantly heavier than electrons so the nuclei move much more slowly than the electrons. The electrons can adapt themselves to the current configuration of nuclei. Using this approximation, we can decouple the electronic and the ionic parts of the Hamiltonian. Consider the nuclei fixed at a given

configuration, α, and solve the following electronic Schrödinger equation:

$$\left[-\sum_i \frac{\hbar^2}{2m_i}\nabla^2_{\mathbf{r}_i} + \sum_{i<j}\frac{e^2}{|\mathbf{r}_j - \mathbf{r}_i|} - \sum_{n,i}\frac{e^2 Z_n}{|\mathbf{r}_i - \mathbf{R}^\alpha_n|}\right]\psi^\alpha(\mathbf{r}) = E^\alpha(\mathbf{R})\psi^\alpha(\mathbf{r}) \tag{2.3}$$

The total energy, E, is calculated by taking the electronic contribution, $E^\alpha(\mathbf{R})$, as a potential energy operator in the ionic Schrödinger equation:

$$\left[-\sum_n \frac{\hbar^2}{2M_n}\nabla^2_{\mathbf{R}_i} + \sum_{m<n}\frac{e^2 Z_m Z_n}{|\mathbf{R}_m - \mathbf{R}_n|} + E^\alpha(\mathbf{R})\right]\Phi^\alpha(\mathbf{R}) = E\Phi^\alpha(\mathbf{R}) \tag{2.4}$$

Mostly, one is interested only in the electronic part, i.e. Equation 2.3. Even though Equation 2.3 contains only the electronic part of the system, the large number of variables (e.g. coordinates of all electrons) makes it remain intractable. In addition, it is the electron-electron interaction that makes the problem so difficult to solve. This interaction is a result of correlation between electrons (the probability of finding an electron depends on where the rest of the electrons are) and the fact that electrons are fermions requiring antisymmetric wavefunctions (the many-electron wavefunction gains a factor of -1 everytime two electrons exchange their coordinates). If this term were absent, the Hamiltonian would be just a sum of many one-electron Hamiltonians, known as independent electron approximation.

2.1.2 Slater determinant

An antisymmetric N-electron wavefunction can be constructed from N one-electron wavefunctions using Slater determinant [18] defined as:

$$\Psi(\mathbf{x}_1, \mathbf{x}_2, \ldots, \mathbf{x}_N) = \frac{1}{\sqrt{N!}}\begin{vmatrix} \psi_1(\mathbf{x}_1) & \psi_2(\mathbf{x}_1) & \ldots & \psi_N(\mathbf{x}_1) \\ \psi_1(\mathbf{x}_2) & \psi_2(\mathbf{x}_2) & \ldots & \psi_N(\mathbf{x}_2) \\ \ldots & \ldots & \ldots & \ldots \\ \psi_1(\mathbf{x}_N) & \psi_2(\mathbf{x}_N) & \ldots & \psi_N(\mathbf{x}_N) \end{vmatrix} \tag{2.5}$$

where $\psi_k(\mathbf{x}_i)$ denotes the k-th one-electron wavefunction being occupied by an electron with spin-orbital coordinate $\mathbf{x}_i = (s_i, \mathbf{r}_i)$, with s_i being the spin state and $\mathbf{r}_i$ the spatial coordinate. For this reason, ψ_k is also called the spin-orbital k. The factor $\frac{1}{\sqrt{N!}}$ arrives from the normalization of the total wavefunction and orthonormality among the spin orbitals:

$$\int \Psi\Psi^* d\mathbf{x}_1 \dots d\mathbf{x}_N = 1 \tag{2.6}$$

$$\int \psi_k(\mathbf{r})\psi_k^*(\mathbf{r})d\mathbf{r} = 1 \tag{2.7}$$

$$\int \psi_k(\mathbf{r})\psi_l^*(\mathbf{r})d\mathbf{r} = 0 \tag{2.8}$$

Using the orthonormality of the spin-orbitals, it can be shown that the charge density of the Slater determinant can be written as $n(\mathbf{x}) = \sum_k |\psi_k(\mathbf{x})|^2$.

2.1.3 Hartree-Fock equations

In the electronic Schrödinger equation (Equation 2.3), the Hamiltonian can be written as follows:

$$H = \sum_i h(i) + \frac{1}{2}\sum_{i \neq j} g(i,j) \tag{2.9}$$

$$h(i) \equiv -\frac{1}{2}\nabla_i^2 - \sum_n \frac{Z_n}{|\mathbf{r}_i - \mathbf{R}_n|} \tag{2.10}$$

$$g(i,j) \equiv \frac{1}{|\mathbf{r}_j - \mathbf{r}_j|} \tag{2.11}$$

where $h(i)$ depends only on $\mathbf{r}_i$ and $g(i,j)$ depends on $\mathbf{r}_i$ and $\mathbf{r}_j$. The energy of the system is calculated by taking the expectation value of the Hamiltonian in the total wavefunction, $E = \langle\Psi|H|\Psi\rangle$. By employing the orthonormality of ψ_k as in the

calculation of charge density $n(\mathbf{x})$, we have

$$\langle\Psi|\sum_i h(i)|\Psi\rangle = \sum_k \langle\psi_k|h|\psi_k\rangle = \sum_k \int d\mathbf{x}\psi_k^*(\mathbf{x})h(\mathbf{r})\psi_k(\mathbf{x}) \tag{2.12}$$

Note that in the first equation, when $|\Psi\rangle$ is written as a Slater determinant, only $i = k$ appears due to orthonormality of ψ_k, and the summation over electron index i inside the many-electron wavefunction $|\Psi\rangle$ becomes a summation over k inside individual spin-orbital ψ_k, and we can drop the index $h(i = k)$ for convenience. The integral $\int d\mathbf{x}$ denotes integral over spatial coordinates and a sum over the spin-degrees of freedom. Similarly, we have

$$\langle\Psi|\sum_{i,j} g(i,j)|\Psi\rangle = \sum_{k,l}\langle\psi_k\psi_l|g|\psi_k\psi_l\rangle - \sum_{k,l}\langle\psi_k\psi_l|g|\psi_l\psi_k\rangle \tag{2.13}$$

$$\langle\psi_k\psi_l|g|\psi_m\psi_n\rangle = \int d\mathbf{x}_1\psi_k^*(\mathbf{x}_1)\left[\int d\mathbf{x}_2\psi_l^*(\mathbf{x}_2)\frac{1}{|\mathbf{r}_1-\mathbf{r}_2|}\psi_n(\mathbf{x}_2)\right]\psi_m(\mathbf{x}_1) \tag{2.14}$$

The total energy is then

$$E = \sum_k\langle\psi_k|h|\psi_k\rangle + \frac{1}{2}\sum_{k,l}\left[\langle\psi_k\psi_l|g|\psi_k\psi_l\rangle - \langle\psi_k\psi_l|g|\psi_l\psi_k\rangle\right] \tag{2.15}$$

This expression shows that the electron-electron interaction, $g(i,j)$, consists of two terms, the first one is known as Coulomb energy (or Hartree term), and the second one is the exchange energy term. To see how this derivation also reduces the many-electron Schrödinger equation to a set of one-electron equations, we differentiate the energy with respect to a particular spin-orbital, e.g. spin-orbital $\langle\psi_i|$. Note that i is not electron index, but a specific value of spin-orbital index k, after the derivation,

we may replace i by k to conform to the usual notation:

$$\frac{\delta E}{\delta\langle\psi_i|} = h|\psi_i\rangle + \frac{1}{2}\left[\sum_l \langle\psi_l|\frac{1}{|\mathbf{r}-\mathbf{r}'|}|\psi_l\rangle\right]|\psi_i\rangle + \frac{1}{2}\left[\sum_k \langle\psi_k|\frac{1}{|\mathbf{r}-\mathbf{r}'|}|\psi_k\rangle\right]|\psi_i\rangle$$
$$-\frac{1}{2}\sum_l \int d\mathbf{x}'\psi_l^*(\mathbf{x}')\frac{1}{|\mathbf{r}-\mathbf{r}'|}\psi_l(\mathbf{x})\psi_i(\mathbf{x}') - \frac{1}{2}\sum_k \int d\mathbf{x}\psi_k^*(\mathbf{x}')\frac{1}{|\mathbf{r}-\mathbf{r}'|}\psi_i(\mathbf{x})\psi_k(\mathbf{x}') \tag{2.16}$$

By changing indices ($k \to l$) in the third term and ($k \to l, \mathbf{x} \to \mathbf{x}'$) in the last term, we get

$$\frac{\delta E}{\delta\langle\psi_i|} = h|\psi_i\rangle + \left[\sum_l \langle\psi_l|\frac{1}{|\mathbf{r}-\mathbf{r}'|}|\psi_l\rangle\right]|\psi_i\rangle - \sum_l \int d\mathbf{x}'\psi_l^*(\mathbf{x}')\frac{1}{|\mathbf{r}-\mathbf{r}'|}\psi_l(\mathbf{x})\psi_i(\mathbf{x}') \tag{2.17}$$

This expression is known as Fock operator acting on $|\psi_i\rangle$. Replacing back i by k, and defining the eigenvalues of Fock operator as ϵ_k, we arrive at the Hartree-Fock equation:

$$H_{HF}\psi_k = \epsilon_k\psi_k \tag{2.18}$$

$$H_{HF}\psi_k = \left[-\frac{\nabla^2}{2} - \sum_n \frac{Z_n}{|\mathbf{r}-\mathbf{R}_n|}\right]\psi_k(\mathbf{x}) + \sum_l \int d\mathbf{x}'\psi_l^*(\mathbf{x}')\frac{1}{|\mathbf{r}-\mathbf{r}'|}\psi_l(\mathbf{x}')\psi_k(\mathbf{x})$$
$$-\sum_l \int d\mathbf{x}'\psi_l^*(\mathbf{x}')\frac{1}{|\mathbf{r}-\mathbf{r}'|}\psi_k(\mathbf{x}')\psi_l(\mathbf{x}) \tag{2.19}$$

Note that the sum of the eigenvalues ϵ_k is not the total energy E. However, by comparing Equation 2.15 and 2.19, E can be recovered using the following equation

$$E = \frac{1}{2}\sum_k \left[\epsilon_k + \langle\psi_k|h|\psi_k\rangle\right] \tag{2.20}$$

The last term (the exchange term) in Equation 2.19 is nonlocal because the Hamiltonian H_{HF} operates on $\psi_k(\mathbf{x})$ at a particular $\mathbf{x}$, but the operator itself is a function

of $\psi_k(\mathbf{x}')$ at all possible $\mathbf{x}'$. This nonlocality makes the Hartree-Fock Hamiltonian difficult to evaluate in large systems involving many atoms and electrons, hence not suitable for solids. Most electronic structure calculations for solids are based on density functional theory (DFT) discussed in the following sections.

2.1.4 Kohn-Sham equations

In DFT, the nonlocal exchange term is given by an effective exchange potential that depends on electronic charge density. Furthermore, all other potential operators are expressed in charge density rather than in spin-orbitals. This approach reduces the number of degrees of freedom significantly since all electron coordinates that enter in the spin-orbitals are now replaced by charge density that is a function only on one coordinate $\mathbf{r}$. The DFT energy functional is given by

$$E(n) = T(n) + \int V_{ext}(\mathbf{r})n(\mathbf{r})d\mathbf{r} + \frac{1}{2}\iint n(\mathbf{r}')\frac{1}{|\mathbf{r}-\mathbf{r}'|}n(\mathbf{r})d\mathbf{r}'d\mathbf{r} + E_{xc}(n) \tag{2.21}$$

where T being the electronic kinetic energy and V_{ext} being the electron-nuclei electrostatic potential. We know that for given wavefunctions we can calculate the charge density, $n(\mathbf{r}) = \sum_k |\psi_k(\mathbf{r})|^2$, however the reverse is not obvious. The formality that proves there exists one-to-one mapping between charge density and wavefunctions was developed by Hohenberg-Kohn [19]. Hohenberg-Kohn theorem also proves that there exists $E_{xc}(n)$ that will produce the exact ground state of the system. The DFT Schrödinger equation can be derived by taking the variation of $E(n)$ with respect to n:

$$\frac{\delta E}{\delta n} = \frac{\delta T}{\delta n} + V_{ext} + \int \frac{n(\mathbf{r}')d\mathbf{r}'}{|\mathbf{r}-\mathbf{r}'|} + \frac{\delta E_{xc}}{\delta n} \tag{2.22}$$

As we have derived the Hartree-Fock equation (Equation 2.19), if we write the DFT many-electron wavefunction as a Slater determinant of spin-orbitals and orthonor-

mality among the spin-orbitals, then each DFT spin-orbital equation satisfies

$$\left[-\frac{1}{2}\nabla^2 + V_{eff}(\mathbf{r})\right]\psi_k(\mathbf{r}) = \epsilon_k\psi_k(\mathbf{r}) \tag{2.23}$$

$$V_{eff}(\mathbf{r}) \equiv V_{ext}(\mathbf{r}) + \int \frac{n(\mathbf{r}')d\mathbf{r}'}{|\mathbf{r}-\mathbf{r}'|} + \frac{\delta E_{xc}}{\delta n} \tag{2.24}$$

The total energy is related to the eigenvalues ϵ_k as follows

$$E = \sum_k \epsilon_k - \frac{1}{2}\iint n(\mathbf{r}')\frac{1}{|\mathbf{r}-\mathbf{r}'|}n(\mathbf{r})d\mathbf{r}'d\mathbf{r} + E_{xc}(n) - \int \frac{\delta E_{xc}(n)}{\delta n}n(\mathbf{r})d\mathbf{r} \tag{2.25}$$

Equations 2.24-2.25 are known as Kohn-Sham equations. Since the potential operators depend on charge density, Equation 2.24 must be solved self-consistently. One starts from a trial electronic charge density to construct the potentials and solve for the eigenvalues and spin-orbitals wavefunctions. A new charge density is then constructed from the spin-orbitals and the procedure is repeated until the charge and the wavefunctions are self-consistent within a certain accuracy.

2.1.5 Local density and generalized gradient approximations

In Kohn-Sham equations, there are two terms involving exchange interaction, namely $E_{xc}(n)$ and $\delta E_{xc}/\delta n$. For a given charge density, the first term (the exchange energy) does not depend on the charge functional on $\mathbf{r}$, whereas the second term (the exchange potential) will depend on $\mathbf{r}$ if the charge density does. This means that for a nonhomogeneous systems, exchange potential can be expanded in charge density and its derivatives:

$$V_{xc} \equiv \frac{\delta E_{xc}(n)}{\delta n(\mathbf{r})} = V_{xc}(n(\mathbf{r}), |\nabla n(\mathbf{r})|, |\nabla(\nabla(n(\mathbf{r})))|, ...) \tag{2.26}$$

As a first approximation, one neglects all the gradients of charge density in the exchange potential, this is known as local density approximation (LDA) since the

exchange potential depends on charge density only at a particular value of $\mathbf{r}$. It means that LDA gives an exact ground state for homogeneous electron gas since in this case the gradients vanish. This allows one to write the LDA exchange energy as a sum of exchange energy per electron in a homogeneous electron gas, $\epsilon_{xc}^{hom}(n)$:

$$E_{xc}^{LDA} = \int \epsilon_{xc}^{hom}(n) n d\mathbf{r} \tag{2.27}$$

LDA also gives accurate results for systems where the charge density does not vary too rapidly such as in metals. For nonhomogenous systems such as transition metals, semiconductors, or slabs, LDA is known to underestimate the energy (hence the band gap). A more accurate approximation, known as generalized gradient approximation (GGA), includes the first gradient of charge and the exchange energy is given by

$$E_{xc}^{GGA} = \int \epsilon_{xc}^{GGA}(n(\mathbf{r}), |\nabla n(\mathbf{r})|) n(\mathbf{r}) d\mathbf{r} \tag{2.28}$$

Several techniques exist to parametrize ϵ_{xc}^{GGA}: Perdew-Wang 1986 (PW86) [20, 21], Perdew-Wang 1991 (PW91) [22], Becke [23], Lee-Yang-Parr (LYP) [24], and Perdew-Burke-Enzerhof (PBE) [25, 26]. In this work, we use GGA-PBE functional for the exchange energy.

2.1.6 Pseudopotentials

Kohn-Sham equations can be solved in different ways depending on the choice of potentials and basis functions to expand the wavefunctions. Some considerations in solving the Kohn-Sham equations are: (1) potentials becomes very strong near the nuclei, whereas at far regions they are relatively weak, (2) wavefunctions fluctuate more near nuclei than in the interstitial regions, (3) the symmetry of the potentials are approximately spherical near the nuclei whereas at larger distances, the symmetry of the crystal dominates. Some of the known methods are augmented plave wave (APW)

[27, 28], linearized augmented plane wave (LAPW) [29, 30], Orthogonalized plave-wave (OPW) [31], and pseudopotential method [32, 33]. LAPW is the most accurate method available. It uses spherical harmonics to expand the wavefunctions in the core region near the nuclei and plane waves for the interstitial region. Pseudopotential methods use only plane wave basis set. The number of plane waves can be kept small by treating an atom as consisting of an effective core (nucleus + core electrons) and valence electrons. Even though pseudopotentials are not as accurate as LAPW (which as a contrast fall into the class of fullpotential methods), it provides good results and becomes the most common choice for its lower computational costs than LAPW.

2.2 Vienna Ab initio Simulation Package

All *ab initio* quantum calculations in this work are done using Vienna Ab initio Simulation Package (VASP) [34, 35]. The calculations are performed in the generalized gradient approximation (GGA) [36, 37] with exchange correlation as parametrized by Perdew, Burke, and Ernzerhof (PBE) [25]. To reduce the number of plane waves, projector augmented-wave (PAW) pseudopotentials are used [38, 39].

VASP uses a plane wave basis set to expand the wave functions in solving the Kohn-Sham equation in reciprocal space. The evaluation of total electronic energy per unit cell is done by integrating the energy of all electronic states in the Brillouin zone. In practice, the Brillouin zone is divided into grids and the integration is replaced by a sum over k-points. In our work, the k-point grids are generated automatically using Monkhorst-Pack scheme [40]. For hexagonal structures, an additional shift is used so that the grids are centered at the Γ point ($\mathbf{k} = (0, 0, 0)$). Typical setting of the number of k-points as many as 3000/number-of-atoms is usually sufficient to achieve a converged energy with an accuracy better than 10 meV/atom. Unless otherwise

stated, all structures are fully relaxed: atoms position as well as unit cell's size and shape are allowed to relax to find the equillibrium configurations.

2.3 Classical interatomic potentials

Due to QC's lack of periodicity, a large enough simulation cell is necessary to capture the effect of substrate's structure on the adsorbed films. A typical cell contains thousands of atoms which makes the simulation unpractical to be performed quantum-mechanically. Therefore, classical interatomic potentials are needed. For simple systems, e.g. adsorption of noble gases, pair potentials such as Lennard-Jones [41] or Morse [42] are sufficient. However, for complex systems, such as adsorption of hydrocarbons, more accurate potentials are required to take into account many-body effects in these systems, especially covalent bonds involving carbons which are higly directional.

Several methods exist to incorporate many-body interations into classical potentials, e.g. force field method (FF) [43, 44, 45, 46], Cluster Expansion method (CE) [47, 48, 49], and embedded-atom method (EAM) [17, 50]. FF is based on energy-bond order-bond length relationship [44] and is mostly used for biological systems [43, 51] and chemical systems where bond formation and breaking are allowed [46]. In CE, energy of a system is approximated by a converging sum over cluster contributions, where contribution from large clusters are negligible. In nonperiodic systems, such as amorphous and quasicrystalline phases, the number of clusters needed can be large to reach the desired accuracy, therefore CE is mostly suitable to evaluate ground state energy in periodic systems. EAM is based on the close relationship between electronic charge density and energy of the system. In quantum physics, this relationship becomes the basis for the density functional theory (DFT) [52, 19, 53], in which it has been proven that there exists a one-to-one mapping between charge densities

and electronic wave functions, and hence energies [19]. Due to the universality of charge density, in principle EAM can be used in any systems.

EAM was originally developed for examining metallic bulks and surfaces [17, 50]. Later on, charge screening methods have been proposed to modify EAM for use in covalent systems such as Si [54] and Ge [55]. EAM has been successfully employed to simulate surface relaxation/reconstructions [56, 57, 58, 59], film growth [60, 61], and diffusion processes [62, 63]. In this study, we will develop EAM potentials to simulate hydrocarbons adsorption on d-AlNiCo surface.

In EAM formalism [17, 50], each atom is viewed as being embedded in the material consisting of all other atoms. The total energy of a system is defined by

$$E_{tot} \equiv \sum_i F_i(\bar{\rho}_i) + \frac{1}{2}\sum_i \sum_{j \neq i} \phi_{ij}(r_{ij}), \tag{2.29}$$

where F_i is the embedding energy of atom i, $\bar{\rho}_i$ is the electron density at the vector position $\mathbf{r}_i$, ϕ_{ij} is the pair potential, and r_{ij} is the distance between atoms i and j. If $\bar{\rho}_i$ is approximated as a sum of individual contribution of the constituents [i.e., $\bar{\rho}_i = \sum_{j \neq i} \rho_j(r_{ij})$, where ρ_j is the atomic electron density of atom j, the energy is then only a function of the position of atoms.

For an elemental potential, there are 3 functions needed: $F(\bar{\rho})$, $\rho(r)$, and $\phi(r)$. For a binary system AB, we will need 7 functions: $F^A(\bar{\rho})$, $\rho^A(r)$, $\phi^A(r)$, $F^B(\bar{\rho})$, $\rho^B(r)$, $\phi^B(r)$, and a cross-pair potential $\phi^{AB}(r)$. The cross-pair potential is needed to calculate pair interaction of atoms of different types. In general, in a system consisting of N different elements, we need $N(N+5)/2$ functions.

We will use the following functional forms:

$$\rho^A(r) = \rho_e^A e^{-\beta^A(r/r_e^A - 1)}, \tag{2.30}$$

$$\phi^{AA}(r) = D^A[e^{-2\alpha^A(r-r_0^A)} - 2e^{-\alpha^A(r-r_0^A)}], \tag{2.31}$$

$$F^A(\bar{\rho}) = cubic - splines, \tag{2.32}$$

$$\phi^{AB}(r) = \frac{\gamma^{AB}}{2}\phi^{AA}(r) + \frac{1}{2\gamma^{AB}}\phi^{BB}(r). \tag{2.33}$$

In the above equations, A and B denote atom type. ρ_e, r_e, and β will be taken from the database of atomic electron density [64]. Equation 2.31 follows Morse potential form [42]. The embedding function F will be taken as a natural cubic spline [65]. The expression for the cross-pair interaction ϕ^{AB} follows Haftel's derivation [59] in which $\gamma^{AB} \equiv Z^B/Z^A$ (Z^A is the effective charge of the core for atom type A).

2.4 Simplex method

The EAM potentials parameters need to be fit to quantum calculations. The fitting will be performed using simplex method [66]. Simplex does not require evaluation of function derivatives which makes it simple to implement. Simplex minimizes N-dimensional function f by creating $P > N$ simplex points. A simplex point is f evaluated at a given coordinate. The simplex points will form P-polytope. A minimization move is made by replacing the maximum simplex point, hence the worst, with a point reflected through the centroid of the remaining $(P-1)$-polytope. Expansion or shrinking of the polytope are allowed to overcome some local minima or to converge, respectively.

2.5 Grand canonical Monte Carlo

The adsorption simulation will be performed using grand canonical Monte Carlo (GCMC) method [67, 68, 69]. At constant temperature, T, and volume, V, the GCMC method explores the configurational phase space using the Metropolis algorithm and finds the equilibrium number of adsorbed atoms (adatoms), N, as a function of the chemical potential, μ, of the gas, i.e. configuration(μ, N, V). The adsorbed atoms are in equilibrium with the coexisting gas: the chemical potential of the gas is constant throughout the system. In addition, the coexisting gas is taken to be ideal. With this method we determine adsorption isotherms, ρ_N, and density profiles, $\rho(x, y)$, as a function of the pressure, $P(T, \mu)$. For each data point in an isotherm, we perform at least 18 million GCMC steps to reach equilibrium. Each step is an attempted displacement, creation, or deletion of an atom with execution probabilities equal to 0.2, 0.4, and 0.4, respectively [70, 71, 72]. At least 27 million steps are performed in the subsequent data-gathering and -averaging phase.

Chapter 3

Noble gas adsorptions on d-AlNiCo

The observed unusual electronic [73, 74] and frictional [75, 76, 77] properties of quasicrystal surfaces stimulate interesting fundamental questions about how these and other physical properties are altered by quasiperiodicity. Recent progress in the characterization and preparation of quasicrystal surfaces raises new possibilities for their use as substrates in the growth of films having novel structural, electronic, dynamic and mechanical properties [78, 79, 80]. The physical behavior of systems involving competing interactions in adsorption is a subject of continuing interest and is particularly relevant to the growth of thin films [69]. Several different growth modes have been observed for the growth of metal films on quasicrystals [81, 82, 83, 84]. A form of competing interactions seen in adsorption involves either a length scale or a symmetry mismatch between the adsorbate-adsorbate interaction and the adsorbate-substrate interaction [85, 86]. Some consequences of such mismatches include density modulations [87, 88], domain walls [89], epitaxial rotation in the adsorbed layer [90, 91, 92, 93, 94, 95], and a disruption of the normal periodicity and growth in the film [96, 97, 98].

The wide range of behavior observed so far indicates that, even in the absence of intermixing, film growth is strongly affected by chemical interactions between adsorbate and substrate. In order to separate these chemical effects from those specific to quasiperiodic order, we have studied the adsorption of noble gases on a quasicrystal surface, where both the gas-gas and gas-surface interactions are believed to be simple, i.e., appreciable chemical interactions and adsorbate-induced surface reconstructions are absent. In this chapter, we explore the implications of structural mismatch by

evaluating the nature of Ne, Ar, Kr, and Xe adsorption on a quasicrystal substrate, namely the 10-fold surface of decagonal $Al_{73}Ni_{10}Co_{17}$ quasicrystal (d-AlNiCo QC) [15, 16].

3.1 Method

3.1.1 Simulation cell

The simulation cell is tetragonal. We take a square section of the surface, A, of side 5.12 nm, to be the (x, y) part of the unit cell in the simulation, for which we assume periodic boundary conditions along the basal directions. Although this assumption limits the accuracy of the long range QC structure, it is numerically necessary for these simulations. To minimize the long range interaction corrections, a relatively large cutoff ($5\sigma_{gg}$) is used. Since the size of the cell is relatively large compared to that of the noble gases, the cell is accurately representative of order on short-to-moderate length scales. The height of the cell, along the z (surface-normal) direction, is chosen to be 10 nm (long enough to contain ∼20 layers of Xe). At the top of the cell, a hard-wall reflective potential is employed to confine the coexisting vapor phase. The simulation results for Xe over d-AlNiCo, presented below, are consistent with both our results from experiments [99] and virial calculations [100]. Hence, the calculations may also be accurate for other systems.

3.1.2 Gas-gas and gas-substrate interactions

The gas-gas and gas-substrate interactions are modeled using Lennard-Jones (LJ) 12-6 potentials, with the gas-gas parameter values ϵ_{gg} and σ_{gg} listed in Table 3.1. The gas-substrate interactions are obtained by summing pair potentials for a gas atom and all of the substrate atoms in an eigth-layer slab: Al, Ni and Co [15, 101, 100]. The position of the atoms in the eight-layer slab are taken from the results of a low-energy

Table 3.1: Parameter values for the 12-6 Lennard-Jones interactions. TM is the label for Ni or Co.

	ϵ_{gg} (meV)	σ_{gg} (nm)	ϵ_{gas-Al} (meV)	σ_{gas-Al} (nm)	ϵ_{gas-TM} (meV)	σ_{gas-TM} (nm)
Ne	2.92	0.278	9.40	0.264	9.01	0.249
Ar	10.32	0.340	17.67	0.295	16.93	0.280
Kr	14.73	0.360	21.11	0.305	20.23	0.290
Xe	19.04	0.410	24.00	0.330	23.00	0.315
iNe$^{(1)}$	2.92	0.410	5.45	0.330	5.22	0.315
dXe$^{(1)}$	19.04	0.278	41.39	0.264	39.67	0.249
dXe$^{(2)}$	19.04	0.390	25.88	0.320	24.80	0.305
iXe$^{(1)}$	19.04	0.550	14.96	0.400	14.34	0.385
iXe$^{(2)}$	19.04	0.675	10.52	0.462	10.08	0.447

electron diffraction LEED analysis of the surface structure of d-AlNiCo [15]. The gas-substrate interaction parameters are derived using conventional combining rules, $\sigma_{AB} = (\sigma_A + \sigma_B)/2$ and $\epsilon_{AB} = \sqrt{\epsilon_A \epsilon_B}$ [102], and experimental heats of adsorption [100, 99, 103]. The LJ gas-substrate parameters are ϵ_{gas-Al} and σ_{gas-Al} for Al, and ϵ_{gas-TM} and σ_{gas-TM} for the two transition metals Ni and Co. All these values are listed in the upper part of Table 3.1. In the calculation of the adsorption potential, we assume a structure of the unrelaxed surface taken from the empirical fit to LEED data [16].

3.1.3 Adsorption potentials

Figures 3.1(a), 3.1(c), 3.1(e), and 3.1(g) show the function $V_{min}(x, y)$ of Ne, Ar, Kr, and Xe on the d-AlNiCo, respectively, which is calculated by minimizing the adsorption potentials, $V(x, y, z)$, along the z direction at every value (x, y) coordinates:

$$V_{min}(x, y) \equiv min \left\{ V(x, y, z) \right\} \big|_{along\ z} . \tag{3.1}$$

The figures reveal the fivefold rotational symmetry of the substrate. Dark spots correspond to the most attractive regions of the substrate. By choosing appropriate sets of five dark spots, we can identify pentagons, whose sizes follow the inflationary property of the d-AlNiCo. Note the pentagon at the center of each figure: it will be used to extract the geometrical parameters λ_s and λ_c in Section 3.2.5.

To characterize the corrugation, not well-defined for aperiodic surfaces, we calculate the distribution function $f(V_{min})$, the average $\langle V_{min} \rangle$ and standard deviation SD of $V_{min}(x, y)$ as:

$$f(V_{min})dV_{min} \equiv probability\left\{ V_{min} \in [V_{min}, V_{min} + dV_{min}[\right\} \tag{3.2}$$

$$\langle V_{min} \rangle \equiv \int_{-\infty}^{\infty} f(V_{min}) V_{min}\, dV_{min}, \tag{3.3}$$

$$SD^2 \equiv \int_{-\infty}^{\infty} f(V_{min})(V_{min} - \langle V_{min} \rangle)^2\, dV_{min}. \tag{3.4}$$

Figures 3.1(b), 3.1(d), 3.1(f), and 3.1(h) show $f(V_{min})$ of the adsorption potential for Ne, Ar, Kr, and Xe on the d-AlNiCo, respectively. $V_{min}(x, y)$ extends by more than 2·SD around its average, revealing the high corrugation of the gas-surface interaction in these four systems. The average and SD of $V_{min}(x, y)$ for these systems are listed in the upper part of Table 3.2. In addition to highly corrugated, the potentials are "deep" because the record maximum well-depth, e.g. for Xe, on a periodic surface is about 160 meV, viz. on graphite [104]; and the record minimum well-depth is about 28 meV, on Cs [105].

3.1.4 Effective parameters

For every gas-substrate interaction we define two effective parameters σ_{gs} and D_{gs}. σ_{gs} represents the averaged LJ size parameter of the interaction, calculated following

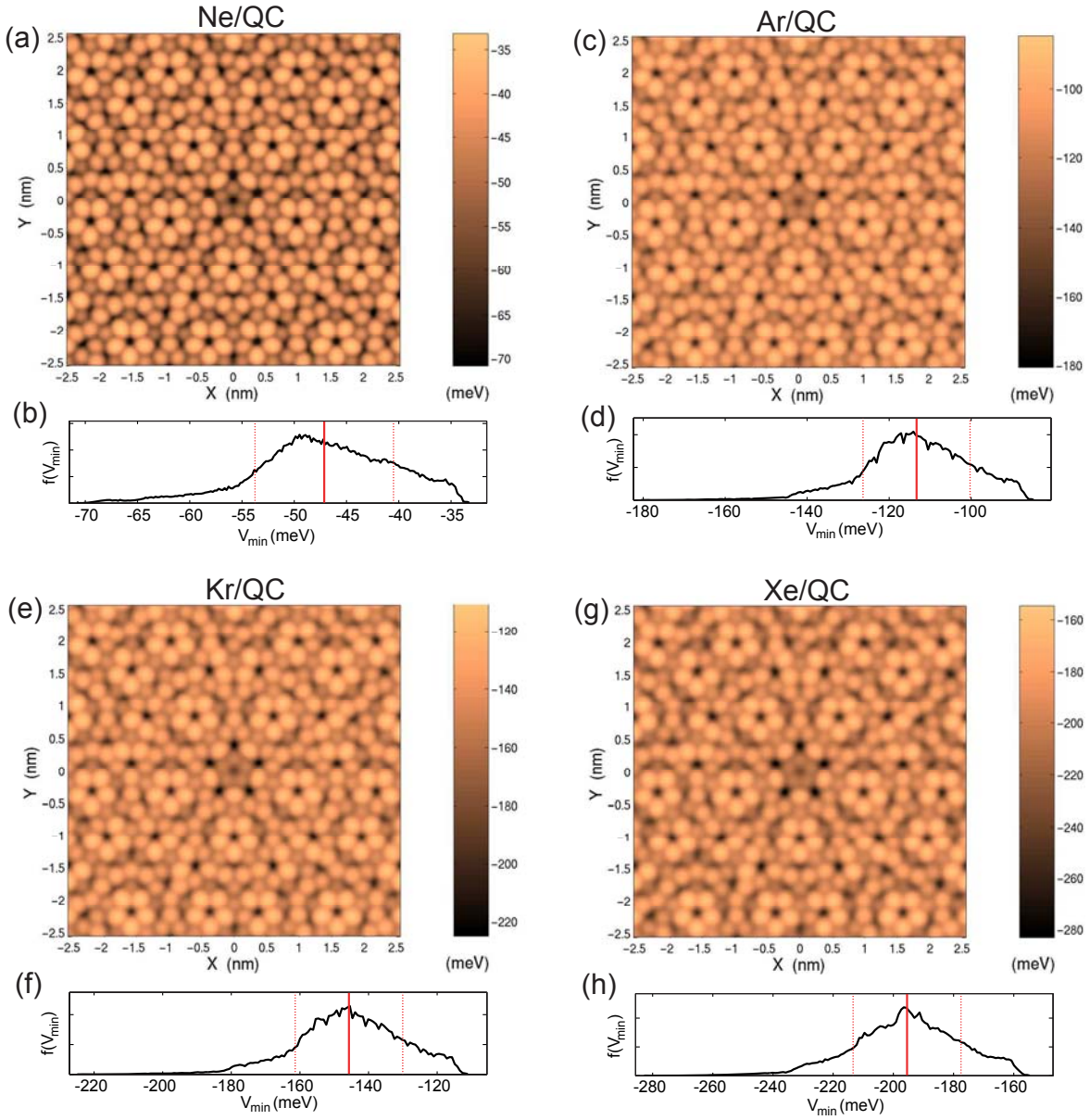

Figure 3.1: (color online). Computed adsorption potentials for (a) Ne, (c) Ar, (e) Kr, and (g) Xe on the d-AlNiCo, obtained by minimizing $V(x, y, z)$ with respect to z. The distribution of the minimum value of these potentials is plotted in (b, d, f, and h) respectively: the solid line marks the average value $\langle V_{min} \rangle$, the dashed lines mark the values at $\langle V_{min} \rangle \pm$SD.

Table 3.2: Range, average ($\langle V_{min} \rangle$), and standard deviation (SD) of the interaction $V_{min}(x.y)$ on the d-AlNiCo. Effective parameters of the gas-substrate interactions (D_{gs}, σ_{gs}, $D^{\star}_{gs}$, $\sigma^{\star}_{gs}$), and, for comparison, the best estimated well depths D^{Gr}_{gs} on graphite [106].

	V_{min} range (meV)	$< V_{min} >$ (meV)	SD (meV)	D_{gs} (meV)	σ_{gs} (nm)	$D^{\star}_{gs}$ (D_{gs}/ϵ_{gg})	$\sigma^{\star}_{gs}$ (σ_{gs}/σ_{gg})	D^{Gr}_{gs} (meV)
Ne	-71 to -33	-47.43	6.63	43.89	0.260	15.03	0.935	33
Ar	-181 to -85	-113.32	13.06	108.37	0.291	10.50	0.856	96
Kr	-225 to -111	-145.71	15.68	140.18	0.301	9.52	0.836	125
Xe	-283 to -155	-195.46	17.93	193.25	0.326	10.15	0.795	162
iNe$^{(1)}$	-65 to -36	-45.11	4.08	43.89	0.326	15.03	0.795	
dXe$^{(1)}$	-305 to -150	-207.55	29.18	193.25	0.260	10.15	0.935	
dXe$^{(2)}$	-295 to -155	-199.40	19.33	193.25	0.316	10.15	0.810	
iXe$^{(1)}$	-248 to -170	-195.31	11.21	193.25	0.396	10.15	0.720	
iXe$^{(2)}$	-230 to -180	-194.25	7.77	193.25	0.458	10.15	0.679	

the traditional combining rules [102]:

$$\sigma_{gs} \equiv x_{Al}\sigma_{g-Al} + x_{Ni}\sigma_{g-Ni} + x_{Co}\sigma_{g-Co}, \tag{3.5}$$

where x_{Al}, x_{Ni}, and x_{Co} are the concentrations of Al, Ni, and Co in the QC, respectively. D_{gs} represents the well depth of the laterally averaged potential $V(z)$:

$$D_{gs} \equiv -min\left\{V(z)\right\}\big|_{along\ z}. \tag{3.6}$$

In addition, we normalize the σ_{gs} and D_{gs} with respect to the gas-gas interactions:

$$\sigma^{\star}_{gs} \equiv \sigma_{gs}/\sigma_{gg}, \tag{3.7}$$

$$D^{\star}_{gs} \equiv D_{gs}/\epsilon_{gg}. \tag{3.8}$$

The values of the effective parameters σ_{gs}, D_{gs}, $\sigma^{\star}_{gs}$, and $D^{\star}_{gs}$ for the four gas-surface interactions are listed in the upper part of Table 3.2. We also include the well depth for Ne, Ar, Kr, and Xe on graphite, as comparison [106].

3.1.5 Test rare gases

As shown in tables 3.1 and 3.2, Ne is the *smallest* atom and has the *weakest* gas-gas and gas-surface interactions (minima of σ_{gg}, σ_{gs}, ϵ_{gg} and D_{gs}). In addition, Xe is the

largest atom and has the *strongest* gas-gas and gas-surface interactions (maxima of σ_{gg}, σ_{gs}, ϵ_{gg} and D_{gs}). Therefore, for our analysis, it is useful to consider two test gases, iNe$^{(1)}$ and dXe$^{(1)}$, which are combinations of Ne and Xe parameters.

iNe$^{(1)}$ represents an "inflated" version of Ne, having the same gas-gas and average gas-substrate interactions of Ne but the geometrical dimensions of Xe:

$$\{\epsilon_{gg}, D_{gs}, D^{\star}_{gs}\}[\mathrm{iNe}^{(1)}] \equiv \{\epsilon_{gg}, D_{gs}, D^{\star}_{gs}\}[\mathrm{Ne}], \tag{3.9}$$

$$\{\sigma_{gg}, \sigma_{gs}, \sigma^{\star}_{gs}\}[\mathrm{iNe}^{(1)}] \equiv \{\sigma_{gg}, \sigma_{gs}, \sigma^{\star}_{gs}\}[\mathrm{Xe}]. \tag{3.10}$$

dXe$^{(1)}$ represents a "deflated" version of Xe, having the same gas-gas and average gas-substrate interactions of Xe but the geometrical dimensions of Ne:

$$\{\epsilon_{gg}, D_{gs}, D^{\star}_{gs}\}[\mathrm{dXe}^{(1)}] \equiv \{\epsilon_{gg}, D_{gs}, D^{\star}_{gs}\}[\mathrm{Xe}], \tag{3.11}$$

$$\{\sigma_{gg}, \sigma_{gs}, \sigma^{\star}_{gs}\}[\mathrm{dXe}^{(1)}] \equiv \{\sigma_{gg}, \sigma_{gs}, \sigma^{\star}_{gs}\}[\mathrm{Ne}]. \tag{3.12}$$

The resulting LJ parameters for iNe$^{(1)}$ and dXe$^{(1)}$ are summarized in the central parts of Tables 3.1 and 3.2. Furthermore, we also define three other test versions of Xe: dXe$^{(2)}$, iXe$^{(1)}$, and iXe$^{(2)}$ which have the same gas-gas and average gas-substrate interactions of Xe but deflated or inflated geometrical parameters. The last three test gases will be used in Section 3.2.5. The LJ parameters for these gases are summarized in the lower parts of Tables 3.1 and 3.2. In simulating test gases, we implicitly rescale the substrate's strengths so that the resulting adsorption potentials have the same D_{gs} as the non-inflated or non-deflated ones (Equations 3.9 and 3.11).

3.1.6 Chemical potential, order parameter, and ordering transition

To conveniently characterize the evolution of the adsorption processes of the gases we define a *normalized chemical potential* $\mu^\star$, as:

$$\mu^\star \equiv \frac{\mu - \mu_1}{\mu_2 - \mu_1}, \tag{3.13}$$

where μ_1 and μ_2 are the chemical potentials at the onset of the first and second layer formation, respectively. In addition, we introduce the *order parameter* ρ_{5-6}, defined as the probability of existence of fivefold defect [70, 71]:

$$\rho_{5-6} \equiv \frac{N_5}{N_5 + N_6}, \tag{3.14}$$

where N_5 and N_6 are the numbers of atoms having 2D coordination equal to 5 and 6, respectively. The 2D coordination is the number of neighboring atoms within a cutoff radius of $a_{NN} \cdot 1.366$ where a_{NN} is the first nearest neighbor (NN) distance of the gas in the solid phase and $1.366 = \cos(\pi/6) + 1/2$ is the average factor of the first and the second NN distances in a triangular lattice. Note that a_{NN} does not change appreciably with respect to temperature difference, e.g. a_{NN} of Xe changes from 0.440 nm at 77 K to 0.443 nm at 140 K.

In a fivefold ordering, most arrangements are hollow or filled pentagons with atoms having mostly five neighbors. Hence, the particular choice of ρ_{5-6} is motivated by the fact that such pentagons can become hexagons by gaining additional atoms with five or six neighbors. **Definition:** the five to sixfold ordering transition is defined as a decrease of the order parameter to a small or negligible final value. The phenomenon can be abrupt (first-order) or continuous. Within this framework, ρ_{5-6} and $(1-\rho_{5-6})$ can be considered as the fractions of pentagonal and triangular phases in the film, respectively.

3.2 Results

3.2.1 Adsorption isotherms

Figure 3.2 shows the adsorption isotherms of Ne, Ar, Kr, and Xe on the d-AlNiCo. The plotted quantity is the thermodynamic excess coverage (densities of adsorbed atoms per unit area), ρ_N), defined as the difference between the total density of atoms in the simulation cell and the density that would be present if the cell were filled with uniform vapor at the specified values of P and T. The simulated ranges and the experimental triple point temperatures (T_t) for Ne, Ar, Kr, and Xe are listed in Table 3.3. A layer-by-layer film growth is visible at low temperatures. Detailed inspection of the isotherms reveals that there is a continuous film growth (i.e. complete wetting) at temperatures above T_t (isotherms at $T > T_t$ are shown as dotted curves). This behavior, observed despite the high corrugation, is interesting as corrugation has been shown to be capable of preventing wetting [107, 108].

Although vertical steps corresponding to layers' formation are evident in the isotherms, the slopes of the isotherms' plateaus at the same normalized temperatures ($T^\star \equiv T/\epsilon_{gg} = 0.35$) differ between systems. To characterize this, we calculate the increase of each layer density, $\Delta\rho_N$, from the formation to the onset of the subsequent layer. $\Delta\rho_N$ is defined as $\Delta\rho_N \equiv (\rho_B - \rho_A)/\rho_A$ and the values are reported in Table 3.3 (points (A) and (B) are specified in Figure 3.2). We observe that, as the size of noble gas increases $\Delta\rho_N$ become smaller, indicating that the substrate corrugation has a more pronounced effect on smaller adsorbates, as expected since they penetrate deeper into the corrugation pockets. However, Xe does not follow this trend. This arises from the complex interplay between the corrugation energy and length of the potential with respect to the parameters of the gas ($\sigma_{gg}, \epsilon_{gg}$) in determining the density of the adsorbed layers. In the case of Ne, Ar, and Kr, the densities at points (A) are approximately the same ($\rho_A = 5.4$ atoms/nm^2), whereas

that of Xe is considerably smaller ($\rho_A = 4.2$ atoms/nm^2), because Xe dimension σ_{gg} becomes comparable to the characteristic length (corrugation) of the potential. This effect is clarified by the density profile of the films, $\rho(x, y)$, shown in Figures 3.3 and 3.4. As can be seen at points (A), the density profiles of Ne, Ar, and Kr are the same, i.e. the same set of dark spots appear in their plots. For Xe, some spots are separated with distances smaller than its core radius (σ_{gg}), causing repulsive interactions. Hence these spots will not likely appear in the density profile, resulting in a lower ρ_A. More discussion on how interaction parameters affect the shape of the isotherms is presented in Section 3.2.4. Note that the second layer in each system has a smaller $\Delta\rho_N$ than the first one. The explanation will be given when we discuss the evolution of density profiles.

Table 3.3: Results for Ne, Ar, Kr, and Xe adsorbed on d-AlNiCo. T_t is taken from reference [109]. The density increase ($\Delta\rho_N$) in the first and second layers is calculated at $T^\star = 0.35$ from point (A) to (B) and (C) to (D) in Figure 3.2, respectively.

	simulated T (K)	$T^\star \equiv T/\epsilon_{gg}$	T_t (K)	$\Delta\rho_N$ at $T^\star = 0.35$ for 1st layer	for 2nd layer	θ_r
Ne	11.8 → 46	0.35 → 1.36	24.55	(12.2-5.3)/5.3=1.30	(11.1-10.2)/10.2=0.09	6°
Ar	41.7 → 155	0.35 → 1.29	83.81	(7.3-5.5)/5.5=0.33	(6.9-6.4)/6.4=0.08	30°
Kr	59.6 → 225	0.35 → 1.32	115.76	(6.9-5.5)/5.5=0.25	(6.6-6.3)/6.3=0.05	42°
Xe	77 → 280	0.35 → 1.27	161.39	(5.8-4.2)/4.2=0.38	(5.2-5.2)/5.2=0	54°

3.2.2 Density profiles

Figures 3.3 and 3.4 show the density profiles $\rho(x, y)$ at $T^\star = 0.35$ for the outer layers of Ne, Ar, Kr, and Xe adsorbed on the d-AlNiCo at the pressures corresponding to points (A) through (F) of the isotherms in Figure 3.2.

Ne/d-AlNiCo system. Figure 3.3(a) shows the evolution of adsorbed Ne. At the formation of the first layer, adatoms are arranged in a pentagonal manner following the order of the substrate, as shown by the discrete spots of the Fourier transform

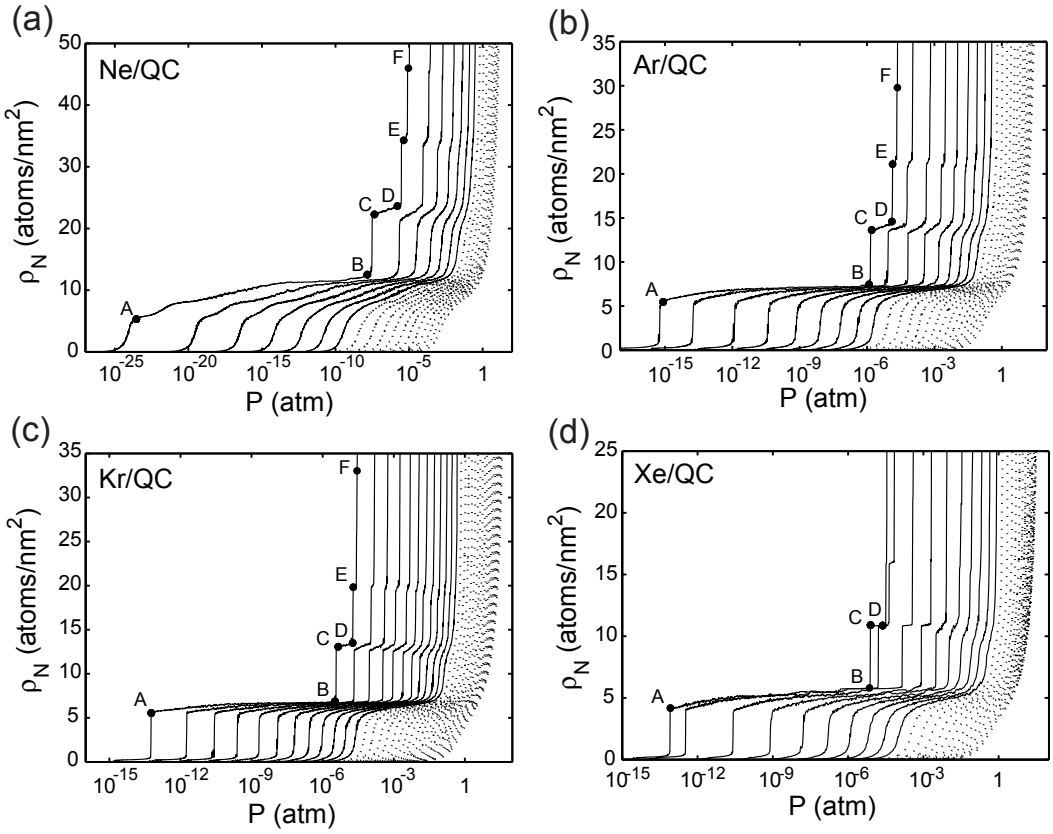

Figure 3.2: Computed adsorption isotherms for all the gas/d-AlNiCo systems. The ranges of temperatures under study are: Ne: $T = 14$ K to 46 K in 2 K steps, Ar: 45 K to 155 K in 5 K steps, Kr: 65 K to 225 K in 5 K steps, Xe: 80 K to 280 K in 10 K steps. Additional isotherms are shown with solid circles at $T^\star = 0.35$: $T = 11.8$ K (Ne), $T = 41.7$ K (Ar), $T = 59.6$ K (Kr), and $T = 77$ K (Xe). Isotherms above the triple point temperatures are shown as dotted curves.

(FT) having tenfold symmetry (point (A)). As the pressure increases, the arrangement gradually loses its pentagonal character. In fact, at point (B) the adatoms are arranged in patches of triangular lattices and the FT consists of uniformly-spaced concentric rings with hexagonal resemblance. The absence of long-range ordering in the density profile is indicated by the lack of discrete spots in the FT. This behavior persists throughout the formation of the second layer (points (C) and (D)) until the appearance of the third layer (point (E)). At this and higher pressures, the FT shows patterns oriented as hexagons rotated by $\theta_r = 6°$, indicating the presence of short-

range triangular order on the outer layer (point (F)). In summary, between points (A) and (F) the arrangement evolves from pentagonal fivefold to triangular sixfold with considerable disorder, as the upper part of the density profile at point (F) shows. The transformation of the density profile, from a lower-packing-density (pentagonal) to a higher-packing-density structure (irregular triangular), occurs mostly in the monolayer from points (A) to (B), causing the largest density increase of the first layer with respect to that of the other layers (see the end of Section 3.2.2 for more discussion). Due to the considerable amount of disorder in the final state Ne/d-AlNiCo does not satisfy the requirements for the transition as defined in Section 3.1.6.

Ar/d-AlNiCo and Kr/d-AlNiCo systems. Figures 3.3(b) and 3.4(a) show the evolutions for Ar and Kr: they are similar to the Ne case. For Ar, the pentagonal structure at the formation of the first layer is confirmed by the FT showing discrete spots having tenfold symmetry (point (A)). The quasicrystal symmetry strongly affects the overlayers' structures up to the third layer by preventing the adatoms from forming a triangular lattice (point (E)). This appears, finally, in the lower part of the density profile at the formation of the fourth layer as confirmed by the FT showing discrete spots with sixfold symmetry (point (F)). Similar to the Ne case, disorder does not disappear but remain present in the middle of the density profile corresponding to the highest coverage before saturation (point (F)). Similar situation occurs also for the evolution of Kr as shown in Figure 3.4(a).

Xe/d-AlNiCo system. Figure 3.4(b) shows the evolution of adsorbed Xe. At the formation of the first layer, adatoms are arranged in a fivefold ordering similar to that of the substrate as shown by the discrete spots of the FT having tenfold symmetry (point (A)). At point (B), the density profile shows a well-defined triangular lattice not present in the other three systems: the FT shows discrete spots arranged in regular and equally-spaced concentric hexagons with the smallest containing six

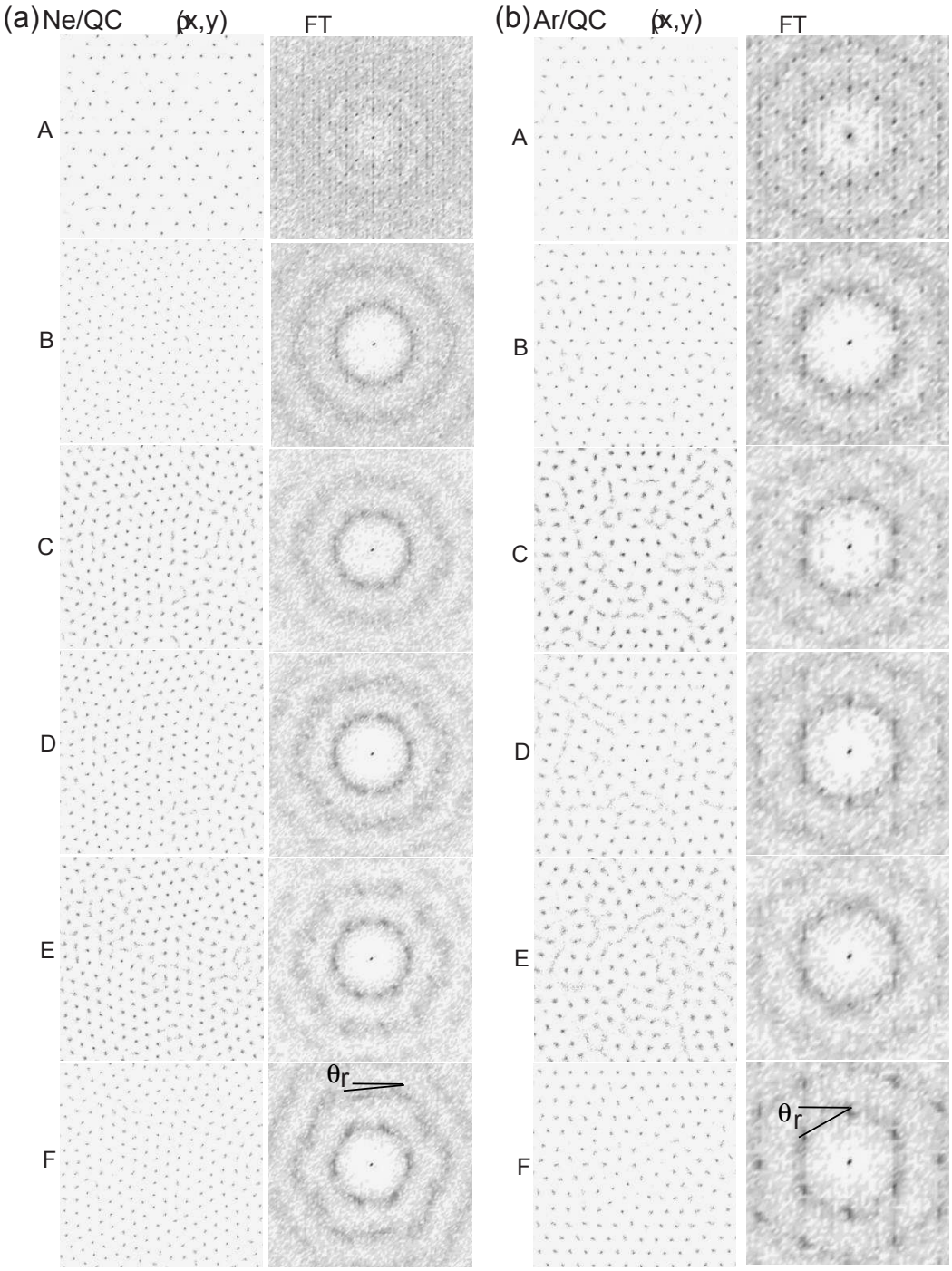

Figure 3.3: Density profiles and Fourier transforms of the outer layer at $T^\star = 0.35$ for Ne/d-AlNiCo ($T = 11.8$ K) and Ar/d-AlNiCo ($T = 41.7$ K), corresponding to points (A) through (F) of Figure 3.2.

clear spots. Thus, at point (B) and at higher pressures, the Xe overlayers can be considered to have regular closed-packed structure with negligible irregularities.

It is interesting to compare the orientation of the hexagons on FT for these four adsorbed gases at the highest available pressures before saturation (point (F) for Ne, Ar, and Kr, and point (D) for Xe). We define the orientation angles as the smallest of the possible clockwise rotations to be applied to the hexagons to obtain one side horizontal, as shown in Figures 3.3 and 3.4. Such angles are $\theta_r = 6°$, $30°$, $42°$, and $54°$, for adsorbed Ne, Ar, Kr, and Xe, respectively. These orientations, induced by the fivefold symmetry of the d-AlNiCo, can differ only by multiples of $n \cdot 12°$ [70, 71]. Since hexagons have sixfold symmetry, our systems can access only five possible orientations $(6, 18, 30, 42, 54°)$, and the final angles are determined by the interplay between the adsorbate solid phase lattice spacing, the periodic simulation cell size, and the potential corrugation. For systems without periodic boundary conditions, the ground state has been found to be fivefold degenerate, as should be the case [70, 71].

Xe adsorption on this surface was studied experimentally using LEED, in which the isobar measurements indicate that the Xe film grows layer-by-layer in the temperature range 65 K to 80 K [99], consistent with the simulations. Under similar conditions to the simulation at 77 K, at the lowest coverage, the only discernible change in the LEED pattern from that of the clean surface is an attenuation of the substrate beams. After the adsorption of one layer, there are still no resolvable features that would indicate an overlayer having order different from the substrate. At the onset of the adsorption of the second layer, however, the LEED pattern shows new diffraction spots that correspond to 5 rotational domains of a hexagonal structure. Within each of these domains, the close-packed direction of the Xe is aligned with the 5-fold directions of the substrate, as also observed in the simulation. In the experiments,

all possible alignments are observed owing to the presence of all possible rotational alignments present within the width of the electron beam (0.25 mm). When the second layer is complete, these spots are well-defined and their widths are the same as the substrate spots, indicating a coherence length of at least 15 nm. The average Xe-Xe spacing measured in the experiment is consistent with the bulk nearest-neighbor spacing of 0.44 nm. A dynamical LEED analysis of the intensities indicates that the structure of the multilayer film is consistent with face-centered cubic (FCC) Xe(111). These structure parameters for the bilayer film are essentially identical to the results obtained for Xe growth on Ag(111) [110, 111], a much weaker and less corrugated substrate. This suggests that effect of the symmetry and corrugation of the substrate potential on the Xe film structure is largely confined to the monolayer.

In every system, the increase of the density for each layer is strongly correlated to the commensurability with its support: the more similar they are, the more flat the adsorption isotherm will be (note that the support for the $(N+1)^{th}$-layer is the Nth-layer). For example, the Xe/d-AlNiCo system has an almost perfect hexagonal structure at point (B) (due to its first-order five to sixfold ordering transition as described in the next section). Hence, all the further overlayers growing on the top of the monolayer will be at least *"as regular"* as the first layer, and have the negligible density increase as listed in Table 3.3.

3.2.3 Order parameters (ρ_{5-6})

The evolution of the order parameter ρ_{5-6} is plotted in Figure 3.5 as a function of the normalized chemical potential, $\mu^{\star}$, at $T^{\star}$=0.35 for all the noble gas/d-AlNiCo systems.

Ne/d-AlNiCo, Ar/d-AlNiCo, and Kr/d-AlNiCo systems. The ρ_{5-6} plots for the first four layers observed before bulk condensation are shown in panels (a)−(c).

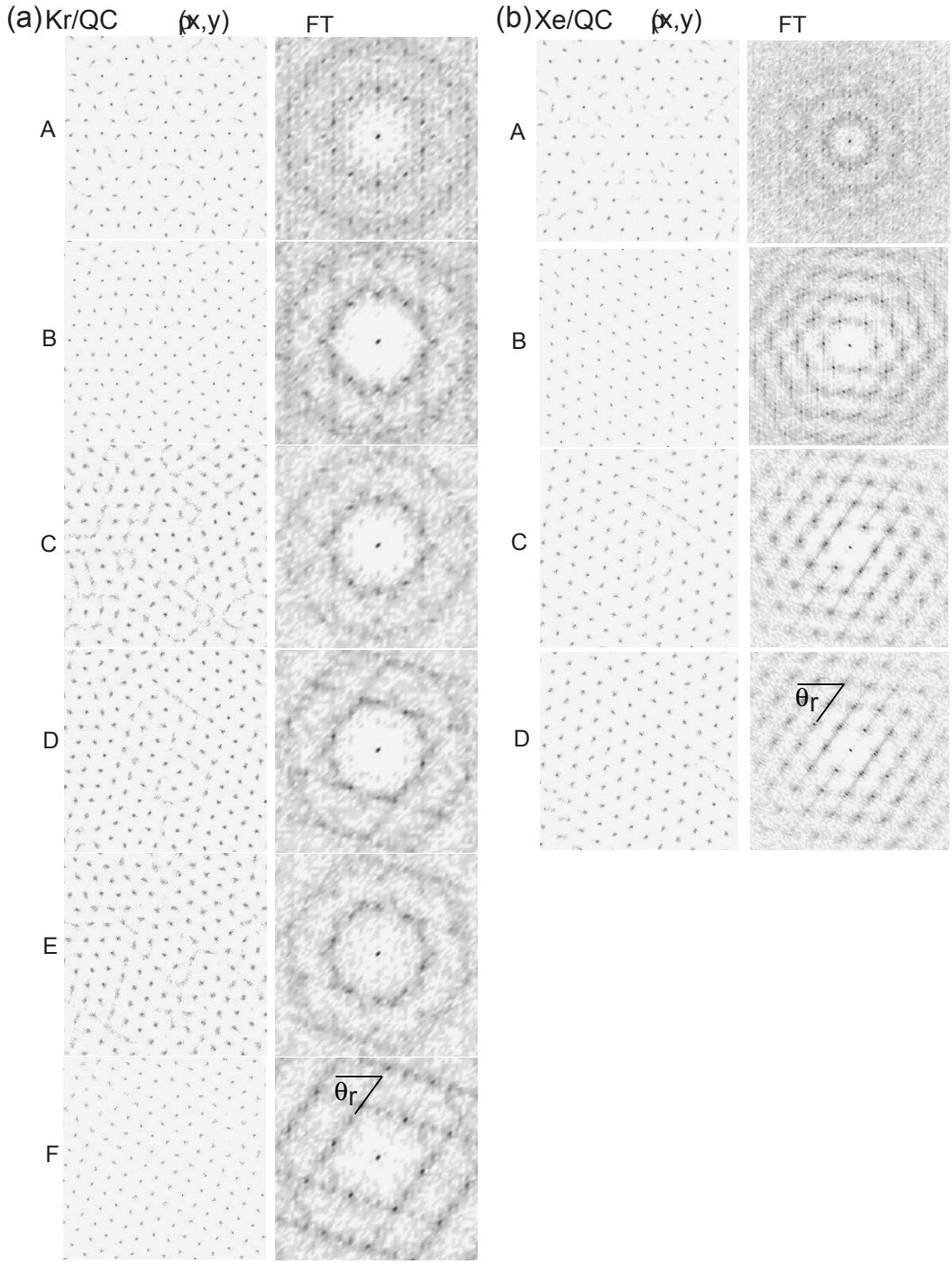

Figure 3.4: Density profiles and Fourier transforms of the outer layer at $T^\star = 0.35$ for of Kr/d-AlNiCo ($T = 59.6$ K) and Xe/d-AlNiCo ($T = 77$ K), corresponding to points (A) through (F) of Figure 3.2.

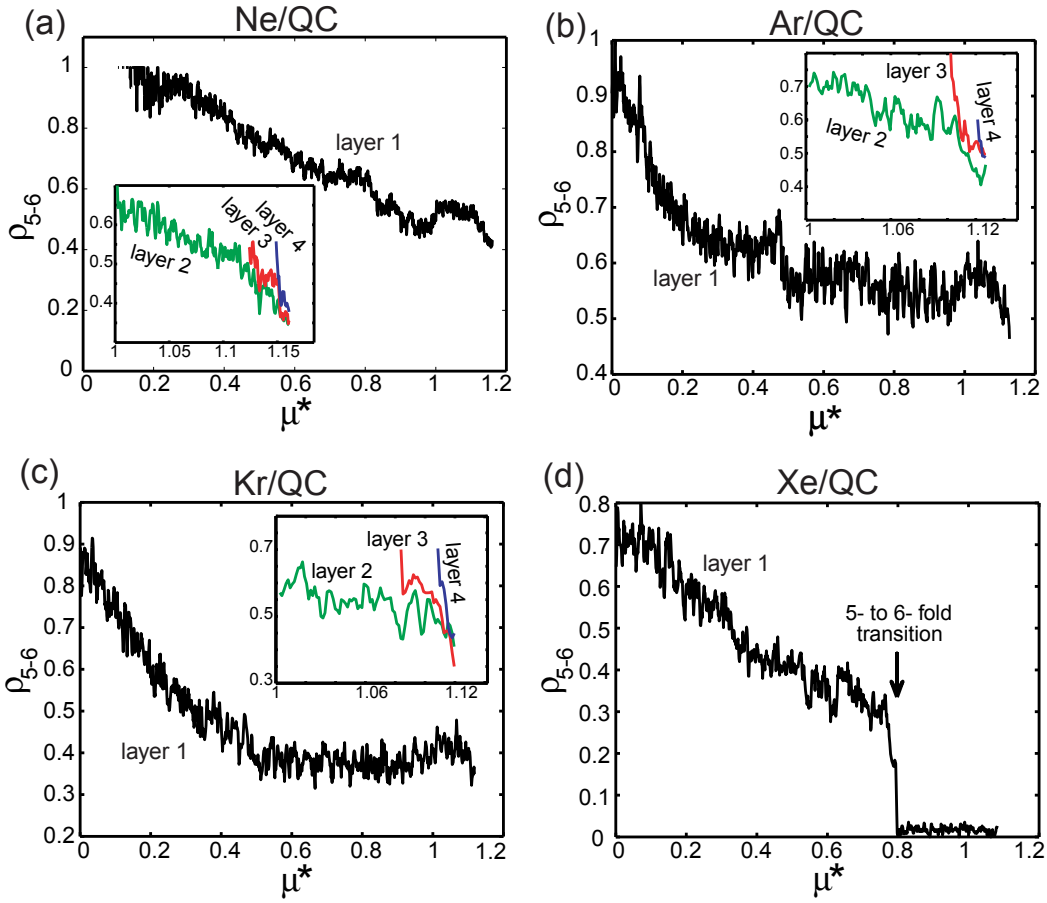

Figure 3.5: (color online). Order parameters, ρ_{5-6}, as a function of normalized chemical potential, $\mu^\star$, (as defined in the text) at $T^\star = 0.35$ for the first four layers of (a) Ne, (b) Ar, (c) Kr, and for the first layer of Xe (d) adsorbed on d-AlNiCo. A sudden drop of the order parameter in Xe/QC to a constant value of ~ 0.017 at $\mu^\star \sim 0.8$ indicates the existence of a first-order structural transition from fivefold to sixfold in the system.

As the chemical potential $\mu^\star$ increases, ρ_{5-6} decreases continuously reaching a constant value only for Kr. At bulk condensation, the values of ρ_{5-6} are still high, approximately $0.35 \sim 0.45$. Data at higher temperatures shows a similar behavior (up to T=24 K ($T^\star$=0.71) for Ne, T =70 K ($T^\star$=0.58) for Ar, and T=90 K ($T^\star$=0.53) for Kr). Thus, we conclude that these systems do not undergo the ordering transition.

Xe/d-AlNiCo system. The ρ_{5-6} plot for the first layer is shown in panel (d). In this system, as the chemical potential $\mu^\star$ increases, the order parameter gradually

decreases reaching a value of ~ 0.3 at $\mu^{\star}_{tr} \sim 0.8$. Suddenly it drops to 0.017 and remains constant until bulk condensation. Similar behavior is observed at higher temperatures up to T=140 K ($T^{\star}$=0.63). This is a clear indication of a five to sixfold ordering transition, as the first layer has undergone a transformation to an almost perfect triangular lattice. Figure 3.6(d) shows the total enthalpy in the system, H. At the transition point $\mu^{\star}_{tr}$, the enthalpy has a little step indicating a latent heat of the transition. The discontinuity of the order parameter ρ_{5-6} and the presence of latent heat indicate that the ransition is first-order. The latent heat of this transition is estimated to be $1.021/151 \approx 6.8$ meV/atom.

Despite the evidence for a first-order transition, the nearest neighbor distance, labeled r_{NN}, e.g. Xe/d-AlNiCO in Figure 3.6(b), appears to change continuously. This nearest neighbor distance is defined as the location of the first peak in the pair correlation function because the latter property is more directly comparable to diffraction measurements. We have also calculated the average spacing between neighbors, $\bar{d}_{NN}$, which is a thermodynamically meaningful quantity (related to the density). This has a small discontinuity at the transition, providing additional evidence for the first-order character of the transition. Both quantities, r_{NN} and $\bar{d}_{NN}$, are shown in Figure 3.6(b). The NN Xe-Xe distance r_{NN} decreases continuously as P increases, starting from 0.45 nm and saturating at 0.44 nm. The Xe-Xe distance reaches saturation value before the appearance of the second layer; therefore, the transition is complete within the first layer. We note that a similar decrease in NN distance was measured for Xe/Ag(111), but in that case, the NN spacing did not saturate before the onset of the second layer adsorption [112, 110].

The observed transition from fivefold to sixfold order within the first layer of Xe on d-AlNiCo can be viewed as a commensurate-incommensurate transition (CIT), since at the lower coverage, the layer is commensurate with the substrate symmetry

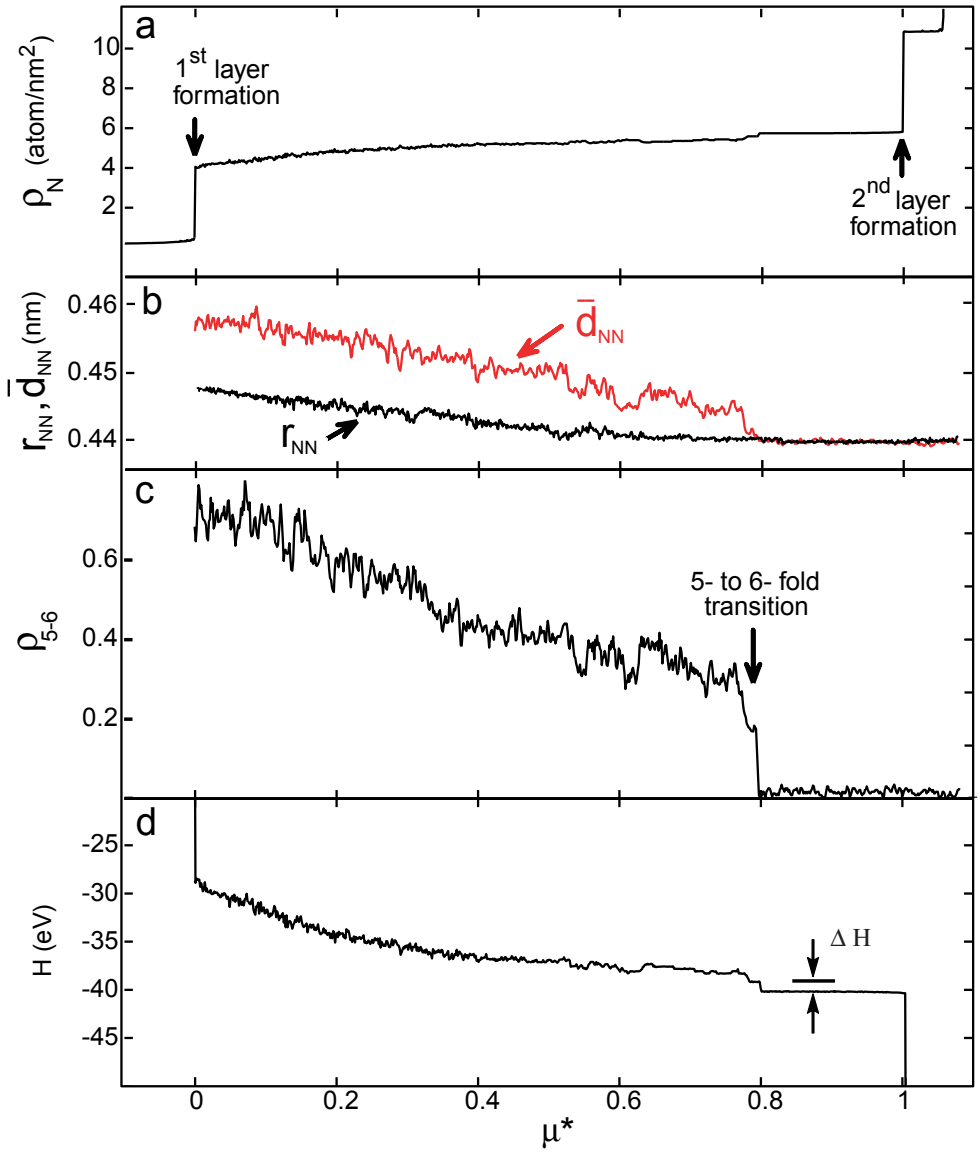

Figure 3.6: (color online). Xe on d-AlNiCo at $T = 77$ K. (a) Adsorption isotherm, ρ_N, versus the normalized chemical potential, $\mu^\star$. (b) Nearest neighbor distance derived from the first peak of pair correlation function, r_{NN}, (black line), and average spacing between neighbors at equilibrium, $\bar{d}_{NN}$, (red line). (c) Order parameter ρ_{5-6} (probability of fivefold defects, defined in Equation 3.14) versus the normalized chemical potential, $\mu^\star$. (d) Total enthalpy. The transition, which is defined as the point in $\mu^\star$ above which the order parameter remains nearly constant, occurs at $\mu^\star_{tr}$ ~0.8. The discontinuity in H around $\mu^\star_{tr} \sim 0.8$ indicates a first order transition with associated latent heat of the transition. The order parameter ρ_{5-6} after the transition is ~ 0.017. Heat of the transition is ≈ 6.8 meV/atom.

and aperiodic, while at higher coverage, it is incommensurate with the substrate. Such transitions within the first layer have been observed before for adsorbed gases, perhaps most notably for Kr on graphite [113]. There, as here for Xe, the Kr forms a commensurate structure at low coverage, which is compressed into an incommensurate structure at higher coverage. The opposite occurs for Xe on graphite, which is incommensurate at low coverage and commensurate at high coverage [114]. Such commensurate-incommensurate transitions have been studied theoretically in many ways, but perhaps most simply as a harmonic system (balls and springs) having a natural spacing that experiences a force field having a different spacing [115]. Such a transition has been found to be first-order for strongly corrugated potentials (in 1D) but continuous for more weakly corrugated potentials [116]. The transition observed in our quasicrystal surface suggests that system is within the regime of "strong" corrugation, which was not the case of Kr over graphite [113]. In fact, for the latter system, both commensurate and incommensurate structures have sixfold symmetry. A more relevant comparison may be the transition of Xe on Pt(111), from a rectangular symmetry incommensurate phase to a hexagonal symmetry commensurate one, although in that case, the low-temperature phase was incommensurate. That transition was also found to be continuous [117]. Therefore, while our simulations indicate that Xe on d-AlNiCo undergoes a CIT, as observed for other adsorbed gases, the observation of a first-order CIT is new, to our knowledge, and likely arises from the large corrugation.

3.2.4 Effects of ϵ_{gg} and σ_{gg} on adsorption isotherms

In Section 3.2.1 we have briefly discussed how the density increase of each layer ($\Delta\rho_N$) is affected by the size of the adsorbate (σ_{gg}). In addition, since the corrugation of the potential depends also on the gas-gas interaction (ϵ_{gg}), the latter quantity could *a*

priori have an effect on the density increase. To decouple the effects of σ_{gg} and ϵ_{gg} on $\Delta\rho_N$ we calculate $\Delta\rho_N$ while keeping one parameter constant, σ_{gg} or ϵ_{gg}, and varying the other. For this purpose, we introduce two test gases iNe$^{(1)}$ and dXe$^{(1)}$, which represent "inflated" or "deflated" versions of Ne and Xe, respectively (parameters are defined in Equations 3.9-3.12 and listed in Tables 3.1 and 3.2). Then we perform four tests summarized as the following:

(1) constant strength ϵ_{gg}, size σ_{gg} increases [Ne→iNe$^{(1)}$]: $\Delta\rho_N$ reduces,

(2) constant strength ϵ_{gg}, size σ_{gg} decreases [Xe→dXe$^{(1)}$]: $\Delta\rho_N$ increases,

(3) constant size σ_{gg}, strength ϵ_{gg} decreases [Xe→iNe$^{(1)}$]: $\Delta\rho_N \sim$ constant,

(4) constant size σ_{gg}, strength ϵ_{gg} increases [Ne→dXe$^{(1)}$]: enhanced agglomeration.

Figure 3.7 shows the adsorption isotherms at $T^\star = 0.35$ for Ne, iNe$^{(1)}$, Xe, and dXe$^{(1)}$ on d-AlNiCo. By keeping the strength constant and varying the size of the adsorbates, tests 1 and 2 ([Ne→iNe$^{(1)}$] and [Xe→dXe$^{(1)}$]), we find that we can reduce or increase the value of the density increase (when $\Delta\rho_N$ decreases the continuous growth tends to become stepwise and vice versa). These two tests indicate that the larger the size, the smaller the $\Delta\rho_N$. By keeping the size constant and decreasing the strength, test 3 ([Xe→iNe$^{(1)}$]), we find that $\Delta\rho_N$ does not change appreciably. An interesting phenomenon occurs in test 4 where we keep the size constant and increase the strength ([Ne→dXe$^{(1)}$]). In this test the growth of the film loses its step-like shape. We suspect that this is caused by an enhanced agglomeration effect as follows. Ne and dXe$^{(1)}$ have the same size which is the smallest of the simulated gases, allowing them to easily follow the substrate corrugation, in which case, the corrugation helps to bring adatoms closer to each other [100] (agglomeration effect). The stronger gas-gas self interaction of dXe$^{(1)}$ compared to Ne will further enhance

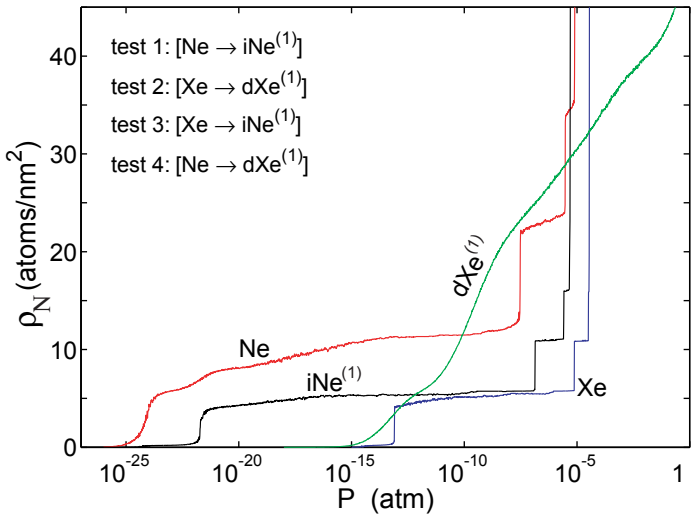

Figure 3.7: (color online). Computed adsorption isotherms for Ne, Xe, iNe$^{(1)}$, and dXe$^{(1)}$ on d-AlNiCo at $T^{\star}$=0.35. iNe$^{(1)}$ and dXe$^{(1)}$ are test noble gases having potential parameters described in the text and in Tables 3.1 and 3.2. The effect of varying the interaction strength of the adsorbates on the density increase $\Delta\rho_N$ (while keeping the size constant) is negligible on large gases but significant on small gases.

this agglomeration effect, resulting in a less stepwise film growth of dXe$^{(1)}$ than Ne. As can be seen, dXe$^{(1)}$ grows continuously, suggesting a strong enhancement of the agglomeration. In summary, the last two tests (3 and 4) indicate that the effect of varying the interaction strength of the adsorbates (while keeping the size constant) is negligible on large gases but significant on small gases.

3.2.5 Effects of ϵ_{gg} and σ_{gg} on 5- to 6-fold transition

Strength ϵ_{gg} and size σ_{gg} of the adsorbates also affect the existence of the first-order transition (present in Xe/d-AlNiCo, but absent in Ne, Ar, and Kr on d-AlNiCo). Hence we perform the same four tests described before and observe the evolution of the order parameter. The results are the following:

(1) constant strength ϵ_{gg}, size σ_{gg} increases [Ne→iNe$^{(1)}$]: transition appears

(2) constant strength ϵ_{gg}, size σ_{gg} decreases [Xe→dXe$^{(1)}$]: transition disappears

(3) constant size σ_{gg}, strength ϵ_{gg} decreases [Xe→iNe$^{(1)}$]: transition remains

(4) constant size σ_{gg}, strength ϵ_{gg} increases [Ne→dXe$^{(1)}$]: remains no transition

The strength ϵ_{gg} has no effect on the existence of the transition (tests 3 and 4), which instead is controlled by the size of the adsorbates (tests 1 and 2). To further characterize such dependence, we add three additional test gases with the same strength ϵ_{gg} of Xe but different sizes σ_{gg}. The three gases are denoted as dXe$^{(2)}$, iXe$^{(1)}$, and iXe$^{(2)}$ (the prefixes d- and i- stand for deflated and inflated, respectively). The interaction parameters, defined in the following equations, are listed in Tables 3.1 and 3.2:

$$\{\epsilon_{gg}, D_{gs}, \sigma_{gg}\}\,[\mathrm{dXe}^{(2)}] \equiv \{\epsilon_{gg}, D_{gs}, 0.95\sigma_{gg}\}[\mathrm{Xe}], \tag{3.15}$$

$$\{\epsilon_{gg}, D_{gs}, \sigma_{gg}\}[\mathrm{iXe}^{(1)}] \equiv \{\epsilon_{gg}, D_{gs}, 1.34\sigma_{gg}\}[\mathrm{Xe}], \tag{3.16}$$

$$\{\epsilon_{gg}, D_{gs}, \sigma_{gg}\}[\mathrm{iXe}^{(2)}] \equiv \{\epsilon_{gg}, D_{gs}, 1.65\sigma_{gg}\}[\mathrm{Xe}]. \tag{3.17}$$

Figure 3.8 shows the evolutions of the order parameter as a function of the normalized chemical potential for the first layer of dXe$^{(2)}$, iNe$^{(1)}$, iXe$^{(1)}$, and iXe$^{(2)}$ adsorbed on d-AlNiCo at $T^{\star}$=0.35. All these systems undergo a transition, except dXe$^{(2)}$, i.e. the transition occurs only in systems with $\sigma_{gg} \geq \sigma_{gg}[\mathrm{Xe}]$ indicating the existence of a critical value for the appearance of the phenomenon. Furthermore, as σ_{gg} increases (iNe$^{(1)}$ → iXe$^{(1)}$ → iXe$^{(2)}$), the transition shifts towards smaller critical chemical potentials.

3.2.6 Prediction of 5- to 6-fold transition

The critical value of σ_{gg} associated with the transition can be related to the characteristic length of the d-AlNiCo by introducing a *gas-substrate mismatch parameter* defined as

$$\delta_m \equiv \frac{k \cdot \sigma_{gg} - \lambda_r}{\lambda_r}. \tag{3.18}$$

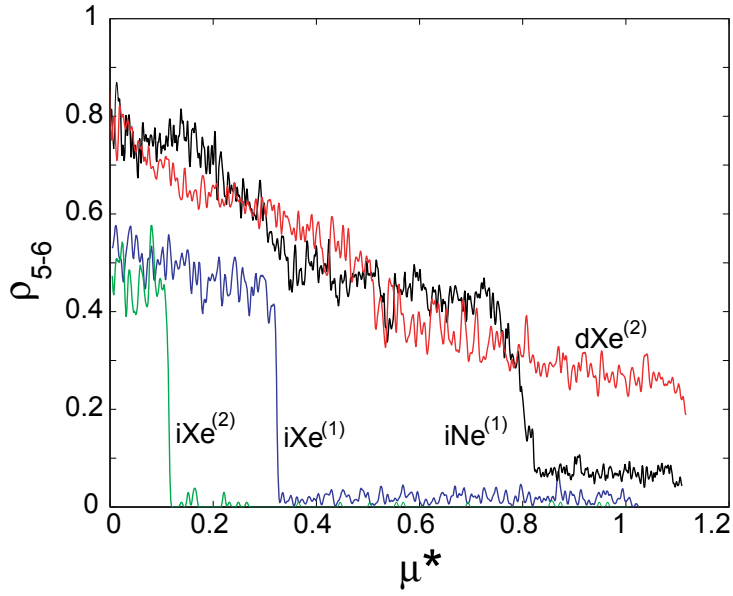

Figure 3.8: (color online). Order parameters as a function of normalized chemical potential (as defined in the text) for the first layer of dXe$^{(2)}$, iNe$^{(1)}$, iXe$^{(1)}$, and iXe$^{(2)}$ adsorbed on d-AlNiCo at $T^{\star} = 0.35$. A first-order fivefold to sixfold structural transition occurs in the last three systems, but not in dXe$^{(2)}$.

where $k = 0.944$ is the distance between rows in a close-packed plane of a bulk LJ gas (calculated at $T = 0$ K with $\sigma = 1$ [118]), and λ_r is the characteristic spacing of the d-AlNiCo, determined from the momentum transfer analysis of LEED patterns [99] (our d-AlNiCo surface has λ_r=0.381 nm [99]). With such *ad hoc* definition, δ_m measures the mismatch between an adsorbed FCC[111] plane of adatoms and the d-AlNiCo surface. In Table 3.4 we show that δ_m perfectly correlates with the presence of the transition in our test cases (transition exists $\Leftrightarrow \delta_m > 0$).

The definition of a gas-substrate mismatch parameter is not unique. For example, one can substitute $k \cdot \sigma_{gg}$ with the first NN distance of the bulk gas, and λ_r with one of the following characteristic lengths: a) side length of the central pentagon in the potential plots in Figure 3.1 ($\lambda_s = 0.45$nm), b) distance between the center of the central pentagon and one of its vertices ($\lambda_c = 0.40$nm), c) $L = \tau \cdot S = 0.45$ nm, where $\tau = 1.618$ is the golden ratio of the d-AlNiCo and $S = 0.243$ nm is the

Table 3.4: Summary of adsorbed noble gases on d-AlNiCo that undergo a first-order fivefold to sixfold structural transition and those that do not.

	δ_m	transition
Ne	-0.311	No
Ar	-0.158	No
Kr	-0.108	No
Xe	0.016	Yes
iNe$^{(1)}$	0.016	Yes
dXe$^{(1)}$	-0.311	No
dXe$^{(2)}$	-0.034	No
iXe$^{(1)}$	0.363	Yes
iXe$^{(2)}$	0.672	Yes

$k = 0.944$ [118]
$\lambda_r = 0.381$ nm [99]
$\delta_m \equiv (k \cdot \sigma_{gg} - \lambda_r)/\lambda_r$

side length of the rhombic Penrose tiles [15]. Although there is no *a priori* reason to choose one definition over the others, the one that we select (Equation 3.18) has the convenience of being perfectly correlated with the presence of the transition, and of using reference lengths commonly determined in experimental measurements (λ_r) or quantities easy to extract ($k \cdot \sigma_{gg}$).

3.2.7 Transitions on smoothed substrates

In Figure 3.1 we can observe that near the center of each potential there is a set of five points with the highest binding interaction (the dark spots constituting the central pentagons). A real QC surface contains an infinite number of these very attractive positions which are located at regular distances and with five fold symmetry. Due to the limited size and shape of the simulation cell, our surface contains only one set of these points. Therefore, it is of our concern to check if the results regarding the existence of the transition are real or artifacts of the method. We perform simulation tests by mitigating the effect of the attractive spots through a Gaussian smoothing function which reduces the corrugation of the original potential. The definitions are

the following:

$$G(x,y,z) \equiv A_G e^{-(x^2+y^2+z^2)/2\sigma_G^2}, \tag{3.19}$$

$$V(z) \equiv \langle V(x,y,z) \rangle_{(x,y)}, \tag{3.20}$$

$$V_{mod}(x,y,z) \equiv V(x,y,z) \cdot [1 - G(x,y,z)] + V(z) \cdot G(x,y,z). \tag{3.21}$$

where $G(x,y,z)$ is the Gaussian smoothing function (centered on the origin and with parameters A_G and σ_G), $V(z)$ is the average over (x,y) of the original potential $V(x,y,z)$, and $V_{mod}(x,y,z)$ is the final smoothed interaction. An example is shown in Figure 3.9(a) where we plot the minimum of the adsorption potential for a Ne/d-AlNiCo modified interaction (smoothed using $A_G = 0.5$ and $\sigma_G = 0.4$ nm). In addition, in panel (b) we show the variations of the minimum adsorption potentials along line $x = 0$ for the modified and original interactions (solid and dotted curves, respectively).

Using the modified interactions (with $A_G = 0.5$ and $\sigma_G = 0.4$ nm) we simulate all the noble gases of Table 3.4. The results regarding the phase transition on modified surfaces do not differ from those on unmodified ones, confirming that the observed transition behavior is a consequence of competing interactions between the adsorbate and the whole QC substrate rather than just depinning of the monolayer epitaxially nucleated. Therefore, the simple criterion for the existence of the transition ($\delta_m > 0$) might also be relevant for predicting such phenomena on other decagonal quasicrystal substrates.

3.2.8 Temperature vs substrate effect

Using Xe/d-AlNiCo data, we observe that defects are present at all temperatures that are simulated (20 to 286 K). The probability of defects increases with temperature, implying that their origin is entropic, as is the case for a periodic crystal. Figure

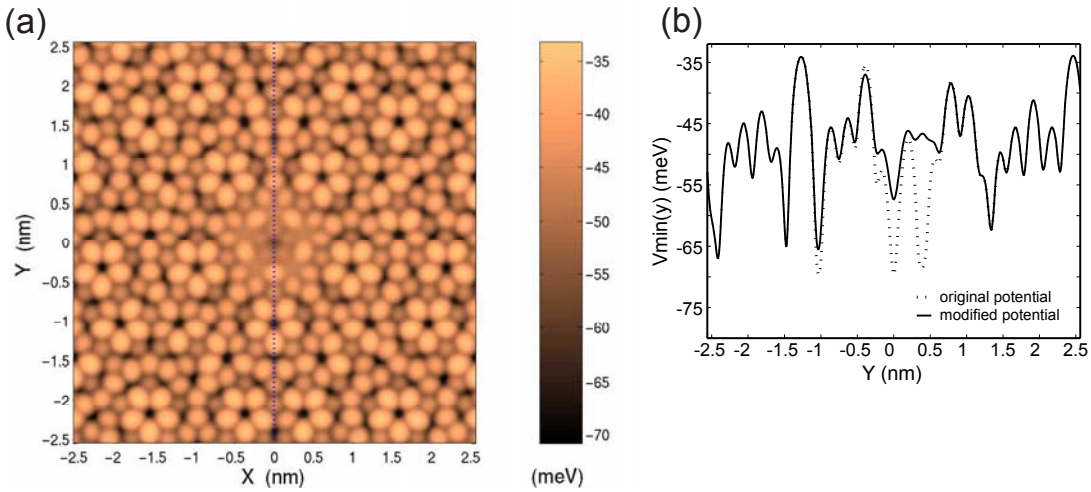

Figure 3.9: (color online). (a) The minimum of adsorption potential, $V_{min}(x, y)$, for Ne on a smoothed d-AlNiCo as described in the text. (b) The variations of the minimum adsorption potentials along the line at $x = 0$ shown in (a), for the modified and original interactions (solid and dotted curves).

3.10-(right axis) shows that the defect probability increases as T increases, while Figure 3.10-(left axis) shows the trend of the transition point in function of T. At low temperatures, the sixfold ordering occurs earlier (at lower $\mu^{\star}_{tr}$) as the temperature is increased from 40K to 70K. This trend is expected because the ordering effect imposed by the substrate corrugation becomes relatively smaller as the temperature increases. However, this trend is not observed in the higher temperature region (from 70K to 140K). In fact, at higher temperatures the transition point shifts again to higher $\mu^{\star}_{tr}$. This is most likely due to the monolayer becoming less two-dimensional, allowing more structural freedom of the Xe atoms and thus decreasing the effect of the repulsive Xe-Xe interaction that would stabilize the sixfold structure. Transitions having critical $\mu^{\star}_{tr} > 1$ indicate that the onset of second-layer adsorption occurs earlier than the transition to the sixfold structure. When the second layer adsorbs at $T >$130K, the density of the monolayer increases by a few percent, thereby increasing the effect of the repulsive interactions and driving the fivefold to sixfold transition.

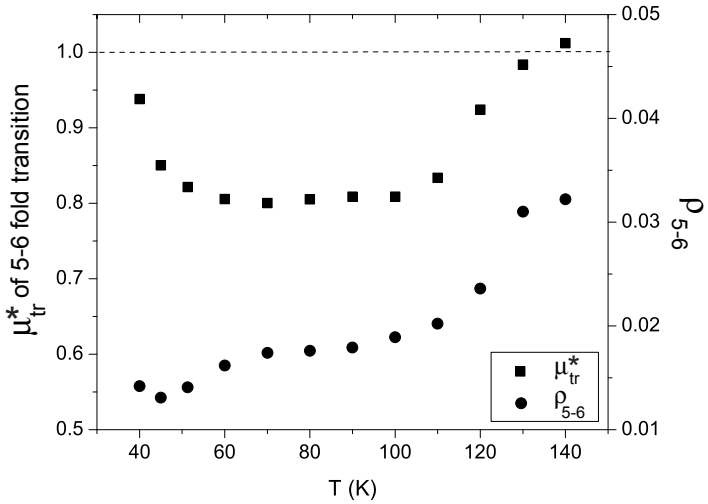

Figure 3.10: Xe on d-AlNiCo. Values of $\mu^{\star}_{tr}$ for the fivefold to sixfold transition points from 40 K to 140 K (left axis). Transition points at $\mu^{\star}_{tr} > 1$ indicate that a transfer of atoms from the second layer to the first layer is required to complete the transition. Also shown is the defect probability as a function of T after the transition occurs (right axis), indicating an increase in defect probability with T.

Interestingly, stacking faults are evident in the multilayer films. This is consistent with x-ray diffraction studies of the growth of Xe on Ag(111), where stacking faults were observed for Xe growth under various growth conditions [110, 111], although the overall structure observed was FCC(111). Such a stacking fault is evident in Figure 3.11, which shows a superposition of Xe layers 2 and 4 at 77 K. The coincidence of the atom locations in the top left part of this figure is consistent with an hexagonal close-packed structure (HEX), ABAB stacking, whereas the offsets observed in the lower part of the figure indicate the presence of stacking faults caused by dislocations in the layers. We note that while bulk Xe has an FCC structure, and indeed an FCC structure was found for the multilayer film in the LEED study, calculations of the bulk structure using LJ pair potentials such as those employed here result in a more stable HEX structure [119]. The energy difference between the two structures is very small, and apparently arises from a neglect of d-orbital overlap interactions, which

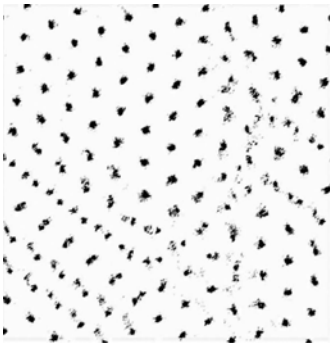

Figure 3.11: Density plot of Xe on decagonal AlNiCo at 77 K, showing a superposition of the density slices for the 2nd and 4th layers. In the top right, 4th-layer atoms are located directly above the 2nd layer atoms indicating an hexagonal close-packed ABAB stacking, whereas in other regions, such as lower left, the two layers are offset due to stacking fault.

are more effective in FCC than in HEX structures [119, 120]. Although the simulated film is HEX instead of FCC, the main conclusions concerning the growth mode of Xe on the quasicrystal are not affected [70].

3.2.9 Orientational degeneracy of the ground state

In was mentioned in the previous section that after the ordering transition is complete, the resulting sixfold structure is aligned parallel to one of the sides of the pentagons in the V_{min} map of the adsorption potential (there are five possible orientations). In the experiments, all five orientations are observed, due to the presence of all possible alignments of hexagons along five sides of a pentagon in the QC sample within the width of the electrons beam (∼0.25 mm). In an ideal infinite GCMC framework the ground state of the system would be degenerate and all five orientations would have the same energy and be equally probable. However, the square periodic boundary conditions of our GCMC break this orientational degeneracy, causing some orientations to become more likely to appear.

To find all the possible orientations, we performed simulations with a cell having free boundary conditions. The cell is a 5.12 x 5.12 nm^2 quasicrystal surface surrounded by vacuum. Figure 3.12(a) shows the V_{min} map of the adsorption potential.

Thirty simulations at 77 K are performed with this cell. The isotherms from these runs are plotted in Figure 3.12(b). Only the first layer is shown, and the finite size of the surface makes the growth of the first layer continuous. The density profiles $\rho(x, y)$ of all the simulations are analyzed at point $p^\star$ of Figure 3.12(b). In this cell, all five orientations of hexagons are observed with equal frequency indicating the orientational degeneracy of the ground state. To represent the five orientations, density profiles of five calculations (c, d, e, f, and g) are shown in Figures 3.12(c) to 3.12(g) with their FT plotted on the side. Figure 3.12(h) presents a schematic depiction of which orientations of hexagons are exemplified in each simulation.

Figures 3.13(a) and 3.13(b) illustrate the effect of pentagonal defects on the orientation of hexagons at point $p^\star$ of Figure 3.12(b). In most of the density profiles corresponding to this coverage, we find the behavior shown in Figure 3.13(a). Here, the effect of the pentagonal defect, which is the center of a dislocation in the hexagonal structure, is to rotate the orientation of the hexagons above the pentagon by $2 \cdot 60°/5 = 24°$ with respect to the hexagons below the pentagon. The possible rotations are $n \cdot 12°$, where n = 1,2,3,4, or 5. The rotation by 12° is usually mediated by more than one equivalent pentagon, as is shown in Figure 3.13(b) (note the "up" pentagon at the middle-bottom part and the "down" pentagon near the middle-top part of the figure). The "up" pentagon (with one vertex on the top) is equivalent with the "down" pentagon (with one vertex on the bottom) since they have five orientationally equivalent sides). These pentagonal defects are induced by the fivefold symmetry of the substrate, and their concentration decreases in the subsequent layers.

3.2.10 Isosteric heat of adsorption

Figure 3.14 shows a P-T diagram for three different coverages of Xe adsorbed on d-AlNiCo constructed from the isotherms in the range 40 K $< T <$ 110 K. In the

simulations, the layers grow step-wise; at 70 K the first step occurs between coverage ∼0.06 and ∼0.7, the second step occurs between coverage 1.0 and ∼1.9, and the third step occurs between coverage ∼1.9 and ∼2.8 (unit is in fractions of monolayer). Figure 3.14 shows the T, P location of these steps, denoted "cov 0.5", "cov 1.5", and "cov 2.5" for the first, second, and third steps, respectively. The isosteric heat of adsorption per atom at these steps can be calculated from the P-T diagram as follows [112]:

$$q_{st} \equiv -k_B \frac{d(lnP)}{d(1/T)_n}. \tag{3.22}$$

The inset of Figure 3.14 summarizes the values of q_{st} obtained from simulations and experiments. The agreement between experiment and the simulations for the half monolayer heat of adsorption is good. The values obtained in the simulation for the 1.5 and 2.5 layer heats are about 20% lower than the bulk value of 165 meV [99]. The lower values suggest that bulk formation should be preferred at coverages above one layer. However, layer-by-layer growth is observed at all T for at least the first few layers in these simulations. We therefore believe that the low heats of adsorption arise from slight inaccuracies in the Xe-Xe LJ parameters used in this calculation, as the heats of adsorption are very sensitive to the gas parameters.

3.2.11 Effect of vertical dimension

In a standard unit cell, only 2 steps, corresponding to the first and second layer adsorption, are apparent in the isotherms [101]. Further simulations indicate that when the cell is extended in the vertical direction, additional steps are observed. Therefore the number of observable steps is related to the size of the cell. Nevertheless, layering is clearly evident in the $\rho(z)$ profile, and the main features of the film growth are not altered. For Xe on d-AlNiCo, the average interlayer distance is calculated to be about 0.37 nm, compared to 0.358 nm for the interlayer distance in the $< 111 >$ direction

of bulk Xe [121]. Our simulations of multilayer films show variable adsorption as the simulation cell is expanded in the direction perpendicular to the surface. This is a result of sensitivity to perturbations (here, cell size) close to the bulk chemical potential, where the wetting film's compressibility diverges. This dependence has been seen previously in large scale simulations. See e.g. Figure 3 of reference [108]. The analog of this effect in real experiments is capillary condensation at pressures just below saturated vapor pressure (svp), the difference varying as the inverse pore radius.

3.3 Summary

The results of GCMC simulations of noble gas films on QC have been presented. Ne, Ar, Kr, and Xe grow layer-by-layer at low temperatures up to several layers before bulk condensation. We observe interesting phenomena that can only be attributed to the quasicrystallinity and/or corrugation of the substrate, including structural evolution of the overlayer films from commensurate pentagonal to incommensurate triangular, substrate-induced alignment of the incommensurate films, and density increase in each layer with the largest one observed in the first layer and in the smallest gas. Two-dimensional quasicrystalline epitaxial structures of the overlayer form in all the systems only in the monolayer regime and at low pressure. The final structure of the films is a triangular lattice with a considerable amount of defects except in Xe/QC. Here a first-order transition occurs in the monolayer regime resulting in an almost perfect triangular lattice. The subsequent layers of Xe/QC have hexagonal close-packed structures. By simulating test systems with various sizes and strengths, we find that the dimension of the noble gas, σ_{gg}, is the most crucial parameter in determining the existence of the phenomenon which is found only in systems with $\sigma_{gg} \geq \sigma_{gg}[\mathrm{Xe}]$.

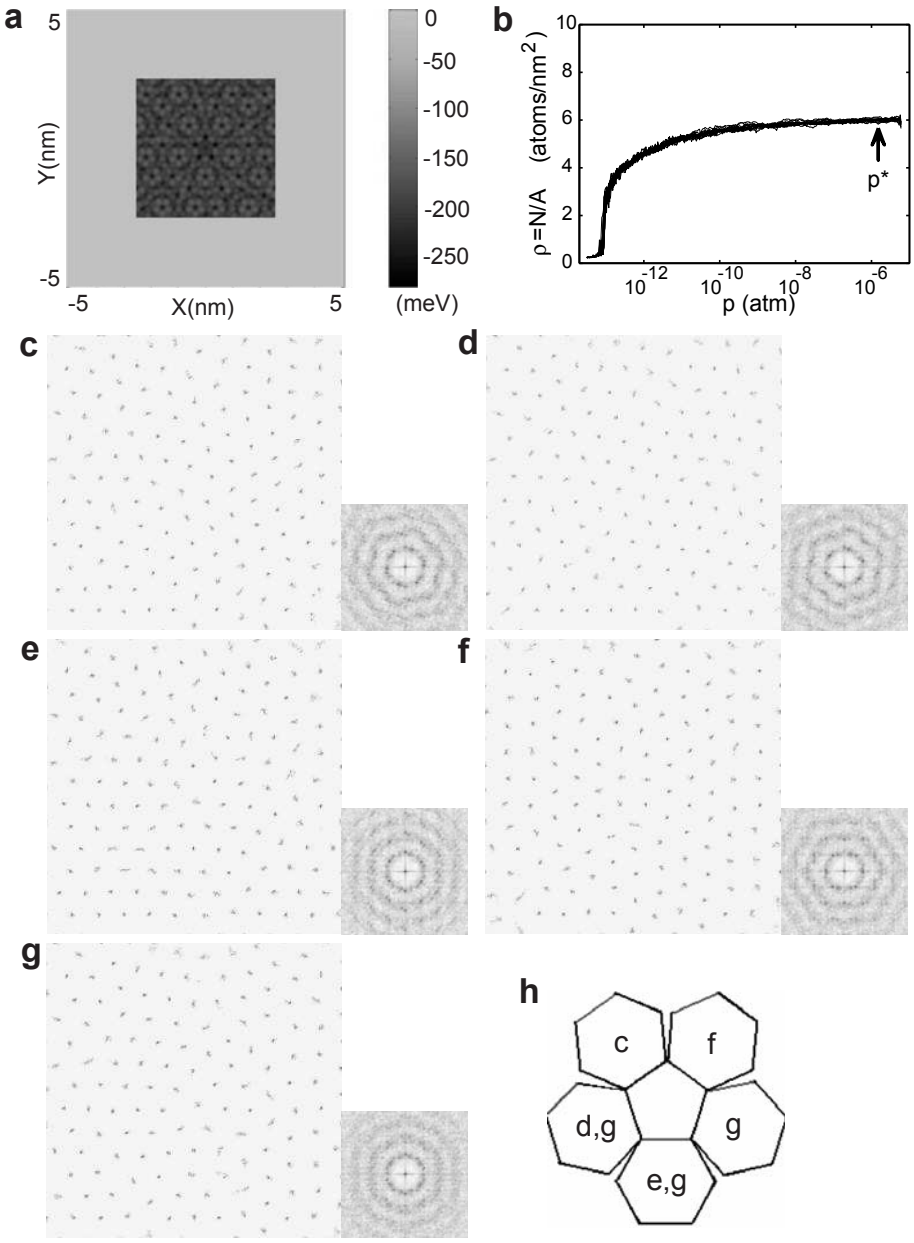

Figure 3.12: Xe adsorption on d-AlNiCo. (a) Minimum potential energy surface of the adsorption potential with free boundary conditions. (b) Adsorption isotherms of the first layer from a set of 30 simulations at 77 K using the free cell described in the paper. Five density profiles and FTs at point $p^\star$ of (b) are shown in (c) to (g), representing all possible orientations of hexagonal domains. (h) Schematic diagram illustrating the correspondence between the orientations of the hexagonal domains observed in the density profiles (c) to (g).

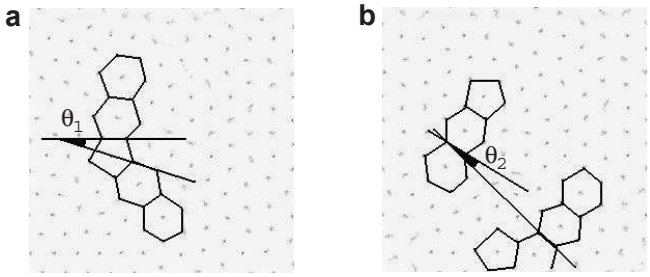

Figure 3.13: Xe adsorption on d-AlNiCo. Pentagonal defects rotate the orientation of hexagons by (a) $\theta_1 = 24°$ and (b) $\theta_2 = 12°$.

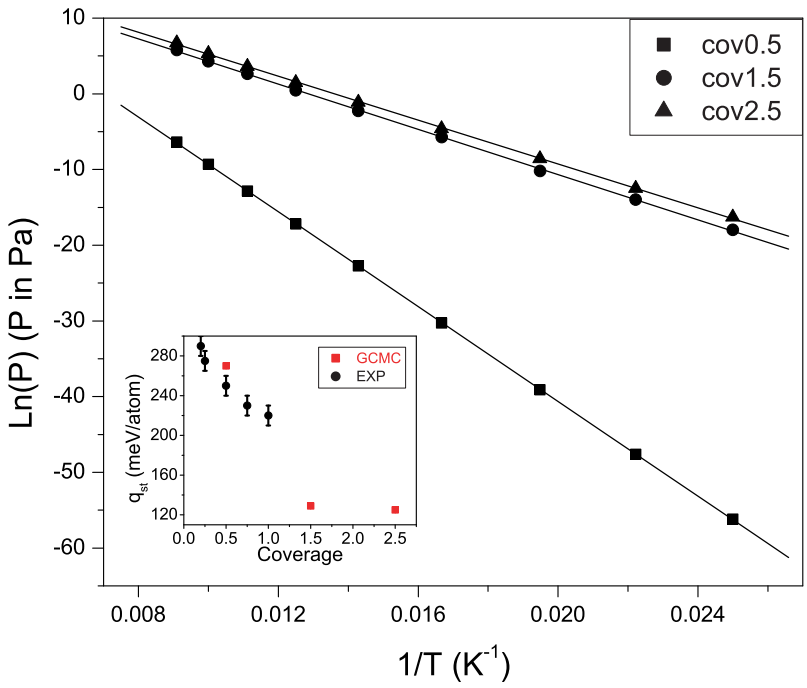

Figure 3.14: (color online). Xe adsorption on d-AlNiCo. Locations in P, T of the vertical risers in the isotherms corresponding to the first (square), second (circle), and third (triangle) layer formation. The heats of adsorptions, q_{st}, are 270, 129, and 125 meV/atom respectively, calculated as described in the text. The inset figure shows q_{st} obtained from the simulations as well as from the experiments.

Chapter 4

Embedded-atom method potentials

The interatomic potentials to simulate hydrocarbon adsorptions on d-AlNiCo are generated within the embedded-atom method (EAM) formalism. The parametrization of the potentials are given in Equations 2.30 - 2.33. These parameters are fitted to the energy of various structures computed via *ab initio* quantum calculations using VASP code. The structure prototypes are summarized in Table 4.1. For elemental Al, Co, and Ni, the prototypes are body-centered cubic (BCC), diamond structure (DIA), face-centered cubic (FCC), graphite structure (GRA), hexagonal close-packed (HEX), simple cubic (SC), and simple hexagonal (SH). The structures are first relaxed from the initial configurations to achieve the equilibrium ones. For the Al-Co-Ni ternary phases, the initial configurations are taken from the database of alloys [122]. After the structures are relaxed, the ground state electronic energies are calculated and are used as the fitting data. The technical details in relaxing the structures and evaluating the energies with VASP are given in Section 2.2.

Fitting of the parameters of the EAM potentials are performed using SIMPLEX method (Section 2.4). SIMPLEX is relatively slower than other methods such as nonlinear least square or conjugate gradient. However, since the speed of the fitting procedure is not a concern in this work (most time is spent in the *ab initio* calculations), SIMPLEX is advantageous because it does not require evaluation of function's derivatives or orthogonality. In this way, a new parametrization of EAM potentials requires changes only in the function evaluation routines. A fitting code is developed to be able to fit in a bulk or adsorption mode. In the bulk mode, the function to

Table 4.1: List of structure prototypes used to fit the EAM potentials for hydrocarbon adsorption on Al-Co-Ni. For elemental Al, Co, and Ni, the prototypes are body-centered cubic (BCC), diamond structure (DIA), face-centered cubic (FCC), graphite structure (GRA), hexagonal close-packed (HEX), simple cubic (SC), and simple hexagonal (SH). The Al–Co-Ni ternaries are taken from the database of alloys [122].

group	structure
Al	BCC, DIA, FCC, GRA, HEX, SC, SH
Co	BCC, DIA, FCC, GRA, HEX, SC, SH
Ni	BCC, DIA, FCC, GRA, HEX, SC, SH
CH_n	CH_4
C_2H_n	C_2H_2, C_2H_4, C_2H_6-isotactic, C_2H_6-syntactic
C_3H_n	propane, C_3H_4 allene, propyne, propene,
	cyclopropane, cyclopropene, cyclopropyne
C_4H_n	isobutane, 1-butene, 1-butyne, cyclobutane, methylcyclopropane
C_5H_n	pentane, cyclopentane
Other alkanes	hexane, heptane, nonane, decane, undecane, dodecane
$Al_xCo_yNi_z$	$Al_32Co12Ni_12$ (cI112)
	$Al_32Co16Ni_12$ (cI128)
	$Al_29Co4Ni_8$ (dB1)
	$Al_17Co5Ni_3$ (dH1)
	$Al_34Co4Ni_12$ (dH2)
	$Al_20Co7Ni_1$ (hP28)
	$Al_18Co4Ni_4$ (mC28)
	$Al_12Co2Ni_2$ (mC32)
	$Al_18Co2Ni_2$ (mP22)
	$Al_36Co8Ni_4$ (oI96)
	$Al_12Co1Ni_3$ (oP16)
	$Al_34Co12Ni_4$ (mC102)

minimize is the $err = \Delta E_{bulk}$ defined as:

$$\Delta E_{bulk} = \sum_i |E^{EAM}_{bulk,i} - E^{VASP}_{bulk,i}| \tag{4.1}$$

The energies are per atom and the summation is over all structures of the fit. In the adsorption mode, the error function consists of the error in the bulk energies of molecule structures ($\Delta E_{bulk,mol}$), substrate structures ($\Delta E_{bulk,sub}$), molecule-on-substrate structure ($\Delta E_{bulk,mol+sub}$), as well as in the adsorption energies (ΔE_{ads}):

$$E_{ads} = E_{bulk,mol+sub} - (E_{bulk,mol} + E_{bulk,sub}) \tag{4.2}$$

$$\Delta E_{ads} = \sum_i |E^{EAM}_{ads,i} - E^{VASP}_{ads,i}| \tag{4.3}$$

$$err = \frac{c_1 \Delta E_{bulk,mol} + c_2 \Delta E_{bulk,sub} + c_3 \Delta E_{bulk,mol+sub} + c_4 \Delta E_{ads}}{c_1 + c_2 + c_3 + c_4} \tag{4.4}$$

The coefficients c_1, c_2, c_3, and c_4 are introduced as weighing factors. To drive the parameters toward physically meaningful convergence point, the fitting is performed in multiple stages:

(1) fit potentials for elemental Al, Co, and Ni,

(2) fit potentials for Al-Co-Ni,

(3) fit potentials for hydrocarbons,

(4) fit final potentials for hydrocarbon on Al-Co-Ni.

The fitted parameters from stage (1) are used as initial conditions in stage (2). The fitted parameters from stage (2) and (3) are used as initial values in stage (4).

4.1 Stage 1: Aluminum, cobalt, and nickel

In stage (1), the elemental potentials for Al, Co, and Ni are fitted to elemental bulk energies (top part of Tables 4.2-4.4). The potentials are also trained at various

pressures to ensure stability under compression/expansion and to yield resonable lattice constants. In the calculations, different pressures are achieved by expanding or compressing the relaxed ground state structures (i.e. Al(FCC) Co(HEX) Ni(FCC)), namely at lattice constants from $a = 0.95a_0$ to $a = 1.1a_0$, where a_0 is the equilibrium lattice constant at zero pressure. Training at various pressures increases the transferability of the potentials due to a wider range of charge density covered. The fitted EAM potentials (bottom part of Tables 4.2-4.4) are able to find the ground state structure as well as the relative stability of each structure. Note that for pure elements, the bulk energy represents the cohesive energy. Going from the most stable structure to the least stable one, the EAM potentials correctly predict the following: FCC → HEX → BCC → SC → SH → GRA → DIA (for Al and Ni) and HEX → FCC → BCC → SC → SH → GRA → DIA (for Co). The potentials also give accurate equilibrium lattice constants (middle part of Tables 4.2-4.4).

4.2 Stage 2: Al-Co-Ni potentials

Results from stage (1) are used as initial conditions in stage (2). The potential for systems containing Al, Ni, and Co (AlCoNi-pot) are fitted to energies in bulk structures and in slab configurations. The latter is intended to tune the AlCoNi-pot at low charge density having different atomic environments from bulk. Slab configurations are created from dB1, dH1, and dH2. Note that dB1, dH1, and dH2 are decagonal AlNiCo quasicrystal approximants. They are crystals with a large unit cell which represent the short-ranged order of the quasicrystal. Approximants exist in the vicinity of region of chemical compositions of their quasicrystalline counterparts. The bulk unit cell of dB1, dH1, and dH2 contains 41, 25, and 50 atoms, respectively. The unit cells consist of two well-defined layers. There are two possible terminations for the bulk. The top(bottom) layer of the unit cell is labeled A(B), respectively. A

Table 4.2: (Top part) List of structures used to fit EAM potential for elemental aluminum. ρ_i is charge density at atom-i, $\Delta E = E_{EAM} - E_{VASP}$. The energies are per atom. The label "FCC at $a_0 \cdot c$" indicates that the structure is FCC with modified lattice contant by a factor of c from the equilibrium one (a_0). (Bottom part) Fitted parameters using cutoff radius $= 3 \cdot r_e$. The knots for the cubic spline of the embedding energy F are given in (ρ, F_x).

structure	ρ_i (Å^{-3})	E_{EAM} (eV/at)	E_{VASP} (eV/at)	ΔE (eV/at)
BCC	0.199	-3.375	-3.368	-0.007
DIA	0.135	-2.847	-2.722	-0.126
FCC at a_0·0.95	0.312	-3.347	-3.347	0.000
FCC at a_0·0.96	0.289	-3.396	-3.390	-0.006
FCC at a_0·0.97	0.267	-3.425	-3.422	-0.003
FCC at a_0·0.98	0.248	-3.440	-3.444	0.004
FCC at a_0·0.99	0.229	-3.443	-3.457	0.014
FCC at a_0·1.00	0.212	-3.439	-3.462	0.023
FCC at a_0·1.05	0.144	-3.356	-3.390	0.034
FCC at a_0·1.10	0.098	-3.221	-3.221	0.000
GRA	0.151	-2.882	-2.958	0.075
HEX	0.211	-3.436	-3.426	-0.009
SC	0.167	-3.108	-3.097	-0.011
SH	0.178	-3.241	-3.241	0.000

a_0(FCC) vasp = 4.04 Å
a_0(FCC) EAM = 4.00 Å

ρ_e (Å^{-3})	β	r_e (Å)	D (meV)	α (Å^{-1})	r_0 (Å)
0.026	7.182	2.700	33.64	3.038	3.012

	knot$_1$	knot$_2$	knot$_3$	knot$_4$	knot$_5$	knot$_6$	knot$_7$
ρ (Å^{-3})	0.000	0.078	0.121	0.495	0.896	1.381	2.200
F_x (eV)	0.000	-2.810	-3.106	-3.980	-3.879	-3.665	-3.074

Table 4.3: (Top part) List of structures used to fit EAM potential for elemental cobalt. ρ_i is charge density at atom-i, $\Delta E = E_{EAM} - E_{VASP}$. The energies are per atom. The label "HEX at $a_0 \cdot c$" indicates that the structure is HEX with modified lattice contant by a factor of c from the equilibrium one (a_0). (Bottom part) Fitted parameters using cutoff radius = $3 \cdot r_e$. The knots for the cubic spline of the embedding energy F are given in (ρ, F_x).

structure	ρ_i (Å^{-3})	E_{EAM} (eV/at)	E_{VASP} (eV/at)	ΔE (eV/at)
BCC	0.665	-5.380	-5.377	-0.003
DIA	0.602	-4.115	-4.141	0.027
FCC	0.693	-5.439	-5.450	0.011
GRA	0.566	-4.596	-4.567	-0.029
HEX at $a_0 \cdot 0.95$	0.973	-5.213	-5.214	0.001
HEX at $a_0 \cdot 0.96$	0.910	-5.317	-5.305	-0.012
HEX at $a_0 \cdot 0.97$	0.849	-5.386	-5.375	-0.011
HEX at $a_0 \cdot 0.98$	0.795	-5.425	-5.425	-0.000
HEX at $a_0 \cdot 0.99$	0.744	-5.442	-5.457	0.016
HEX at $a_0 \cdot 1.00$	0.697	-5.440	-5.473	0.033
HEX at $a_0 \cdot 1.05$	0.501	-5.295	-5.383	0.088
HEX at $a_0 \cdot 1.10$	0.358	-5.098	-5.098	0.000
SC	0.569	-4.984	-4.708	-0.276
SH	0.608	-5.155	-4.966	-0.189

a_0(HEX) vasp = 2.47 Å
a_0(HEX) EAM = 2.45 Å

ρ_e (Å^{-3})	β	r_e (Å)	D (meV)	α (Å^{-1})	r_0 (Å)
0.090	5.945	2.280	36.70	2.832	2.701

	knot$_1$	knot$_2$	knot$_3$	knot$_4$	knot$_5$	knot$_6$	knot$_7$
ρ (Å^{-3})	0.000	0.146	0.380	0.821	1.306	1.683	2.200
F_x (eV)	0.000	-3.374	-4.894	-5.517	-5.509	-5.008	-3.952

Table 4.4: (Top part) List of structures used to fit EAM potential for elemental nickel. ρ_i is charge density at atom-i, $\Delta E = E_{EAM} - E_{VASP}$. The energies are per atom. The label "FCC at $a_0 \cdot c$" indicates that the structure is FCC with modified lattice contant by a factor of c from the equilibrium one (a_0). (Bottom part) Fitted parameters using cutoff radius = $3 \cdot r_e$. The knots for the cubic spline of the embedding energy F are given in (ρ, F_x).

structure	ρ_i (Å^{-3})	E_{EAM} (eV/at)	E_{VASP} (eV/at)	ΔE (eV/at)
BCC	0.699	-4.928	-4.924	-0.004
DIA	0.500	-3.839	-3.839	-0.000
FCC at $a_0 \cdot 0.95$	0.980	-4.754	-4.783	0.029
FCC at $a_0 \cdot 0.96$	0.918	-4.870	-4.868	-0.002
FCC at $a_0 \cdot 0.97$	0.861	-4.941	-4.932	-0.009
FCC at $a_0 \cdot 0.98$	0.807	-4.980	-4.980	0.000
FCC at $a_0 \cdot 0.99$	0.757	-4.995	-5.010	0.015
FCC at $a_0 \cdot 1.00$	0.709	-4.993	-5.024	0.031
FCC at $a_0 \cdot 1.05$	0.507	-4.871	-4.955	0.084
FCC at $a_0 \cdot 1.10$	0.369	-4.687	-4.687	-0.000
GRA	0.543	-4.081	-4.109	0.028
HEX	0.706	-4.993	-4.998	0.005
SC	0.591	-4.464	-4.342	-0.122
SH	0.637	-4.682	-4.630	-0.052

a_0(FCC) vasp = 3.49 Å
a_0(FCC) EAM = 3.46 Å

ρ_e (Å^{-3})	β	r_e (Å)	D (meV)	α (Å^{-1})	r_0 (Å)
0.126	5.447	2.150	39.17	2.839	2.717

	knot$_1$	knot$_2$	knot$_3$	knot$_4$	knot$_5$	knot$_6$	knot$_7$
ρ (Å^{-3})	0.000	0.223	0.336	0.566	1.028	1.355	2.200
F_x (eV)	0.000	-3.899	-4.373	-4.731	-5.280	-5.028	-4.172

slab is labeled A if the top layer is layer A, and vice versa. The unit cell for slab configurations contains vacuum space of 12 Å in the vertical dimension to minimize the interaction between unit cells due to periodic boundary conditions. In relaxing the slabs, cell's size/shape and atoms are allowed to relax except the bottom atoms. In this way, the bottom atoms will be at the same coordinates as they were in the bulk which will be more appropriate (than if bottom atoms are relaxed) when the slabs are used as the substrates in the adsorption configurations (stage (4) of fitting). The bottom part of Table 4.5 shows the parameters of AlCoNi-pot fitted to structures listed in the top part of Table 4.5.

4.3 Stage 3: Hydrocarbon potentials

The EAM potentials for hydrocarbons (CH-pot) are fitted to the energies of isolated molecules. The *ab initio* calculations are performed in a fairly large cubic cell with vacuum size of larger than 10 Å to minimize the interaction between molecules due to periodic boundary conditions implemented in VASP. The structures are fully relaxed. In the beginning, all molecules listed in Table 4.1 are included in the fit. The resulting fitted parameters and the fitted energies are reported in Table 4.6. The results show that EAM is fairly accurate for hydrocarbons, especially for alkanes. This is interesting because EAM formalism was introduced for metals where bondings are due to nonlocal electrons. Nevertheless, not all hydrocarbons can be fit simultaneously, as significant errors are found in some molecules, e.g C_3H_4-allene, propylene, cyclopropane, cyclopropyne, 1-butene, and benzene. For our simulations, presented in Chapter 5, a more accurate fit for alkanes and benzene is needed. Table 4.7 shows the EAM potentials fitted to alkanes and benzene.

.

Table 4.5: (Top part) List of structures used to fit EAM potential for Al-Co-Ni systems. The energies are in eV/atom. (Bottom part) Fitted parameters using cutoff radius = 3·max[r_e]. The knots for the cubic spline of the embedding energy F are given in (ρ, F_x) with unit (Å^{-3},eV) and the first knot at (0,0) is assumed. The cross pair interaction between species A and B is defined as $\phi_{AB} \equiv (Z_B\phi_A/Z_A + Z_A\phi_B/Z_B)/2$.

structure	E_{EAM} (eV/at)	E_{VASP} (eV/at)	ΔE (eV/at)
cI112 bulk	-4.828	-4.828	-0.000
cI128 bulk	-4.916	-4.915	-0.000
dB1 bulk	-4.398	-4.395	-0.003
dH1 bulk	-4.483	-4.516	0.032
dH2 bulk	-4.441	-4.480	0.038
hP28 bulk	-4.484	-4.490	0.006
mC102 bulk	-4.520	-4.517	-0.003
mC28 bulk	-4.492	-4.509	0.017
mC32 bulk	-4.323	-4.322	-0.001
mP22 bulk	-4.121	-4.111	-0.010
oI96 bulk	-4.334	-4.350	0.016
oP16 bulk	-4.292	-4.300	0.007
dB1 slab3A	-3.816	-3.853	0.037
dB1 slab3B	-3.913	-3.921	0.008
dB1 slab4A	-4.105	-4.096	-0.009
dB1 slab4B	-4.015	-4.015	0.000
dH1 slab3A	-4.058	-4.043	-0.015
dH1 slab3B	-4.056	-4.028	-0.029
dH1 slab4A	-4.153	-4.155	0.003
dH1 slab4B	-4.158	-4.153	-0.005
dH2 slab4A	-4.144	-4.143	-0.001
dH2 slab4B	-3.980	-3.980	0.000

	Al	Co	Ni
ρ_e (Å^{-3})	0.026	0.090	0.126
β	7.182	5.945	5.447
r_e (Å)	2.70	2.28	2.15
D (eV)	0.034	0.037	0.039
α (Å^{-1})	1.833	3.350	3.258
r_0 (Å)	3.009	2.744	2.735
Z/Z_{Al}	1	0.862	0.521
Z/Z_{Co}		1	0.975
knot$_2$	0.086,-2.758	0.235,-3.249	0.285,-3.772
knot$_3$	0.120,-2.974	0.383,-4.834	0.341,-4.449
knot$_4$	0.517,-4.688	0.864,-5.579	0.604,-4.931
knot$_5$	0.868,-3.777	1.321,-5.420	1.050,-5.279
knot$_6$	1.365,-3.736	1.705,-5.061	1.355,-5.160
knot$_7$	2.200,-3.151	2.200,-4.090	2.200,-4.196

Table 4.6: (Top part) List of structures used to fit EAM potential for hydrocarbons. The energies are in eV/atom. (Bottom part) Fitted parameters using cutoff radius = 3·max[r_e]. The knots for the cubic spline of the embedding energy F are given in (ρ, F_x) with unit (Å^{-3},eV). The cross pair interaction between species A and B is defined as $\phi_{AB} \equiv (Z_B\phi_A/Z_A + Z_A\phi_B/Z_B)/2$.

structure	E_{EAM} (eV/at)	E_{VASP} (eV/at)	ΔE (eV/at)
methane	-4.807	-4.806	-0.001
ethane syntactic	-5.076	-5.061	-0.015
ethane isotactic	-5.068	-5.047	-0.021
C_2H_2	-5.735	-5.736	0.001
C_2H_4	-5.382	-5.328	-0.054
propane	-5.189	-5.183	-0.004
C_3H_4 allene	-5.751	-5.342	-0.409
propylene	-5.188	-5.002	-0.186
propyne	-5.679	-5.687	0.008
cyclopropane	-5.308	-4.850	-0.459
cyclopropene	-5.366	-5.273	-0.094
cyclopropyne	-5.340	-5.477	0.137
isobutane	-5.249	-5.253	0.004
1-butene	-5.250	-5.128	-0.122
1-butyne	-5.648	-5.630	-0.018
cyclobutane	-3.899	-3.899	0.000
methylcyclopropane	-5.404	-5.410	0.006
pentane	-5.291	-5.297	0.006
cyclopentane	-5.024	-5.047	0.022
hexane	-5.321	-5.329	0.008
benzene	-6.136	-6.334	0.198
heptane	-5.343	-5.352	0.009
octane	-5.358	-5.370	0.012
nonane	-5.368	-5.375	0.007
decane	-5.383	-5.381	-0.002
undecane	-5.392	-5.391	-0.001
dodecane	-5.400	-5.413	0.013

	ρ_e (Å^{-3})	β	r_e (Å)	D (eV)	α (Å^{-1})	r_0 (Å)
C	0.932	5.473	1.24	0.123	3.116	1.489
H	1.639	2.798	0.74	0.211	4.296	1.125

$Z_H/Z_C = 0.880$

		knot$_1$	knot$_2$	knot$_3$	knot$_4$	knot$_5$	knot$_6$	knot$_7$
C	ρ	0.000	0.334	1.103	1.357	1.635	1.870	2.200
	F_x	0.000	-3.851	-6.067	-8.011	-7.771	-8.17	-7.352
H	ρ	0.000	1.071	1.528	1.773	2.008	2.200	-
	F_x	0.000	-2.997	-3.482	-4.189	-3.764	-3.409	

Table 4.7: (Top part) List of structures used to fit EAM potential for alkanes and benzene. The energies are in eV/atom. (Bottom part) Fitted parameters using cutoff radius = 3· max[r_e]. The knots for the cubic spline of the embedding energy F are given in (ρ, F_x) with unit (Å^{-3},eV). The cross pair interaction between species A and B is defined as $\phi_{AB} \equiv (Z_B\phi_A/Z_A + Z_A\phi_B/Z_B)/2$.

structure	E_{EAM} (eV/at)	E_{VASP} (eV/at)	ΔE (eV/at)
methane	-4.806	-4.806	-0.000
ethane syntactic	-5.060	-5.061	0.001
propane	-5.182	-5.183	0.001
isobutane	-5.254	-5.253	-0.001
pentane	-5.298	-5.297	-0.001
hexane	-5.329	-5.329	0.000
heptane	-5.349	-5.352	0.003
octane	-5.367	-5.370	0.003
nonane	-5.380	-5.375	-0.005
decane	-5.393	-5.381	-0.012
undecane	-5.402	-5.391	-0.011
dodecane	-5.411	-5.413	0.002
benzene	-6.334	-6.334	0.000

	ρ_e (Å^{-3})	β	r_e (Å)	D (eV)	α (Å^{-1})	r_0 (Å)
C	0.932	5.473	1.24	0.116	2.793	1.477
H	1.639	2.798	0.74	0.225	3.154	1.077

$Z_H/Z_C = 0.533$

	C	H
$knot_1$	0,0	0,0
$knot_2$	0.366,-3.793	1.040,-3.543
$knot_3$	0.509,-5.454	1.534,-4.003
$knot_4$	0.761,-6.130	1.801,-3.656
$knot_5$	1.012,-7.611	1.911,-3.874
$knot_6$	1.834,-8.037	2.200,-3.736
$knot_7$	2.200,-7.288	-

4.4 Stage 4: Hydrocarbon on Al-Co-Ni

The final EAM potentials for hydrocarbon adsorption on Al-Co-Ni are fitted to the adsorption energies of a hydrocarbon on a substrate. As the substrates, dB1-slab4A and dH1-slab4A are used for methane, and dH2-slab4A are used for larger molecules. The initial conditions are taken from Tables 4.5 and 4.7 and the fitting is performed in the adsorption mode as explained previously. During the fitting, it is found that the adsorption energies are more difficult to fit than those of molecules, substrates, and molecule-on-substrate. This originates from the different nature of bonding. As discussed later in Chapter 5, alkanes do not make strong chemical bonds with the Al-Co-Ni. They are only physically adsorbed. Whereas the bondings within a molecule and within the substrate are strong. Weighing factors of $c_1 = c_2 = c_3 = 1$ and $c_4 > 1$ are used to prioritize adsorption energies. Typically, values of $c_4 < 4$ are used to get the final fit. Increasing c_4 beyond 4 does not considerably improve the fit, indicating the limitations inherent with EAM formalism. The fitted structures and energies are shown in Table 4.9 while the fitted parameters are tabulated in the Table 4.8.

Table 4.8: Fitted parameters using cutoff radius = 3· max[r_e]. The knots for the cubic spline of the embedding energy F are given in (ρ, F_x) with unit (Å^{-3},eV). The cross pair interaction between species A and B is defined as $\phi_{AB} \equiv (Z_B\phi_A/Z_A + Z_A\phi_B/Z_B)/2$. Fitting structures are given in Table 4.9

	C	H	Al	Co	Ni
ρ_e (Å^{-3})	0.932	1.639	0.026	0.09	0.126
β	5.473	2.798	7.182	5.945	5.447
r_e (Å)	1.24	0.74	2.7	2.28	2.15
D (eV)	0.116	0.225	0.034	0.037	0.039
α (Å^{-1})	2.786	3.156	1.740	3.636	3.198
r_0 (Å)	1.478	1.076	2.938	2.730	2.731
Z/Z_C	1	0.532	0.989	1.115	1.258
Z/Z_H		1	0.857	1.140	0.850
Z/Z_{Al}			1	0.370	0.498
Z/Z_{Co}				1	0.970
knot$_1$	0,0	0,0	0,0	0,0	0,0
knot$_2$	0.353,-3.860	1.037,-3.475	0.079,-2.816	0.217,-3.250	0.252,-3.932
knot$_3$	0.519,-5.429	1.527,-3.974	0.108,-3.056	0.358,-5.176	0.327,-4.425
knot$_4$	0.746,-6.254	1.797,-3.797	0.507,-4.214	0.774,-5.376	0.574,-4.849
knot$_5$	1.033,-7.443	1.899,-3.744	0.893,-3.618	1.439,-5.139	1.032,-5.194
knot$_6$	1.824,-7.988	2.200,-3.674	1.408,-3.681	1.635,-4.834	1.354,-5.065
knot$_7$	2.200,-7.264		2.200,-2.911	2.200,-3.577	2.200,-4.130

Table 4.9: Fitted energies calculated using EAM parameters in Table 4.8. Methane_up represents methane with one H below C and three H above C. Methane_down is inverse of methane_up. The unit for energy is eV/atom except for the adsorption energy which is in eV/molecule.

structure	E_{EAM}	E_{VASP}	ΔE
Molecule energy (eV/atom):			
methane	-4.805	-4.805	0.000
ethane syntactic	-5.078	-5.061	-0.017
propane	-5.189	-5.183	-0.006
butane	-5.252	-5.252	0.000
pentane	-5.293	-5.297	0.004
hexane	-5.322	-5.328	0.007
benzene	-6.294	-6.334	0.040
Substrate energy (eV/atom):			
dB1 slab4A	-4.132	-4.096	-0.036
dH1 slab4A	-4.141	-4.155	0.014
dH2 slab4A	-4.135	-4.143	0.008
Molecule and substrate energy (eV/atom):			
methane on dB1 slab4A	-4.173	-4.139	-0.034
methane_up on dH1 slab4A	-4.204	-4.219	0.015
methane_down on dH1 slab4A	-4.205	-4.219	0.014
ethane syntactic on dH2 slab4A	-4.207	-4.214	0.006
propane on dH2 slab4A	-4.242	-4.249	0.007
butane on dH2 slab4A	-4.276	-4.283	0.008
pentane on dH2 slab4A	-4.306	-4.315	0.009
hexane on dH2 slab4A	-4.337	-4.346	0.009
benzene on dH2 slab4A	-4.381	-4.385	0.004
Adsorption energy (eV/molecule):			
methane on dB1 slab4A	-0.225	-0.238	0.013
methane_up on dH1 slab4A	-0.238	-0.243	0.005
methane_down on dH1 slab4A	-0.304	-0.257	-0.047
ethane syntactic on dH2 slab4A	-0.348	-0.253	-0.095
propane on dH2 slab4A	-0.458	-0.328	-0.131
butane on dH2 slab4A	-0.439	-0.439	0.000
pentane on dH2 slab4A	-0.465	-0.527	0.062
hexane on dH2 slab4A	-0.520	-0.589	0.069
benzene on dH2 slab4A	-0.790	-0.791	0.001

Chapter 5

Hydrocarbon adsorptions on d-AlNiCo

The low friction properties of quasicrystals in ambient conditions coupled with their high hardness and oxidation resistance led to the development of applications of quasicrystal coatings, for instance on machine parts, cutting blades, and non-stick frying pans [5]. In machine parts, hydrocarbons are commonly used as a lubricant. Superlubricity is the name given to the phenomenon in which two parallel single crystal surfaces slide over each other with vanishingly small friction because their structures are incommensurate. This phenomenon was proposed in the early 1990's [12] and experiment evidence for this effect has been seen in studies of mica sliding on mica [123], W(110) on Si(100) [124], Ni(100) on Ni(100) [125], and tungsten on graphite [13]. This effect is also expected in quasicrystals due to their aperiodic structures at all length scales. Indeed, quasicrystal surfaces were observed to have low friction not long after they were first discovered [126], but pinning down the exact origin of the low friction has been elusive.

Recent experiments in ultra high vacuum (UHV) have demonstrated a frictional dependence on aperiodicity for decagonal Al-Ni-Co quasicrystal (d-AlNiCo) against thiol-passivated titanium-nitride tip [11]. In coating applications, it is expected that even if superlubricity exists between moving parts, some additional lubricant would still be needed to counter the macroscopic frictions due to grain boundaries, asperities, and other defects in the surfaces of the moving parts. Some of the requirements of the lubricant in such a situation are that it must wet the surface and that it must not remove or reduce the superlubricity. Therefore it is desirable to have a good understanding of how gases, hydrocarbons in particular, interact with quasicrystal

surfaces.

Very little is currently known about the interaction of hydrocarbons, their structures and growth on alloy or quasicrystalline surfaces. Some earlier experiments using Fourier transform infrared spectroscopy (FTIR) and low energy electron diffraction (LEED) suggest that on the 5-fold surface of Al-Pd-Mn, carbon monoxide (CO) does not adsorb at 100 K, benzene adsorb at 100 K with possibly commensurate or disordered structure (LEED pattern unchanged) [127]. The same experiments on the 10-fold surface of d-AlNiCo show that CO bonds to the Ni sites at > 132 K, no structure reported, while there is no experiment available for benzene on Al-Ni-Co [127]. Later, scaning tunneling microscopy (STM) experiments on benzene adsorption on Al-Pd-Mn show that the adsorbed benzene has a disordered structure [128]. In this chapter, we report the simulation results of small hydrocarbons adsorb on the 10-fold surface of decagonal $Al_{73}Ni_{10}Co_{17}$ [15, 16], namely for methane, propane, hexane, octane, and benzene.

5.1 Model

The simulations are performed within the framework of grand canonical ensemble using Monte Carlo (GCMC) method as previously described in Section 2.5. The simulation cell is tetragonal. We take a square section of the surface, A, of side 5.12 nm, to be the (x, y) part of the unit cell in the simulation, for which we assume periodic boundary conditions along the basal directions. The coordinates of substrate atoms are taken from Ref. [100]. The interaction potentials are modeled as the following. The *inter*molecular interactions (adsorbate-adsorbate) are calculated as a sum of pair interactions between atoms. For methane-methane [129, 130] Buckingham-type potentials are used:

$$V(r) = Ae^{-Br} - C/r^6 \tag{5.1}$$

Buckingham potentials also used to parametrize the benzene-benzene interactions [131, 132]. For linear alkane-alkane, Morse-type potentials are used:

$$V(r) = -A(1 - (1 - e^{-B(r-C)})^2) \tag{5.2}$$

The parameters for these potentials are summarized in Table 5.1. EAM potentials generated in Chapter 4 are used for the rest of the interactions, namely the *intra*molecular, adsorbate-substrate (C-Al, C-Co, C-Ni, H-Al, H-Co, H-Ni), and between substrate atoms (Al-Al, Al-Co, Al-Ni, Co-Ni). As previously mentioned in Section 4.4, the *ab initio* calculations show that alkanes and benzene do not dissociate on dB1, dH1, and dH2 (these are decagonal Al-Ni-Co approximants). In these systems, the surface of the substrate does not undergo any considerable relaxation upon the adsorption of the molecules. Therefore, as a first approximation, in our GCMC simulations, the substrate and the molecules are considered as rigid. However, molecules are allowed to explore all rotational degrees of freedom to achieve the equilibrium configurations.

5.2 Adsorption potentials

Figure 5.1 displays the minima of the adsorption potential for methane (**a**), propane (**b**), hexane (**c**), octane (**d**), and benzene (**e**), generated by minimizing the adsorption potential of a molecule on d-AlNiCo with respect to z (Equation 3.1) and all rotational degrees of freedom. The average adsorption energies are 221 (methane), 374 (propane), 620 (hexane), 794 (octane), and 931 (benzene), given in meV/molecule. The figure shows the distribution of binding sites (dark spots) for the molecule. Methane, propane, and benzene are small enough to follow the local atomic environments of the substrate, whereas hexane and octane show considerable smearing due to their large size. The location of dark spots in methane is similar to that

Table 5.1: Parameter values for the adsorbate-adsorbate interactions used for hydrocarbon adsorption on a decagonal Al-Ni-Co. Intermolecular energies are calculated as a sum of pair interactions. For methane-methane, the C-H is taken as the geometrical mean for parameter A and as the arithmetic mean for parameters B and C.

		A (eV)	B ($Å^{-1}$)	C ($Å^6$)	ref.
methane	C-C	82.132	2.693	449.53	[130]
$V(r) = Ae^{-Br} - C/r^6$	C-H	66.217	2.892	167.51	
	H-H	53.381	3.105	62.42	[129]
benzene	C-C	11527.700	3.909	524	[131, 132]
$V(r) = Ae^{-Br} - C/r^6$	C-H	348.518	3.703	75	[131, 132]
	H-H	127.447	3.746	39	[131, 132]
		(meV)	($Å^{-1}$)	(Å)	
alkane	C-C	6.984	1.2655	4.1844	[133]
$V(r) = -A(1-(1-x)^2)$	C-H	23.921	2.2744	2.544	[133]
$x = e^{-B(r-C)}$	H-H	0.002	1.255	6.1543	[133]

[129] Tsuzuki S, *et al* 1993 *J. Mol. Struct.* **280** 273
[130] Tsuzuki S, *et al* 1994 *J. Phys. Chem.* **98** 1830
[131] Califano S, *et al* 1979 *Chem. Phys. Lett.* **64** 491
[132] Chelli R, *et al* 2001 *Phys. Chem. Chem. Phys.* **3** 2803
[133] Jalkanen J-P, *et al* 2002 *J. Chem. Phys.* **116** 1303

of propane. However, it is interesting to see that the dark spots in methane and propane become the bright ones in benzene. To study more, the topview of the substrate atoms is depicted in panel (**f**) of Figure 5.1. The legend for the atoms is: Al-toplayer (gray), Al-otherlayers (black), Co-toplayer (yellow), Co-otherlayers (red), Ni-toplayer (green), and Ni-otherlayers (blue). In methane and propane, dark spots occur when the center of the molecule is located on top of black-Al (5 gray-Al on toplayer forming a pentagon). In benzene, this location gives a bright spot (less binding). Except the binding site at the center of the figure, strong binding sites (dark spots) in benzene occur when the center of benzene is located on top of gray-Al (on the top layer, the pentagon consists of 2 Al and 3 Ni, or 3 Al and 2 Ni).

5.3 Molecule orientations

First we study the orientations of a molecule as it is adsorbed on d-AlNiCo. During the calculation of minima of the adsorption potential (Section 5.2, the orientation of the molecule is recorded when a minimum is achieved. It is found that for methane, the rotational ground state is degenerate indicating its spherical nature. *Ab initio* calculations of methane dimers indicate that the interaction energy within the dimer depends on the relative orientations of the two [129, 130]. Therefore, the degeneracy observed is due to the limitation of the EAM model. For linear alkanes, we can define θ as the angle between the substrate's xy-plane and the main axis of the alkanes. Again, θ is recorded when an adsorption minimum is achieved. We find that θ decreases with increasing alkane chain, e.g. propane ($\theta = 10°$), hexane ($\theta = 5°$), and octane ($\theta \sim 0°$). For benzene, θ would be the angle between the molecule's plane and substrate's xy-plane, and it is $\theta \sim 0°$. Therefore, we conclude that alkanes and benzene prefer most contact with d-AlNiCo.

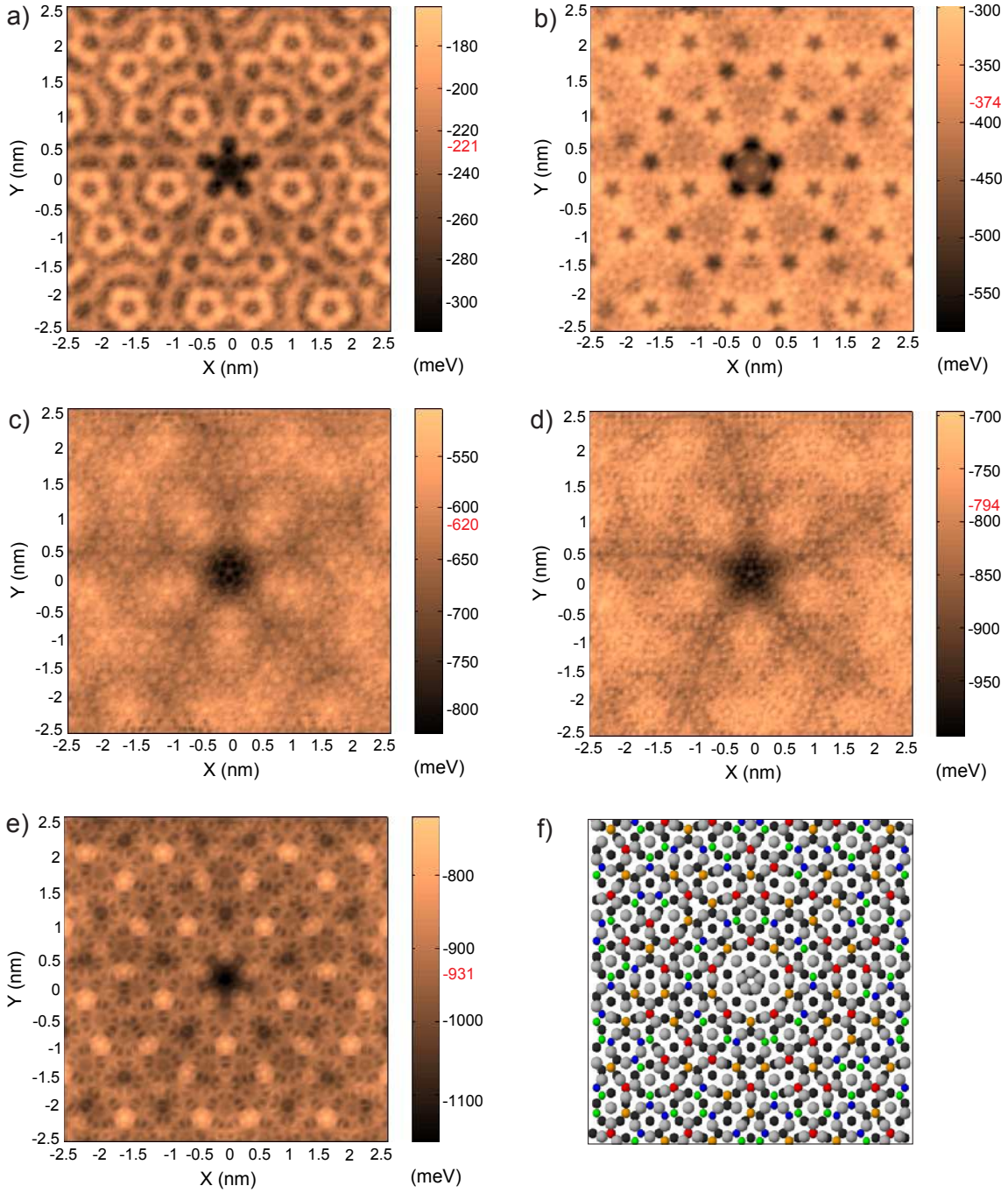

Figure 5.1: (color online). (**a-e**) Adsorption potential map, calculated by minimizing the adsorption potential of one molecule on a decagonal Al-Ni-Co along z direction and all rotational degrees of freedom at every coordinates (x, y). Red numbers represent the average value of the adsorption energies. (**f**) Top view of the decagonal Al-Ni-Co substrate 51.2x51.2 Å^2: Al-toplayer (gray), Al-otherlayers (black), Co-toplayer (yellow), Co-otherlayers (red), Ni-toplayer (green), and Ni-otherlayers (blue).

5.4 Adsorption isotherms

To use quasicrystals as low-friction coatings in conjunction with oil lubricants, the lubricants must be able to spread well on the quasicrystals. Lubricants consist mostly of alkanes. The wetting of d-AlNiCo by alkanes and benzene is demonstrated in Figure 5.2. In the figure, the number of molecules adsorbed on the substrate per area is plotted as a function of pressure at various temperatures. The results for methane, propane, hexane, octane, and benzene are shown. The simulated temperatures are: for methane $T = 68, 85, 136, 185$ K, for propane $T = 80, 127, 245, 365$ K, for hexane $T = 134, 170, 267, 450$ K, for octane $T = 162, 210, 324, 450, 565$ K, for benzene $T = 209, 270, 418, 555$ K. Note that $T = 450$ K represents a typical temperature of the inner wall of cylinder in regular car engines [134]. In the isotherms, even though the step corresponding to the adsorption of the first layer is well observed, steps corresponding to the second and further layers are not evident for methane, propane, and benzene, and barely visible for hexane and octane. The second layer condensation occurs near the bulk condensation and extends a short range of pressure, nevertheless multilayer adsorptions can be seen at higher pressures (point **d**) as shown in the inset of each panel in which the distribution of adsorbed molecules is plotted against the z direction.

5.5 Density profiles

Methane on d-AlNiCo. Figure 5.3 shows the density plots for methane at two different coverages, corresponding to points "**a**" and "**c**" on the 68 K isotherm in Figure 5.2.a. At submonolayer regime, methanes occupy the strong binding sites on the surface. At monolayer coverage, the ordering is 5-fold commensurate with the substrate, also indicated by the Fourier transform (panel **c**), and there is no transition to 6-fold. The evidence that there is no such transition is shown more

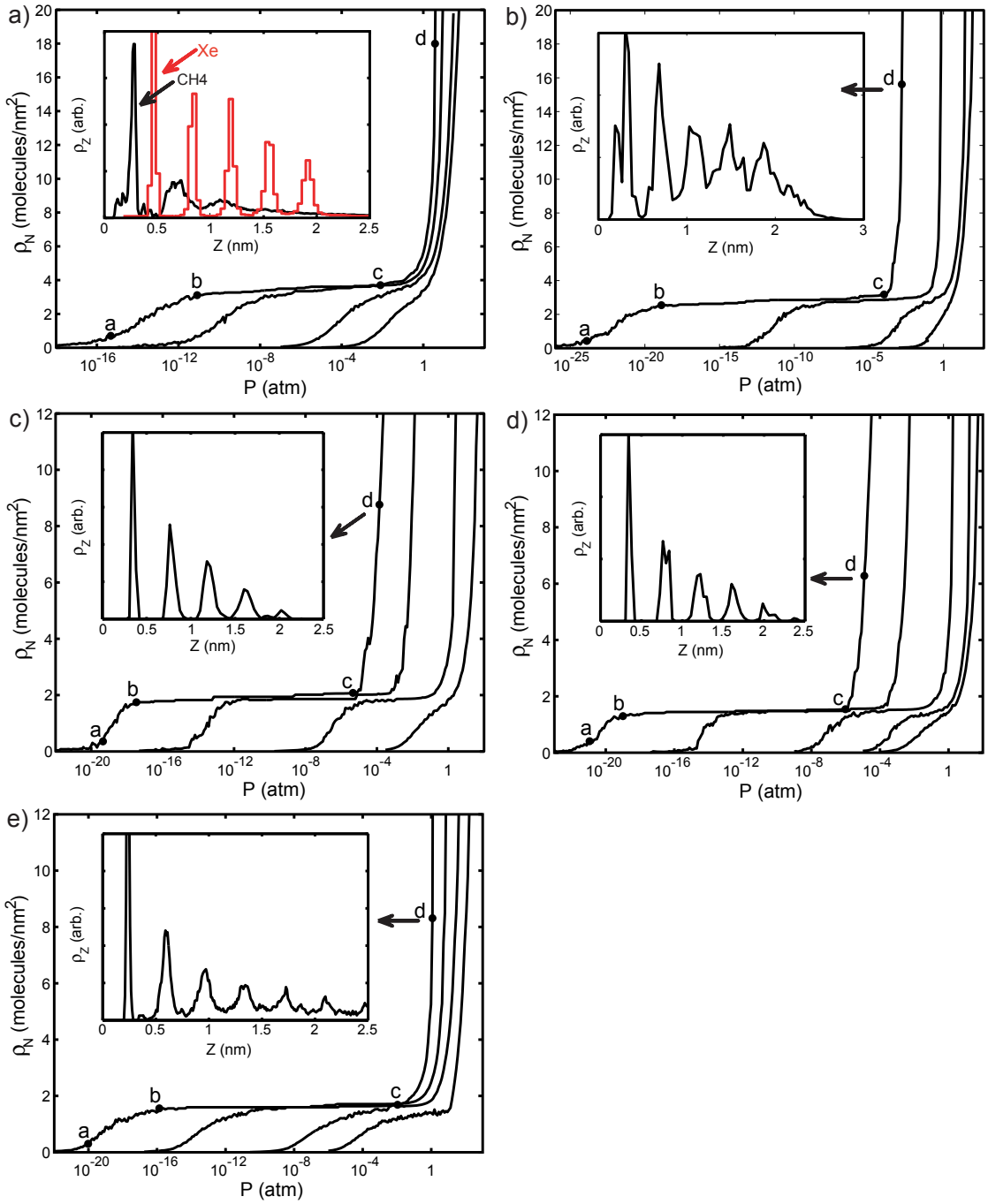

Figure 5.2: (color online). Isothermal adsorption densities of hydrocarbons on a decagonal Al-Ni-Co: (**a**) methane (from left to right T = 68, 85, 136, 185 K), (**b**) propane (T = 80, 127, 245, 365 K), (**c**) hexane (T = 134, 170, 267, 450 K), (**d**) octane (T = 162, 210, 324, 450, 565 K), and (**e**) benzene (T = 209, 270, 418, 555 K). The inset in each figure is the density along z direction at pressure corresponding to point d. Xenon (red) is plotted in panel (a) for comparison.

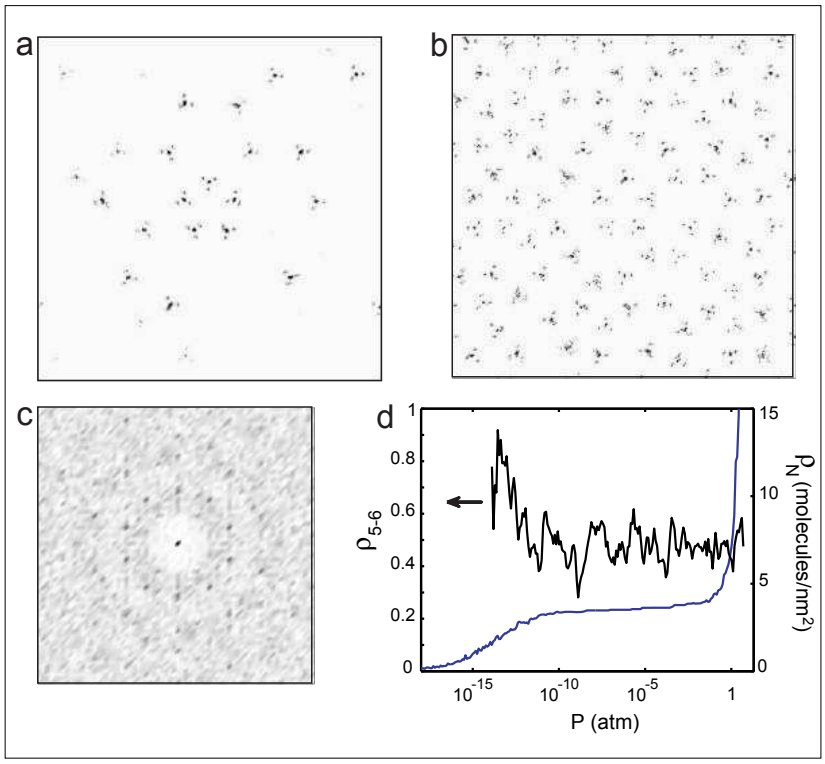

Figure 5.3: (**a**) and (**b**) Calculated density of methane adsorbed on a decagonal Al-Ni-Co at pressures corresponding to points "**a**" and "**c**" of the 68 K isotherm shown in Figure 5.2.a, respectively. (**c**) Fourier transform of the density plot shown in (**b**), consistent with 5-fold ordering of the methane near monolayer completion. (**d**) Order parameter (left axis, as calculated in Equation 3.14) as a function of pressure for the 68 K isotherm (right axis), indicating no sharp transition to 6-fold ordering.

clearly in panel **d**, where the order parameter (left axis, as calculated in Equation 3.14) does not present any sharp transition as seen in the case of xenon adsorption on the same substrate (Section 3.2.3). The lack of 5-fold to 6-fold transition is consistent with our proposed rule based on rare gases (Section 3.2.6), that the size of the rare gas must be at least as large as Xe on this quasicrystalline surface for the transition to occur [135]. Note that the size of methane relative to xenon (ratio of Lennard-Jones σ parameters) is 0.8 [69].

Propane, Hexane, and Octane on d-AlNiCo. At submonolayer coverages, propane, hexane, and octane do not show any clear evidence of binding to specific sites of the surface even though molecules tend to bind in the center of the surface with

the most attractive site. Figure 5.4 shows the density profiles for these hydrocarbons at pressure corresponding to the first layer completion at various temperatures. The simulated temperatures have been indicated in Section 5.4. At monolayer coverage, propane adsorbs in a disordered fashion at all temperatures, whereas hexane and octane tend to form close-packed structures as suggested by domains with stripe feature. As comparisons, the crystal structures of solid propane at 30 K is monoclinic (space group #11, $P2_1/m$) [136], hexane is triclinic (space group #2, $P\bar{1}$) at 90 K [136] and at 158 K [137], octane is triclinic (space group #2, $P\bar{1}$) at 90 K [136] and at 213 K [138]. The 2-dimensional structures of these hydrocarbons are close-packed structures as charactereized by stripe structures with 1 and 2 molecules per unit cell for even- and odd-alkanes, respectively [136]. In general, even-alkanes form triclinic ($6 \leq N_C \leq 26$), monoclinic ($28 \leq N_C \leq 36$), or orthorombic ($38 \leq N_C$) with decreasing packing density [136, 137, 138, 139], where N_C being the number of carbon atoms. Whereas for odd-alkanes form triclinic ($7 \leq N_C \leq 9$) or orthorombic ($11 \leq N_C$) [136, 139, 140] also with decreasing packing density for longer chain. Note that the even-alkanes have higher packing density than odd-alkanes.

Benzene on d-AlNiCo. As in the case of methane, at submonolayer coverage, benzene preferentially adsorbs at sites offering the strongest binding at all simulated temperatures. At pressure near to first layer completion, the density profiles show a temperature-dependence as plotted in Figure 5.5 for 209 K, 270 K, and 418 K. The structures are more clearly charaterized by the plotting the geometrical center of density as shown in the middle row of the figure. At $T = 209$ K, pentagonal ordering is observed. As the temperature is increased, a mixture of 5-fold and 6-fold ordering is seen, e.g. at $T = 270$ K. At higher temperature, $T = 418$ K, 6-fold structure dominates the ordering of the monolayer as confirmed by the Fourier analysis of the density showing hexagonal spots characteristic of triangular lattice (bottom row, last

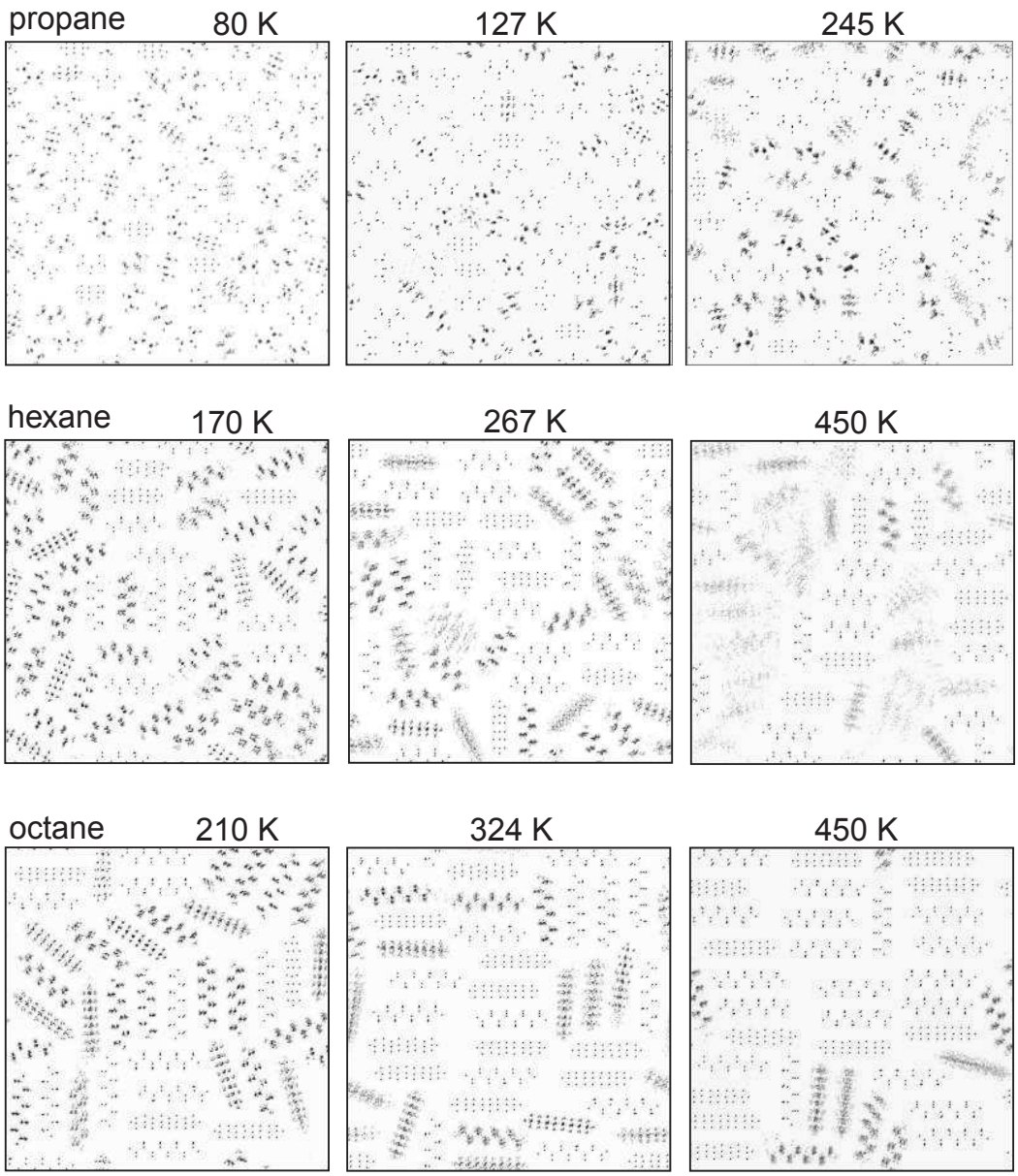

Figure 5.4: Calculated density of propane, hexane, and octane adsorbed on a decagonal Al-Ni-Co at pressure near to first layer completion. Propane forms a disordered structures, whereas hexane and octane tend to form close-packed structures indicated by stripe features with increasing order for longer chain.

column in Figure 5.5). The crystal structure of bulk benzene has been determined at 4.2 K and 270.15 K to be orthorombic (space group #61, Pbca) with 4 molecules per unit cell [141].

The evolution of the density profile over temperature from being 5-fold to 6-fold can be studied more clearly by plotting the order parameter, $\rho_{5-6} = N_5/(N_5 + N_6)$ (N_n denotes the number of molecules having n nearest neighbors as defined in Section 3.1.6) as a function of T as shown in Figure 5.6 (left axis). The plot is taken at a constant pressure of 0.01 atm corresponding to point c in Figure 5.2 panel e. The adsorption isobar representing the number of adsorbed molecules N as a function of T is plotted in right axis of Figure 5.6. Three dashed lines corresponding to T =209, 270, and 418 K, whose adsorption isotherms are plotted earlier in Figure 5.2 panel e, are added for guidance in comparing the density profile to the order parameter value at each of these temperatures. We observe the following trends:

- **(region 1)** $T < 260$ K, $0.5 < \rho_{5-6} \rightarrow$ 5-fold ordering dominates, $N = 44$.
- **(region 2)** $260 \leq T \leq 280$ K, $0.3 \leq \rho_{5-6} \leq 0.5 \rightarrow$ 5-fold becomes mostly 6-fold, $N = 44$.
- **(region 3)** $280 \leq T \leq 370$ K, $\rho_{5-6} = 0.3 \rightarrow$ 6-fold ordering dominates, $N = 44$.
- **(region 4)** $370 \leq T \leq 390$ K, $0.1 \leq \rho_{5-6} \leq 0.3 \rightarrow$ transition to 6-fold ordering, $44 \leq N \leq 46$.
- **(region 5)** $T > 390$ K, ρ_{5-6} increases from $0.1 \rightarrow$ 6-fold ordering weakens, N decreases from 46.

The highest 6-fold ordering occurs at $T = 390$ K which is mediated by a gain of 2 additional molecules adsorbed on the substrate. Beyong this temperature, thermal

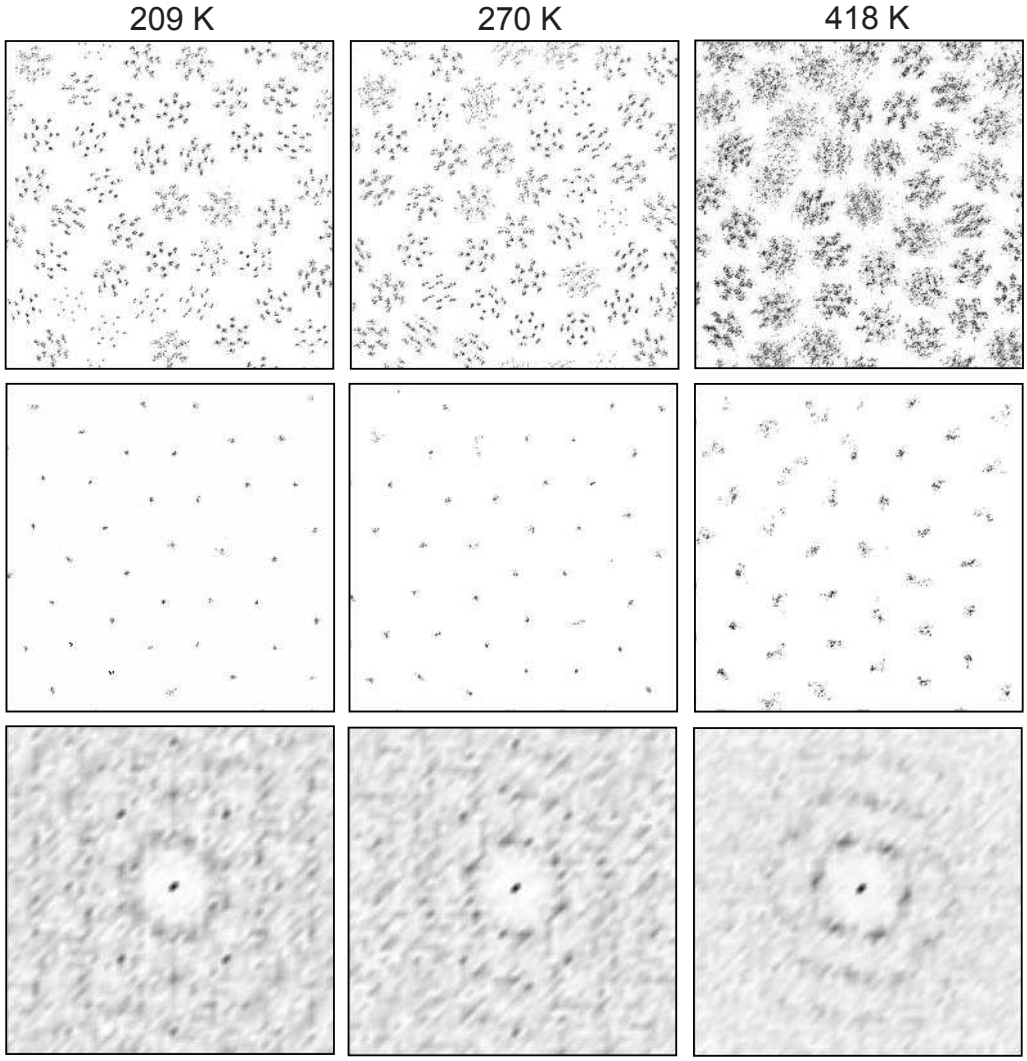

Figure 5.5: (Top row) Calculated density of benzene adsorbed on a decagonal Al-Ni-Co at pressure near to first layer completion for 209 K, 270 K, and 418 K. (middle row) Density profile of the geometrical center of density shown in the top row. (bottom row) Fourier transform of the density plot shown in the middle row, showing 5-fold ordering at 209 K, mixture of 5-fold and 6-fold structures at 270 K, and mostly 6-fold features at 418 K.

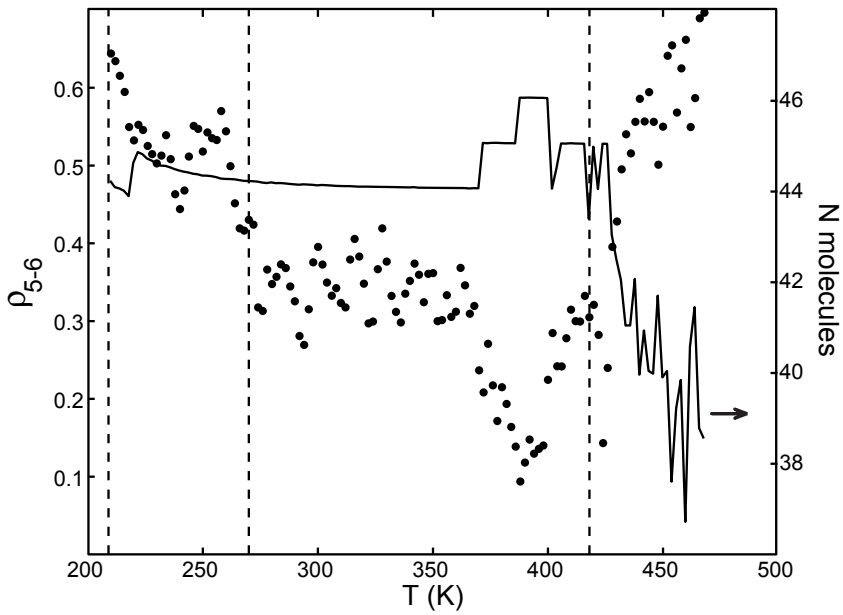

Figure 5.6: (left axis) Order parameter $\rho_{5-6} = N_5/(N_5+N_6)$ (N_n denotes the number of molecules having n nearest neighbors) as a function of temperature at 0.01 atm of pressure. (right axis) Adsorption isobar showing the number of adsorbed molecules as a function of temperature. Verticel dashed lines correspond to T = 209, 270, and 418 K whose density profiles are plotted in Figure 5.5.

energy causes reduction of N resulting in less ordered 6-fold structure as T increases. Nevertheless, the 6-fold ordering are still well resolved up to T = 418 K as shown before in Figure 5.5.

5.6 Summary

In this chapter, we have presented our studies on methane, propane, hexane, octane, and benzene adsorption on decagonal Al-Ni-Co quasicrystal. All of these hydrocarbons form very well defined step corresponding to the first layer condensation. Eventhough multilayer formation is evident from the density distribution along vertical dimension, the step corresponding to the condensation of the second and further layers can not be observed clearly in the isotherm due narrow range of pressure for these layers to form before bulk condensation occurs. Monolayer of methane has

been determined to be pentagonal commensurate with the substrate for 68 K $\leq T \leq$ 136 K. Monolayer of propane shows disordered structures for 80 K $\leq T \leq$ 245 K. Monolayers of hexane (134 K$\leq T \leq$ 450 K) and octane (162 K $\leq T \leq$ 450 K) form 2-dimensional close-packed structures characterized by stripe ordering consistent with their bulk crystal structures. Benzene monolayer is pentagonal at $T \leq$ 260 K, which transforms into 6-fold structure at $T \geq$ 280 K with the highest 6-fold ordering occurs at $T =$ 390 K. Beyong 390 K, thermal energy causes fewer adsorbed benzene and the 6-fold ordering starts to deterioates. Nevertheless, the 6-fold ordering are still well observed up to $T =$ 418 K.

Chapter 6

Embedded-atom potentials for selected pure elements in the periodic table

Embedded-atom method (EAM) formalism provides only the skeleton of calculating the total electronic energy for a given charge density. It does not specify the parametrization of the three functionals: atomic charge density, embedding energy, and pair interaction. Many different parametrizations have been introduced [54, 55, 58, 59, 59, 65, 142, 143, 144, 145]. This arises inconveniences when one needs to use different potentials for different elements. Steps toward universal EAM potentials are needed. Recently, a consistent set of atomic charge density for all elements in the periodic table suitable for EAM potentials has been developed [64]. The set is calculated by spherically averaging the atomic charge density of the solution of Hartree-Fock (HF) equations (Equation 2.19) of an isolated atom. The exchange term in the HF equation contains an atom-specific parameter which is adjusted to reproduce the experimental first ionization energy, hence are semiempirical. In this chapter we use these charge densities to generate a consistent set of EAM potentials for pure elements in the periodic table.

The parametrizations are given in Section 2.3. For each element, the potential is fitted to the *ab initio* cohesive energies in body-centered cubic (BCC), face-centered cubic (FCC), hexagonal close-packed (HEX), and diamond structure (DIA). In addition, energies in the ground state structure at different pressures are included in the fitting procedure to ensure the mechanical stability of the potentials. Energies at various pressures are achieved by expanding or compressing the equillibrium lattice

constant a by a factor from 0.90 to 1.16. Within an accuracy of 30 meV, all the EAM potentials successfully predict the correct ground state structure with respect to those that are not included in the fitting step, namely graphite (GRA), simple cubic (SC), and simple hexagonal (SH) structures. The fitted parameters are summarized in Tables 6.1-6.4. Tables 6.5 and 6.6 list the ground state structures of the elements, range of charge density covered in the fit, and the equillibrium lattice constants calculated by the *ab initio* method as well as by using the fitted EAM parameters. Literature value of the lattice constants is also included as comparisons. Overall, the EAM potentials predict the lattice constants with within 0.5 Å of the literature value except for tellurium. Indeed, elements in the V-A, VI-A, and VII-A colums of periodic table tend to form complex structures with large unit cells and more EAM parameters might be needed to fit these structures better. Manganese is excluded also because of its complex cubic structure with 58 atoms/cell. Noble gases are excluded because they are already well described by simple pair potentials. Elements in the Actinide series are excluded because they do not have a stable structure due to their radioactivity.

Table 6.1: Fitted parameters for the charge density and pair interaction functionals of the EAM potentials for pure elements, continued in Table 6.2. The fitting structures are given in Tables 6.5 and 6.6. The parameters for the embedding functionals are given in Tables 6.3 and 6.4.

Z	Struct.	ρ_e (Å^{-3})	β	r_e (Å)	D (eV)	α (Å^{-1})	r_0 (Å)
3	Li	0.038	4.813	2.670	0.010	3.015	2.422
4	Be	0.031	7.174	2.450	0.016	3.317	2.216
6	C	0.932	5.473	1.240	0.115	3.152	1.441
11	Na	0.021	5.552	3.080	0.011	5.800	3.500
12	Mg	0.001	10.030	3.890	0.012	2.807	3.110
13	Al	0.026	7.182	2.700	0.034	3.038	3.012
14	Si	0.072	7.171	2.250	0.043	4.115	1.601
19	K	0.008	6.412	3.920	0.015	2.926	4.088
20	Ca	0.002	9.719	4.280	0.020	2.940	3.646
21	Sc	0.058	6.053	2.700	0.021	2.264	3.210
22	Ti	0.287	4.333	1.940	0.022	2.282	2.850
23	V	0.394	4.025	1.780	0.023	2.501	2.615
24	Cr	0.297	4.538	1.680	0.024	2.519	2.494
26	Fe	0.192	5.214	2.000	0.026	5.747	2.412
27	Co	0.090	5.945	2.280	0.037	2.832	2.701
28	Ni	0.126	5.447	2.150	0.039	2.839	2.717
29	Cu	0.052	5.864	2.220	0.029	2.589	2.553
30	Zn	0.0005	14.630	4.800	0.030	2.655	2.560
32	Ge	0.042	7.419	2.440	0.045	2.659	2.001
37	Rb	0.006	6.788	4.210	0.037	3.599	4.694
38	Sr	0.002	9.614	4.450	0.038	2.926	3.299
39	Y	0.037	6.593	3.000	0.039	2.123	3.300
40	Zr	0.158	5.287	2.300	0.040	2.132	3.230
41	Nb	0.145	5.556	2.080	0.041	2.347	2.858
42	Mo	0.201	5.621	1.940	0.042	2.153	2.728
43	Tc	0.365	4.968	1.880	0.043	2.559	2.640
44	Ru	0.047	6.360	2.400	0.044	2.702	2.700
45	Rh	0.020	6.981	2.680	0.045	2.609	2.687
46	Pd	0.017	8.389	2.500	0.036	2.719	2.791
47	Ag	0.028	6.619	2.530	0.027	2.982	3.055
48	Cd	0.0005	13.340	4.500	0.048	2.284	3.170
52	Te	0.047	8.157	2.560	0.052	2.477	2.245
56	Ba	0.001	10.020	4.900	0.056	2.815	3.847
57	La	0.009	8.106	3.890	0.057	2.518	3.350

Table 6.2: continuation of Table 6.1.

58	Ce	0.013	7.575	3.682	0.058	2.488	2.949
59	Pr	0.016	7.342	3.646	0.059	2.502	2.970
60	Nd	0.015	7.361	3.632	0.060	2.543	3.548
63	Eu	0.016	7.306	3.542	0.033	2.596	3.300
64	Gd	0.015	7.724	3.470	0.064	2.549	3.240
65	Tb	0.017	7.323	3.464	0.065	2.527	3.300
66	Dy	0.017	7.303	3.420	0.066	2.512	3.240
67	Ho	0.018	7.323	3.392	0.067	2.532	3.180
68	Er	0.019	7.271	3.346	0.068	2.560	3.260
69	Tm	0.020	7.284	3.320	0.069	2.597	3.140
70	Yb	0.020	7.250	3.274	0.070	2.542	3.522
71	Lu	0.023	6.972	3.342	0.071	2.596	3.210
72	Hf	0.138	5.581	2.350	0.072	2.454	2.900
73	Ta	0.142	6.016	2.300	0.073	2.026	2.766
74	W	0.137	6.176	2.270	0.074	2.350	2.630
75	Re	0.242	3.686	2.040	0.075	3.055	2.760
76	Os	0.029	7.771	2.760	0.076	2.696	2.540
77	Ir	0.244	6.055	1.960	0.077	3.142	2.715
78	Pt	0.021	7.539	2.500	0.078	2.919	2.772
79	Au	0.024	7.553	2.470	0.079	2.917	2.885
81	Tl	0.004	8.850	3.500	0.081	2.576	3.300
82	Pb	0.002	8.368	2.930	0.082	2.935	3.242

Table 6.3: Fitted knots of cubic spline of the embedding functionals for the EAM potentials of pure elements, continued in Table 6.4. The first knot at (0,0) is assumed. The fitting structures are given in Tables 6.5 and 6.6.

	$knot_2$ (Å^{-3},eV)	$knot_3$ (Å^{-3},eV)	$knot_4$ (Å^{-3},eV)	$knot_5$ (Å^{-3},eV)	$knot_6$ (Å^{-3},eV)	$knot_7$ (Å^{-3},eV)
Li	0.048,-1.058	0.119,-1.52850	0.190,-1.54750	0.246,-1.607	0.291,-1.554	0.469,-1.469
Be	0.178,-3.079	0.228,-3.241	0.423,-3.509	0.731,-3.647	1.057,-3.588	1.670,-3.324
C	0.301,-4.967	0.344,-5.905	0.476,-6.986	0.861,-7.490	1.419,-7.264	2.389,-5.970
Na	0.014,-0.725	0.029,-0.9756	0.062,-1.059	0.082,-1.057	0.135,-1.059	0.181,-1.424
Mg	0.015,-0.939	0.033,-1.292	0.062,-1.414	0.096,-1.413	0.133,-1.356	0.242,-1.175
Al	0.078,-2.811	0.121,-3.106	0.495,-3.980	0.897,-3.879	1.381,-3.665	2.200,-3.074
Si	0.057,-3.662	0.087,-4.153	0.157,-4.476	0.286,-4.409	0.349,-4.204	0.561,-3.168
K	0.005,-0.613	0.009,-0.757	0.025,-0.844	0.057,-0.710	0.089,-0.551	0.149,-0.415
Ca	0.009,-1.202	0.021,-1.692	0.062,-1.814	0.094,-1.719	0.135,-1.578	0.201,-1.434
Sc	0.055,-3.363	0.080,-3.787	0.140,-4.092	0.226,-4.140	0.315,-4.009	0.481,-3.612
Ti	0.133,-4.307	0.188,-4.850	0.314,-5.315	0.444,-5.410	0.712,-5.033	1.075,-4.406
V	0.245,-4.014	0.333,-4.545	0.606,-5.153	0.858,-5.111	1.058,-4.850	1.520,-4.005
Cr	0.168,-3.162	0.182,-3.277	0.300,-3.808	0.487,-3.758	0.634,-3.324	0.935,-1.915
Fe	0.171,-4.007	0.247,-4.554	0.505,-5.071	0.834,-4.962	1.072,-4.734	1.445,-4.613
Co	0.146,-3.374	0.380,-4.894	0.821,-5.517	1.306,-5.509	1.683,-5.008	2.200,-3.952
Ni	0.223,-3.899	0.336,-4.373	0.566,-4.731	1.028,-5.280	1.355,-5.028	2.200,-4.172
Cu	0.091,-2.811	0.127,-3.100	0.238,-3.280	0.334,-3.215	0.455,-2.935	0.604,-2.374
Zn	1.012,-0.752	1.604,-0.880	2.794,-0.940	3.544,-0.919	4.805,-0.822	8.006,-0.406
Ge	0.056,-3.285	0.072,-3.429	0.115,-3.592	0.188,-3.553	0.241,-3.359	0.364,-2.645
Rb	0.004,-0.552	0.009,-0.707	0.020,-0.663	0.029,-0.594	0.036,-0.633	0.047,-0.977
Sr	0.005,-1.128	0.008,-1.304	0.046,-1.558	0.063,-1.490	0.088,-1.331	0.108,-1.205
Y	0.012,-3.002	0.021,-3.548	0.098,-4.152	0.167,-4.060	0.260,-3.712	0.338,-3.459
Zr	0.052,-4.542	0.082,-5.367	0.186,-6.136	0.299,-6.147	0.489,-5.725	0.685,-5.428
Nb	0.034,-6.744	0.054,-7.933	0.139,-9.012	0.240,-8.889	0.347,-8.192	0.468,-7.278
Mo	0.059,-4.588	0.088,-5.395	0.192,-6.024	0.271,-5.941	0.363,-5.304	0.542,-4.467
Tc	0.164,-5.372	0.217,-5.913	0.317,-6.476	0.482,-6.730	0.720,-6.230	1.108,-4.437
Ru	0.088,-6.348	0.130,-7.166	0.241,-7.687	0.311,-7.756	0.457,-7.052	0.638,-6.282
Rh	0.074,-4.522	0.095,-4.900	0.176,-5.540	0.279,-5.529	0.381,-4.971	0.495,-3.965
Pd	0.017,-2.667	0.025,-3.029	0.078,-3.490	0.128,-3.256	0.166,-2.905	0.232,-2.126
Ag	0.027,-1.749	0.035,-1.894	0.117,-2.349	0.178,-2.390	0.239,-2.422	0.294,-2.488
Cd	0.061,-0.301	0.110,-0.379	0.245,-0.409	0.364,-0.446	0.690,-0.333	0.921,-0.278
Te	0.006,-1.550	0.011,-1.922	0.029,-2.088	0.038,-2.159	0.069,-1.969	0.117,-1.615
Ba	0.004,-1.228	0.010,-1.721	0.020,-1.822	0.027,-1.813	0.050,-1.658	0.081,-1.393
La	0.019,-2.564	0.051,-3.977	0.121,-4.240	0.210,-4.086	0.322,-3.777	0.416,-3.536
Ce	0.040,-2.826	0.106,-4.210	0.207,-4.481	0.329,-4.503	0.526,-4.234	0.677,-3.908

Table 6.4: continuation of Table 6.3.

Pr	0.035,-2.470	0.088,-3.600	0.166,-3.856	0.246,-3.891	0.357,-3.821	0.554,-3.605
Nd	0.021,-2.403	0.062,-3.730	0.157,-3.834	0.308,-3.858	0.456,-3.972	0.554,-3.776
Eu	0.010,-1.188	0.021,-1.599	0.055,-1.790	0.125,-1.734	0.191,-1.516	0.275,-1.357
Gd	0.017,-3.615	0.043,-5.278	0.085,-5.539	0.129,-5.542	0.219,-5.281	0.330,-4.894
Tb	0.027,-2.642	0.067,-3.837	0.142,-4.061	0.202,-3.963	0.319,-3.614	0.409,-3.340
Dy	0.027,-2.672	0.068,-3.683	0.158,-4.026	0.199,-3.866	0.279,-3.728	0.404,-3.139
Ho	0.028,-2.672	0.069,-3.851	0.162,-4.020	0.199,-3.927	0.283,-3.689	0.406,-3.248
Er	0.028,-2.681	0.069,-3.729	0.162,-3.947	0.196,-3.823	0.276,-3.654	0.406,-3.278
Tm	0.030,-2.762	0.069,-3.659	0.168,-3.992	0.217,-3.801	0.289,-3.658	0.397,-3.268
Yb	0.012,-0.958	0.022,-1.224	0.056,-1.366	0.122,-1.191	0.188,-1.044	0.264,-0.965
Lu	0.040,-2.683	0.087,-3.659	0.155,-3.911	0.210,-3.900	0.340,-3.630	0.482,-3.254
Hf	0.036,-4.599	0.057,-5.285	0.209,-6.329	0.279,-6.266	0.399,-5.886	0.680,-4.554
Ta	0.066,-5.540	0.109,-6.815	0.210,-7.729	0.409,-7.719	0.624,-6.877	0.903,-6.333
W	0.111,-6.179	0.149,-6.886	0.256,-7.726	0.465,-7.681	0.689,-6.553	0.953,-4.666
Re	0.307,-4.531	0.441,-5.847	0.680,-7.039	0.803,-7.237	1.102,-6.969	1.636,-5.140
Os	0.106,-6.174	0.206,-7.540	0.326,-7.866	0.394,-7.945	0.570,-7.555	0.908,-5.803
Ir	0.089,-5.498	0.106,-6.040	0.228,-7.004	0.342,-7.142	0.486,-6.271	0.667,-5.735
Pt	0.025,-3.842	0.035,-4.280	0.094,-5.002	0.149,-4.728	0.188,-4.327	0.250,-3.495
Au	0.015,-1.932	0.023,-2.231	0.075,-2.492	0.108,-2.276	0.134,-2.038	0.179,-1.590
Tl	0.007,-1.336	0.013,-1.611	0.029,-1.661	0.062,-1.476	0.091,-1.268	0.133,-1.001
Pb	0.0004,-1.813	0.0006,-2.159	0.0010,-2.454	0.0016,-2.537	0.0046,-2.491	0.0125,-1.686

Table 6.5: (left part) Structures used to fit EAM potentials for pure elements, continued in Table 6.6. The EAM potentials are fitted to the *ab initio* energies in body-centered cubic (BCC), face-centered cubic (FCC), hexagonal close-packed (HEX), diamond structure (DIA), and groundstate structure at various pressures obtained by expanding/compressing the equillibrium lattice constant a by a factor from 0.9 to 1.16 corresponding to a range of charge density from ρ_{max} to ρ_{min}. (right part) Lattice constansts calculated using the fitted parameters. The literature values a_{LIT} are taken from [146].

Z	Name	Struct.	$\rho_{min} \rightarrow \rho_{max}$ (Å^{-3})	a_{LIT} (Å)	a_{VASP} (Å)	a_{EAM} (Å)
3	Li	BCC	0.104 → 0.441	3.49	3.44	3.44
4	Be	HEX	0.268 → 1.437	2.29	2.27	2.24
6	C	DIA	0.329 → 2.038	3.57	3.57	3.57
11	Na	BCC	0.027 → 0.163	4.23	4.19	4.19
12	Mg	HEX	0.014 → 0.174	3.21	3.19	3.16
13	Al	FCC	0.098 → 0.312	4.05	4.04	4.00
14	Si	DIA	0.060 → 0.443	5.43	5.46	5.46
19	K	BCC	0.013 → 0.089	5.23	5.29	5.29
20	Ca	FCC	0.014 → 0.186	5.58	5.54	5.54
21	Sc	HEX	0.064 → 0.441	3.31	3.30	3.34
22	Ti	HEX	0.150 → 0.845	2.95	2.92	2.92
23	V	BCC	0.263 → 1.320	3.02	2.98	2.98
24	Cr	BCC	0.126 → 0.765	2.88	2.84	2.84
26	Fe	BCC	0.213 → 1.221	2.87	2.83	2.83
27	Co	HEX	0.361 → 0.974	2.51	2.47	2.45
28	Ni	FCC	0.374 → 0.983	3.52	3.49	3.46
29	Cu	FCC	0.113 → 0.519	3.61	3.64	3.64
30	Zn	HEX	0.777 → 7.050	2.66	2.71	2.71
32	Ge	DIA	0.056 → 0.306	5.66	5.79	5.79
37	Rb	BCC	0.004 → 0.048	5.59	5.65	5.65
38	Sr	FCC	0.009 → 0.097	6.08	6.05	6.05
39	Y	HEX	0.036 → 0.282	3.65	3.64	3.64
40	Zr	HEX	0.073 → 0.511	3.23	3.22	3.22
41	Nb	BCC	0.050 → 0.390	3.30	3.31	3.31
42	Mo	BCC	0.055 → 0.463	3.15	3.15	3.12
43	Tc	HEX	0.147 → 0.993	2.74	2.76	2.76
44	Ru	HEX	0.084 → 0.558	2.70	2.73	2.70
45	Rh	FCC	0.072 → 0.469	3.80	3.84	3.84
46	Pd	FCC	0.017 → 0.195	3.89	3.96	3.96
47	Ag	FCC	0.034 → 0.256	4.09	4.16	4.16
48	Cd	HEX	0.076 → 0.855	2.98	3.09	3.03
52	Te	HEX	0.007 → 0.108	4.45	4.06	4.02

Table 6.6: continuation of Table 6.5.

56	Ba	BCC	0.007 → 0.074	5.02	5.02	5.02
57	La	HEX	0.042 → 0.331	3.75	3.74	3.74
58	Ce	FCC	0.096 → 0.610	5.16	4.74	4.74
59	Pr	HEX	0.076 → 0.502	3.67	3.45	3.45
60	Nd	HEX	0.068 → 0.457	3.66	3.56	3.56
63	Eu	BCC	0.029 → 0.232	4.61	4.46	4.41
64	Gd	HEX	0.037 → 0.303	3.64	3.62	3.62
65	Tb	HEX	0.049 → 0.362	3.60	3.62	3.62
66	Dy	HEX	0.047 → 0.345	3.59	3.61	3.61
67	Ho	HEX	0.048 → 0.356	3.58	3.59	3.63
68	Er	HEX	0.047 → 0.352	3.56	3.58	3.61
69	Tm	HEX	0.049 → 0.367	3.54	3.55	3.55
70	Yb	FCC	0.023 → 0.202	5.49	5.29	5.29
71	Lu	HEX	0.061 → 0.425	3.51	3.48	3.48
72	Hf	HEX	0.073 → 0.530	3.20	3.20	3.20
73	Ta	BCC	0.091 → 0.692	3.31	3.32	3.32
74	W	BCC	0.105 → 0.794	3.16	3.19	3.19
75	Re	HEX	0.378 → 1.509	2.76	2.78	2.78
76	Os	HEX	0.114 → 0.861	2.74	2.76	2.73
77	Ir	FCC	0.068 → 0.629	3.84	3.88	3.80
78	Pt	FCC	0.025 → 0.236	3.92	3.98	3.98
79	Au	FCC	0.016 → 0.167	4.08	4.17	4.17
81	Tl	HEX	0.011 → 0.112	3.46	3.54	3.54
82	Pb	FCC	0.001 → 0.011	4.95	5.02	5.02

Chapter 7

Effects of Mo on the thermodynamics of Fe:Mo:C nanocatalyst for single-walled carbon nanotube growth

Among the established methods for single-walled carbon nanotubes (SWCNTs) synthesis [147, 148, 149], catalytic chemical vapor decomposition (CCVD) technique is preferred for growing nanotubes on a substrate at a target position due to its relatively low synthesis temperature. Temperature as low as $\sim$ 450 ^{o}C was reported by using hydrocarbon feedstock with exothermic catalytic decomposition reaction [150, 151]. Critical factors for the efficient growth via CCVD are the compositions of the interacting species, the preparation of the catalysts, and the synthesis conditions. Efficient catalysts must have long active lifetimes (with respect to feedstock dissociation and nanotube growth), high selectivity and be less prone to contamination. Common factors that lead to reduction in catalytic activity are deactivation (e.g. due to coating with carbon or nucleation of inactive phases) [152, 153, 154] and thermal sintering (e.g. caused by highly exothermic reactions on the clusters surface [150, 151, 155] with insufficient heat [156]).

Metal alloy catalysts, such as Fe:Co, Co:Mo, and Fe:Mo, improve the growth of CNTs [157, 158, 159, 160, 162, 163], because the presence of more than one metal species can significantly enhance the activity of a catalyst [159, 164], and can prevent catalyst particle aggregation [163, 164]. In the case of Fe:Mo nanoparticles supported on Al_2O_3 substrates, the enhanced catalyst activity has been shown to be larger than the linear combination of the individual Fe/Al_2O_3 and Mo/Al_2O_3 activities [159, 160].

This is explained in terms of substantial intermetallic interaction between Mo, Fe and C [159, 165, 166]. The addition of Mo in mechanical alloying of powder Fe and C mixtures promotes solid state reactions even at low Mo concentrations by forming ternary phases, such as the $(Fe,Mo)_{23}C_6$ and $Fe_2(MoO_4)_3$ type carbides [167]. It has been found that low Mo concentration in Fe:Mo is favored for growing SWCNTs (on Al_2O_3 substrates) since the presence, after activation, of the phase $Fe_2(MoO_4)_3$ can lead to the formation of small metallic clusters [168]. Considering the vapor-liquid-solid model (VLS), which is the most probable mechanism for CNT growth [159, 169]. The metallic nanoparticles are very efficient catalysts when they are in the liquid or viscous states, probably due to considerable carbon bulk-diffusion in this phase (compared to surface or sub-surface diffusion). Generally, unless stable intermetallic compounds form, alloying metals reduce the melting point below those of the constituents [165, 166]. Hence, to improve the yield and quality of nanotubes, one can tailor the composition of the catalyst particle to move its liquidus line below the synthesis temperature [159]. However, identifying the perfect alloy composition is non trivial. In fact, the presence of more than two metallic species allows for the possibility of different carbon pollution mechanisms by thermodynamic promotion of ternary carbides. In this Chapter, we study the phase diagram of Fe:Mo:C system and the possible roles of Mo in the catalytic properties of Fe:Mo.

7.1 Size-pressure approximation

Determining the thermodynamic stability of different phases in nanoparticles of different sizes with *ab initio* calculations is computationally expensive. We develop a simple model, called the "size-pressure approximation", which allows one to estimate the phase diagram at the nanoscale starting from bulk calculations under pressure [152]. Surface curvature and superficial dangling bonds on nanoparticles are

responsible for internal stress fields which modify the atomic bond lengths. As a first approximation, where all surface effects that are not included in the curvature are neglected, we can map the particle radius R to the pressure P by equating the deviation from the bulk value of the average bond lengths due to surface curvature (in the case of particle) and pressure (in the case of bulk). For spherical clusters, the phenomenon can be modeled with the Young-Laplace equation $P = 2\gamma/R$ where the proportionality constant γ can be calculated with *ab initio* methods. In our study, since the concentration of Mo in Fe:Mo is small, we use the "size-pressure approximation" of Fe particle.

Figure 7.1 shows the implementation of the "size-pressure approximation" for Fe nanoparticles. On the left hand side we show the *ab initio* calculations of the deviation of the average bond length inside the cluster $\Delta d_{nn} \equiv d^0_{nn} - d_{nn}$ ($d^0_{nn} = 0.2455$ nm is our bulk bond length), for body-centered cubic (BCC) particles of size N = 59, 113, 137, 169, 307 and ∞ (bulk) as a function of the inverse radius ($1/R$). The particles were created by intersecting a BCC lattice with different size spheres. The particle radius is defined as $1/R \equiv 1/N_{scp} \sum_i 1/R_i$ where the sum is taken over the atoms belonging to the surface convex polytope (N_{scp} vertices) and R_i are the distances to the geometric center of the cluster. The left straight line is a linear interpolation between $1/R$ and Δd_{nn} calculated with the constraint of passing through $1/R = 0$ and $\Delta d_{nn} = 0$ ($N = \infty$, bulk). The right hand side shows the *ab initio* value of d_{nn} in bulk BCC Fe as a function of hydrostatic pressure, P. The straight line is a linear interpolation between P and Δd_{nn} calculated with the constraint of passing through $P = 0$ and $\Delta d_{nn} = 0$ (bulk lattice). By following the colored dashed paths indicated by the arrows we can map the analysis of nanoparticles stability as a function of R onto bulk stability as a function of P, and obtain the relation between the radius of particle/nanotube and the effective pressure $P \cdot R = 2.46$ GPa $\cdot$ nm. It is important

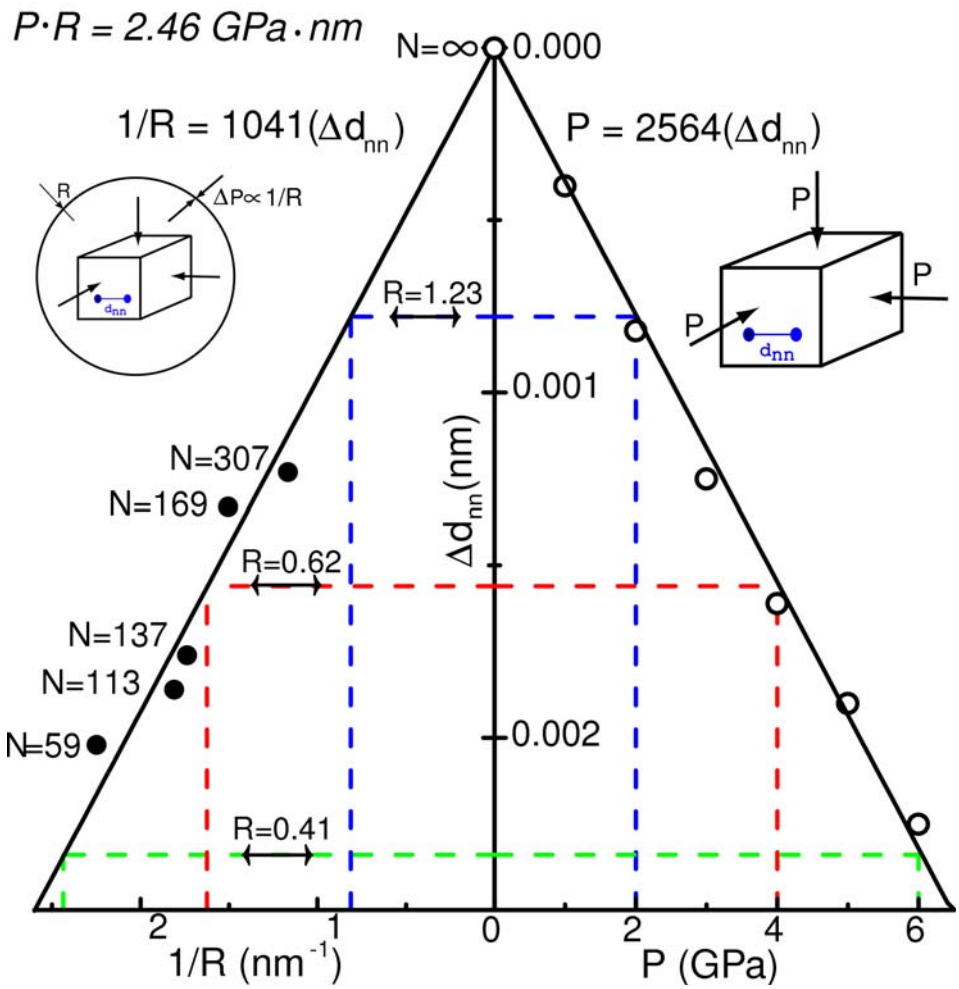

Figure 7.1: (color online). Size-pressure approximation for Fe nanoparticles obtained by equating the deviation of average bond length from the bulk value due to curvature $1/R$ (in the case of particle) and due to pressure P (in the case of bulk).

to mention that our $\gamma = 1.23$ J/m^2 is not a real surface tension but an *ab initio* fitting parameter describing size-induced stress in nanoparticles. With this γ, we deduce the Fe-Mo-C phase diagram of nanoparticles of radius R from *ab initio* calculations of the bulk material under pressure P.

7.2 Fe-Mo-C phase diagram under pressure

Simulations are performed with VASP as described in Section 2.2. The hydrostatic pressure estimated from the pressure-size model is implemented as Pulay stress [170]. Ternary phase diagrams are calculated using BCC-Mo, BCC-Fe and SWCNTs as references (pure-Fe phase is taken to be BCC because our simulations are aimed at the low temperature regime of catalytic growth). The reference SWCNTs have the same diameter of the particle to minimize the curvature-strain energy. In fact, CVD experiments of SWCNT growth from small ($\sim$ 0.6-2.1 nm) particles indicate that the diameter of the nanotube is similar to the diameter of the catalyst particle from which it grows. In some experiments where the growth mechanism is thought to be root-growth, the ratio of the catalyst particle diameter to SWCNT diameter is ~ 1.0, whereas in experiments involving pre-made floating catalyst particles this ratio is $\sim$ 1.6 [171]. Formation energies are calculated with respect to decomposition into the nearby stable phases, depending the position in the ternary phase diagram.

Binary and Ternary phases are included if they are stable in the temperature range used in CVD growth of SWCNTs or if they have been reported experimentally during or after the growth [165, 166, 172]. Thus, we include the binaries Mo_2C, Fe_2Mo and Fe_3C. In addition, since our Fe-rich Fe:Mo experiments were performed with compositions close to Fe_4Mo [159], we include a random phase Fe_4Mo generated with the special quasi-random structure formalism (SQS). Bulk ternary carbides, which have been widely investigated due to their importance in alloys and steel, can be considered as derivatives of binary structures with extra C atoms in the interstices of the basic metal alloy structures. Three possible ternary phases have been reported for bulk Fe-Mo-C [173] and they are referred as τ_1 (M_6C), τ_2 (M_3C) and τ_3 ($M_{23}C_6$) (M is the metal species). For simplicity, we follow the same nomenclature. τ_1 is the wellknown M_6C phase, which has been observed experimentally as Fe_4Mo_2C and

Fe_3Mo_3C structures (η carbides) [174, 175]. Both of these structures are FCC but have different lattice spacings. Our calculations show that the most stable variant τ_1 is Fe_4Mo_2C, and we denote it as τ_1 henceforth. τ_2 is the Fe_2MoC phase, which has an orthorhombic symmetry distinct from that of Fe_3C [176, 177]. We consider $Fe_{21}Mo_2C_6$ as the third τ_3 FCC phase [178]. We use the $Cr_{23}C_6$ as the prototype structure [179] where Fe and Mo substitute for Cr. Although $M_{23}C_6$ type phases do not appear in the stable C-Fe or C-Mo systems, they have been reported in ternary C-Fe-Mo systems and also appear as transitional products in solid state reactions [173]. Time-temperature precipitation diagrams of low-C steels have identified τ_2, τ_3 and τ_1 as low-temperature, metastable and stable carbides, respectively [180]. Furthermore, τ_2 carbides precipitate quickly due to carbon-diffusion controlled reaction while τ_3 carbides precipitate due to substitutional-diffusion controlled reactions. The latter phenomenon, requiring high temperature, longer times and producing metastable phases is not expected to enhance the catalytic deactivation of the nanoparticle. In summary, as long as the presence of carbon does not lead to excessive formation of Fe_3C and τ_2), the catalyst should remain active for SWCNT growth.

Figure 7.2 shows the phase diagram at zero temperature of nanoparticles of radii $R \sim \infty$, 1.23, 0.62, 0.41 nm, calculated at P = 0, 2, 4, and 6 GPa, respectively. Stable and unstable phases are shown as black squares and red dots, respectively. The solid green lines connect the stable phases. The numbers "1"..."8" in panels (c) and (d) indicate the intersections between the phases' boundary and the dotted lines representing the path of carbon pollution to the two test phases Fe_4Mo and FeMo. Fe_4Mo has been reported to be an effective catalyst composition [159] while FeMo represents a hypothetical Fe:Mo particle with a Mo content larger than 33%.

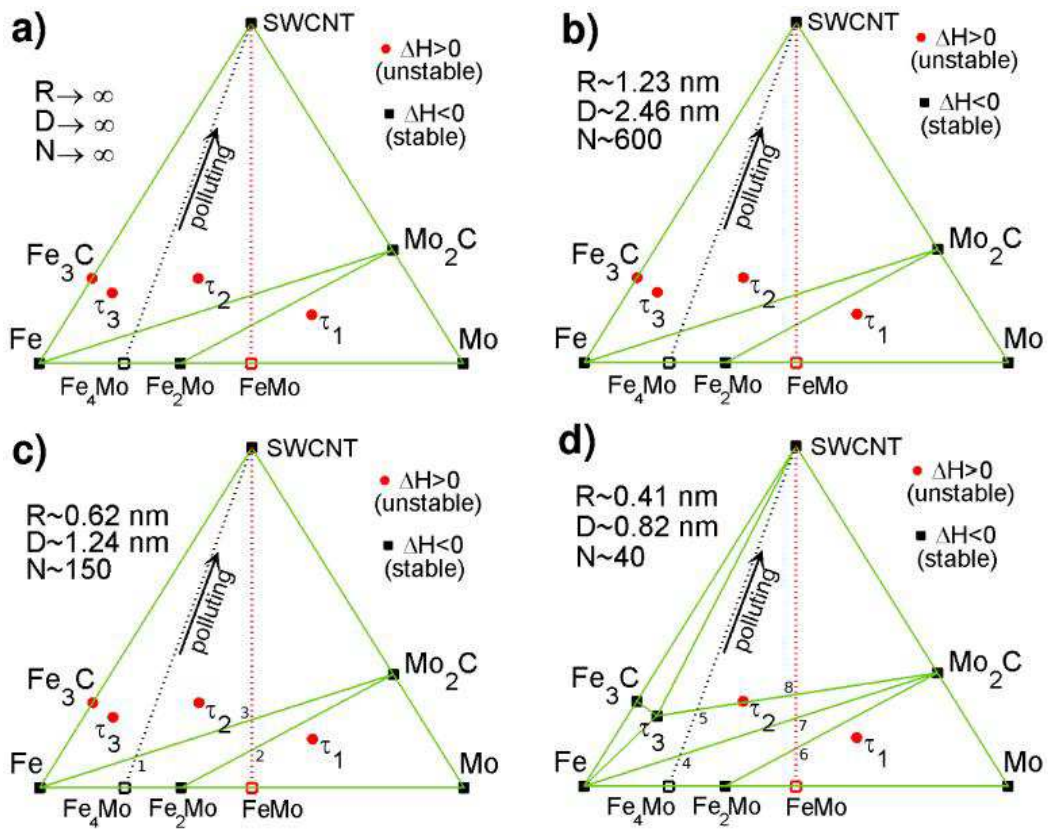

Figure 7.2: (color online). Ternary phase diagram for Fe-Mo-C nanoparticles of $R \sim \infty$, 1.23, 0.62, 0.41 nm.

7.3 Fe_4Mo particles

An advantage of an Fe_4Mo particle has over a pure Fe particle is that the $[Fe_{4/5}Mo_{1/5}]_{1-x}$-C_x line does not intercept any carbide (Fe_3C, τ_3, τ_2). This implies that, at least at low temperatures, there is a surplus of unbounded metal (probably even at high temperatures since the line is far from all of the competing stable phases). This is illustrated in figure 7.3, which shows the fractional evolution of species as one progresses along the $[Fe_{4/5}Mo_{1/5}]_{1-x}$-C_x line in figure 7.2.

For a large Fe_4Mo particle ($R \geq 0.62$ nm), the decomposition into stable phases is shown in figure 7.3(a)). At concentrations between $0 < x_c < 0.09$ there is available free Fe for catalysis, however there is no carbon content in the particle. At higher

concentrations, the particle starts to contain free carbon while still providing free Fe. Therefore, a steady state growth of SWCNTs is possible from large Fe_4Mo particles. Figure 7.3(b) shows the decomposition for a small Fe_4Mo particle ($R \leq 0.41$ nm)). In this case, the free Fe is consumed and transformed into τ_3 carbide before the particle has enough free carbon, hence, the SWCNT growth will not occur. We can estimate the minimum size of the particle by calculting the pressure at which τ_3 starts to form. By linear interpolation, we obtain $R = 0.52$ nm. This size is smaller than that if one uses pure Fe nanocatalyst ($R = 0.56$ nm) [152, 153].

7.4 FeMo particles

Figure 7.4 shows the decomposition analysis for FeMo particle. For a large particle of size $R \geq 0.62$ nm, The particle contains free Fe and carbon only after the concentration x_c is larger than 0.2 which then permits the growth of the nanotube. Comparing to the Fe_4Mo particle, since the fraction of Fe in the FeMo particle is considerably smaller than in Fe_4Mo, the expected yield is lower and the synthesis temperature needs to be increased (to overcome the reduced fraction of catalytically active free Fe). Small FeMo particles ($R \leq 0.41$ nm) are similar to small Fe_4Mo clusters. Nucleation of τ_3 and the abscence of free Fe and excess carbons indicate that the particles are catalytically inactive. The minimum size of FeMo and Fe_4Mo particles able to grow nanotube is the same since it is determined by the stabilization of the same τ_3 carbide.

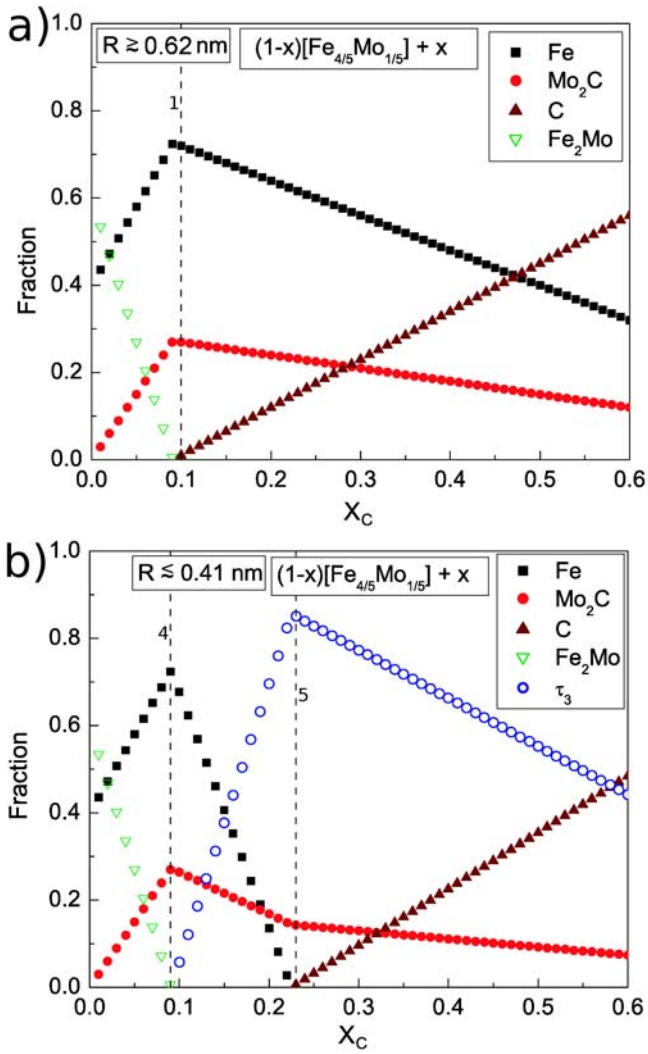

Figure 7.3: (color online). a) Fraction of species for catalyst composition $[Fe_{4/5}Mo_{1/5}]_{1-x}$-C_x and nanocatalyst of $R \geq 0.62$ nm. The dashed vertical line, labeled as "1", represents $[Fe_{4/5}Mo_{1/5}]_{1-x}$-C_x crossing the boundary phase Fe↔Mo_2C, as shown in figure 7.2(c). b) Fraction of species for catalyst composition $[Fe_{4/5}Mo_{1/5}]_{1-x}$-C_x and nanocatalyst of $R \leq 0.41$ nm. The dashed vertical lines, labeled as "4" and "5", represent $[Fe_{4/5}Mo_{1/5}]_{1-x}$-C_x crossing the boundary phases Fe⟷Mo_2C and τ_3, as shown in figure 7.2(d).

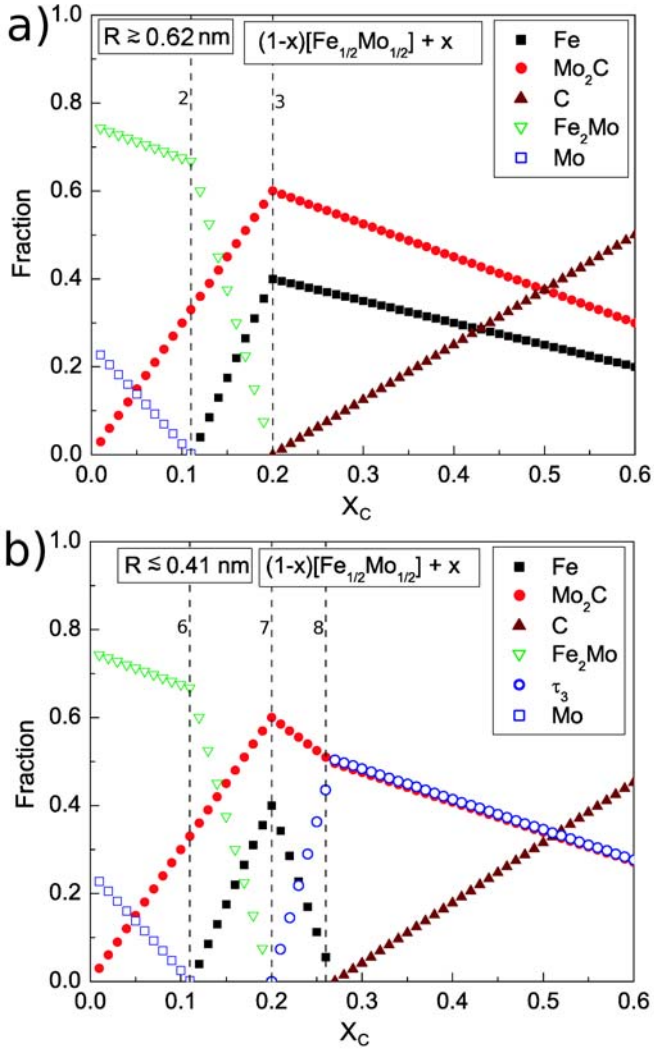

Figure 7.4: (color online). a) Fraction of species for catalyst composition $[Fe_{1/2}Mo_{1/2}]_{1-x}$-C_x and nanocatalyst of $R \geq 0.62$ nm. The dashed vertical line, labeled as "2" and "3", represent $[Fe_{1/2}Mo_{1/2}]_{1-x}$-C_x crossing the boundary phase $Fe_2Mo \leftrightarrow Mo_2C$ and $Fe \leftrightarrow Mo_2C$, as shown in figure 7.2(c). b) Fraction of species for catalyst composition $[Fe_{1/2}Mo_{1/2}]_{1-x}$-C_x and nanocatalyst of $R \leq 0.41$ nm. The dashed vertical lines, labeled as "6", "7", and "8", represent $[Fe_{1/2}Mo_{1/2}]_{1-x}$-C_x crossing the boundary phases $Fe_2Mo \leftrightarrow Mo_2C$, $Fe \longleftrightarrow Mo_2C$, and $\tau_3 \leftrightarrow Mo_2C$, as shown in figure 7.2(d).

Chapter 8

Conclusions

We have presented the results of our computational studies on adsorptions of hydrocarbons (alkanes, benzene) and rare gases on a decagonal surface of Al-Ni-Co quasicrystal (d-AlNiCo). *Ab initio* calculations show that upon the adsorptions, the surface of the d-AlNiCo does not undergo relaxations and that there are no dissociations of the adsorbates. The simulations of thin film growth of these adsorbates have been performed in the grand canonical ensemble using Monte Carlo method. We use semiempirical pair interactions for the rare gases and develop classical many-body potentials based on embedded-atom method (EAM) for the hydrocarbons. All of the simulated atoms/molecules wet the substrate as a consequence of comparable strengths between the substrate-adsorbate and adsorbate-adsorbate. Another consequence is the wide range of overlayer structures observed in these systems. Methane monolayer has a quasicrystalline pentagonal order commensurate with the substrate. Propane forms a disordered structure. Hexane and octane monolayers show 2-dimensional close-packed features consistent with their bulk structure. Benzene forms a pentagonal monolayer at low and moderate temperatures which transforms into a triangular lattice at high temperatures. Similar structural transition also occurs in xenon monolayer, however in this case, the transition is observed at all temperatures below the triple-point temperature and as a function of pressure. We have characterized that such transition is first-order with an associated latent heat. Smaller noble gases such as Ne, Ar, Kr form monolayers with mixed pentagonal and triangular patterns and do not show any structural transitions.

By systematically simulating test noble gases of various sizes and strengths, we

observe that the relative strengths between the competing interactions determine the growth mode. Agglomeration occurs when the adsorbate-adsorbate interactions are much stronger than the substrate-adsorbate ones. In the comparable strength regime, a layer-by-layer film growth is observed. In this regime, the mismatch between the size of the gas and the substrate's characteristic length plays a major role in affecting the structure of the adsorbed films. In general, on the d-AlNiCo substrate, we found that structural transition from 5- to 6-fold occurs when the gas size is larger than $\lambda/0.944$ (λ represents the average row-row spacing in the quasicrystalline plane of the d-AlNiCo). Even though this rule is derived from rare gases, it is consistent with methane, benzene, hexane and octane. Therefore, it might be useful as a guidance in the search for suitable quasicrystalls for which alkanes (as the main constituent of oil lubricants) will form quasiperiodic structures for the low-friction coating applications.

It is a natural extension of this work to investigate other quasicrystalls with larger characterictic lengths than the d-AlNiCo used in this study. In fact, d-AlNiCo is stable in many decorations depending on the concentration of Al, Ni, and Co. Due to the stripe nature in the close-packed structure of linear alkanes, the film structure of these molecules on one dimensional quasicrystals is interesting to study. Two surfaces with stripe pattern will be commensurate only when the stripes are perfectly alligned, therefore, one dimensional quasicrystalls might be good candidate for low-friction coatings.

Bibliography

[1] Tsai A P, Inoue A and Masumoto T 1987 *Jap. J. Appl. Phys.* **26** L1505

[2] Tsai A P, Inoue A and Masumoto T 1989 *Acta. Met.* b**37** 1443

[3] Tsai A P, Inoue A, Yokoyama Y and Masumoto T 1990 *Mater. Trans. Japan Inst. Met.* **32** 98

[4] Feuerbacher M, Thomas C and Urban K 2003 *Quasicrystals: Structure and Physical Properties* ed Trebin H R (Wiley-VCH) ch 1

[5] Dubois J M 2005 *Usefull Quasicrystals* World Scientific

[6] Ko J S, Gellman A J, Lograsso T A, Jenks C J and Thiel P A 1999 *Surface Science* **423** 243

[7] McFadden C F and Gellman A J 1995 *Langmuir* **11** 273

[8] Dubois J M, Brunet P and Belin-Ferre 2000 *Quasicrystals: Current Topics* ed Belin-Ferre, Berger C, Quiquandon M and Sadoc A (World Scientific, singapore) p 498; Brunet P, Zhang L, Sordelet D J, Besser M F and Dubois J M 2000 *Quasicrystals* ed Gähler F, Kramer P, Trebin H -R and Urban K *Mat. Sci. Eng. A* **74** 294-296

[9] Dong C, Zhang L -M, Belin-Ferre, Brunet P and Dubois J M 2001 *Mat. Sci. Eng. A* bf 172 304-306

[10] Dubois J M 2005 *Usefull Quasicrystals* World Scientific p 400

[11] Park J Y, Ogletree D F, Salmeron M, Ribeiro R A, Canfield P C, Jenks C J, Thiel P A 2005 *Science* **309** 1354

[12] Hirano M and Shinjo K 1990 *Phys. Rev. B* **41** 11837

[13] Dienwiebel M, Verhoeven G S, Pradeep N, Frenken J W M, Heimberg J A and Zandbergen H W 2004 *Phys. Rev. Lett.* **92** 126101

[14] Fisher I R, Kramer M J, Islam Z, Ross A R, Kracher A, Weiner T, Sailer M J, Goldman A I and Canfield P C 1999 *Philosophical Magazine B* **79** 425

[15] Ferralis N, Pussi K, Gierer M, Cox E J, Ledieu J, Fisher I R, Jenks C J, Lindroos M, McGrath R and Diehl R D 2004 *Phys. Rev. B* **69** 153404

[16] Pussi K, Ferralis N, Mihalkovic M, Widom M, Curtarolo S, Gierer M, Jenks C J, Fisher I R and Diehl R D 2006 *Phys. Rev. B* **73** 184203

[17] Daw M S and Baskes M L 1983 *Phys. Rev. Lett.* **50** 1285

[18] Slater J C 1929 *Phys. Rev.* **34** 1293

[19] Hohenberg P and Kohn W 1964 *Phys. Rev. B* **136** B864

[20] Perdew J P and Wang Y 1986 it Phys. Rev. B **33** 8800

[21] Perdew J P 1986 it Phys. Rev. B **33** 8822

[22] Wang Y and Perdew J P 1991 it Phys. Rev. B **44** 13298

[23] Becke A D 1988 *Phys. Rev. A* **38** 3098

[24] Lee C, Yang W and Parr R G 1988 *Phys. Rev. B 37* 785

[25] Perdew J P, Burke K and Enzerhof M 1996 *Phys. Rev. Lett.* **77** 3865

[26] Perdew J P, Burke K and Enzerhof M 1997 *Phys. Rev. Lett.* **78** 1396

[27] Slater J C 1937 *Phys. Rev.* **51** 846

[28] Slater J C 1953 *Phys. Rev.* **92** 603

[29] Andersen O K 1975 *Phys. Rev. B* **12** 3060

[30] Koelling D D and Arbman G O 1975 *J. Phys. F* **5** 2041

[31] Herring C 1940 *Phys. Rev.* **57** 1169

[32] Antoncik E 1959 *J. Phys. Chem. Solids* **10** 314

[33] Phillips J C and Kleinman L 1959 *Phys. Rev.* **116** 880

[34] Kresse G and Hafner J 1993 *Phys. Rev. B* **47** 558

[35] Kresse G and Furthmuller J 1996 *Comput. Mater. Sci.* **6** 15

[36] Kohanoff J 2006 *Electronic Structure Calculations for Solids and Molecules* (Cambrigde University Press) p 86

[37] Perdew J P and Wang Y 1992 *Phys. Rev. B* **45** 13244

[38] Blöchl P E 1994 *Phys. Rev. B* **50** 17953

[39] Kresse G and Joubert J 1999 *Phys. Rev. B* **59** 1758

[40] Monkhorst H J and Pack J D 1976 *Phys. Rev. B* **13** 5188

[41] Lennard-Jones J E 1924 *Proc. Roy. Soc. London A.* **106** 463

[42] Morse P M 1929 *Phys. Rev. B* **34** 57

[43] Leckband D and Israelachvili J 2001 *Quart. Rev. Biophys.* **34** 105

[44] van Duin A C T, Dasgupta S, Lorant F and Goddard W A III 2001 *J. Phys. Chem. A* **105** 9396

[45] Zhang Q, Cagin T, van Duin A C T and Goddard W A III 2004 *Phys. Rev. B* **69** 045423

[46] Buehler M J, van Duin A C T and Goddard W A III 2006 *Phys. Rev. Lett.* **96** 095505

[47] Sanchez J M, Ducastelle F and Gratias D 1984 *Physica A* **128** 334

[48] Fontaine D de 1979 *Solid State Physics* ed Ehrenreich H, Seitz F and Turnbull D (Academic Press) **34** p 73

[49] Fontaine D de 1994 *Solid State Physics* ed Ehrenreich H and Turnbull D (Academic Press) **47** p 33

[50] Daw M S and Baskes M L 1984 *Phys. Rev. Lett.* **29** 6443

[51] Ponder J W and Case D A 2003 Force *Adv. Prot. Chem.* **66** 27

[52] Parr R G and Yang W 1989 *Density Functional Theory of Atoms and Molecules* (Oxford University Press) p 47

[53] Kohn W and Sham L J 1965 *Phys. Rev. B* **140** 1133

[54] Cai J 1999 *Phys. Stat. Sol. (b)* **212** 9

[55] Baskes M I, Nelson J S and Wright A F 1989 *Phys. rev. B* **40** 6085

[56] Haftel M I, Andreadis T D, Lill J V and Eridon J M 1990 *Phys. Rev. B* **42** 11540

[57] Dodson B W 1986 *Phys. Rev. B* **35** 880

[58] Ercolessi F, Tosatti E and Parrinello M 1986 *Phys. Rev. Lett.* **57** 719

[59] Haftel M I 1993 *Phys. Rev. B* **48** 2611

[60] Luedtke W D and Landman U 1991 *Phys. Rev. B* **44** 5970

[61] Haftel M I, Rosen M, Franklin T and Hetternmann M 1996 *Phys. Rev. B* **53** 8007

[62] Chang C M, Wei C M and Chen S P 2000 *Phys. Rev. Lett.* **85** 1044

[63] Liu C L, Cohen J M, Adams J B and Voter A F 1991 *Surf. Sci.* **253** 334

[64] Herman A 2005 *Int. J. Nanotech.* **2** 215

[65] Mishin Y, Farkas D, Mehl M J and Papaconstantopoulos D A 1999 *Phys. Rev. B* **59** 3393

[66] Nelder J A and Mead R 1965 *The Computer Journal* **7** 308

[67] Frenkel D and Smith B 2002 *Understanding Molecular Simulations: From Algorithms to Application* (New York: Academic)

[68] Allen M P and Tildesley D J 1987 *Computer Simulation of Liquids* (Oxford: Oxford U P)

[69] Bruch L W, Cole M W and Zaremba E 1997 *Physical Adsorption* (Oxford: Oxford University Press)

[70] Setyawan W, Ferralis N, Diehl R D, Cole M W and Curtarolo S 2006 *Phys. Rev. B* **74** 125425

[71] Diehl R D, Setyawan W, Ferralis N, Trasca R A, Cole M W and Curtarolo S 2007 *Phil. Mag.* **87** 2973

[72] Bojan M J, Stan G, Curtarolo S, Steele W A and Cole M W 1999 *Phys. Rev. E* **59** 864

[73] Rotenberg E, Theis W, Horn K and Gille P 2000 *Nature* **406** 602

[74] Rotenberg E, Theis W and Horn K 2002 *J. Alloys Compd.* **342** 348

[75] Dubois J M 1993 *Physica Scripta* **T49** 17

[76] Ko J S, Gellman A J, Lograsso T A, Jenks C J and Thiel P A 1998 *Surf. Sci.* **423** 243

[77] Park J Y, Ogletree D F, Salmeron M, Jenks C J and Thiel P A 2004 *Tribology Letters* **17** 629

[78] McGrath R, Grimm U and Diehl R D 2004 *Physics World* **17** 23

[79] McGrath R, Ledieu J, Cox E J and Diehl R D 2002 *J. Phys.: Condensed Matter* **14** R119

[80] McGrath R, Ledieu J, Cox E J, Haq S, Diehl R D, Jenks C J, Fisher I, Ross A R and Lograsso T A 2002 *J. Alloys Compd.* **342** 432

[81] Ledieu J, Hoeft J-T, Reid D E, Smerdon J, Diehl R D, Lograsso T A, Ross A R and McGrath R 2004 *Phys. Rev. Lett.* **92** 135507

[82] Cai T C, Ledieu J, Fournée V, Lograsso T A, Ross A R, McGrath R and Thiel P A 2003 *Surf. Sci.* **526** 115

[83] Fournée V, Cai T C, Ross A R, Lograsso T A, Evans J W and Thiel P A 2003 *Phys. Rev. B* **67** 033406

[84] Franke K J, Sharma H R, Theis W, Gille P, Ebert P and Rieder K H 2002 *Phys. Rev. Lett.* **89** 156104

[85] Sander L M and Hautman J 1984 *Pys. Rev. B* **29** 2171

[86] Fairobent D K, Saam W F and Sander L M 1982 *Phys. Rev. B* **26** 179

[87] Smith A R, Chao K-J, Niu Q and Shih C K 1996 *Science* **273** 226

[88] Ebert P, Chao K-J, Niu Q and Shih C K 1996 *Phys. Rev. Lett.* **83** 3222

[89] Grimm B, Hövel H, Pollmann M and Reihl B 1999 *Phys. Rev. Lett.* **83** 991

[90] Leatherman G S and Diehl R D 1996 *Phys. Rev. B* **53** 4939

[91] Leatherman G S, Karimi M, Vidali D and Diehl R D 1997 *Phys. Rev. B* **56** 6970

[92] D'Amico K L, Moncton D E, Specht E D, Birgeneau R J, Nagler S E and Horn P M 1984 *Phys. Rev. Lett.* **53** 2250

[93] Fain Jr S C, Chinn M D and Diehl R D 1980 *Phys. Rev. B* **21** 4170

[94] Novaco A D and McTague J P 1977 *Phys. Rev. Lett.* **38** 1286

[95] Tkatchenko A *Phys. Rev. B* 2006 **74** 035428

[96] Noakes T C Q, Bailey P, Draxler M, McConville C F, Ross A R, Lograsso T A, Leung L, Smerdon J A and McGrath R 2006 *J. Phys.: Condens. Matt.* **18** 5017

[97] Cai T C, Ledieu J, McGrath R, Fournée, Lograsso T A, Ross A R and Thiel P A 2003 *Surf. Sci.* **526** 115

[98] Ledieu J, Hoeft J T, Reid D E, Smerdon J A, Diehl R D, Lograsso T A, Ross A R and McGrath R 2004 *Phys. Rev. Lett.* **92** 135507

[99] Ferralis N, Diehl R D, Pussi K, Lindroos M, Fisher I R and Jenks C J 2004 *Phys. Rev. B* **69** 075410

[100] Trasca R A, Ferralis N, Diehl R D and Cole M W 2004 *J. Phys.: Condens. Matt.* **16** S2911

[101] Curtarolo S, Setyawan W, Ferralis N, Diehl R D and Cole M W 2005 *Phys. Rev. Lett.* **95** 136104

[102] Reference [69]: p 67

[103] Zeppenfeld P 2001 *Physics of Covered Surfaces* in *Landolt-Bornstein New Series* Group III **42** ed Bonzel H P (Berlin: Springer) p 67

[104] Vidali G, Ihm G, Kim H-Y and Cole M W 1991 *Surf. Sci. Reports* **12** 133

[105] Chizmeshya A, Cole M W and Zaremba E 1998 *J. Low Temp. Phys.* **110** 677

[106] Vidali G, Ihm G, Kim H -Y and Cole M W 1991 *Surf. Sci. Rep.* **12** 135

[107] Curtarolo S, Stan G, Cole M W, Bojan M J and Steele W A 1999 *Phys. Rev. E* **59** 4402

[108] Curtarolo S, Stan G, Bojan M J, Cole M W and Steele W A 2000 *Phys. Rev. E* **61** 1670

[109] Crawford R K 1977 *Rare Gas Solids* **2** ed Klein M L and Venables J A (London: Academic) p 663

[110] Dai P, Angot T, Ehrlich S N, Wang S-K and Taub H 1994 *Phys. Rev. Lett.* **72** 685

[111] Dai P, Wu Z, Angot T, Wang S-K, Taub H and Ehrlich S N 1999 *Phys. Rev. B* **59** 15464

[112] Unguris J, Bruch L W, Moog E R and Webb M B 1979 *Surf. Sci.* **87** 415

[113] Chinn M D and Fain S C Jr 1977 *Phys. Rev. Lett.* **39** 146

[114] Schabes-Retchkiman P S and Venables J A 1981 *Surf. Sci.* **105** 536

[115] Frank F C and Van der Merwe J H 1949 *Proc. Roy. Soc. London, Ser A* **198** 205 and 216 and **200** 125

[116] Ying S C 1971 *Phys. Rev. B* **3** 4160

[117] Kern K, David R, Zeppenfeld P, Palmer R and Comsa G 1987 *Solid State Comm.* **62** 391

[118] Bruch L W, Cohen P I and Webb M B 1976 *Surf. Sci.* **59** 1

[119] Niebel K F and Venables J A 1976 in *Rare Gas Solids*, edited by Klein M L and Venables J A (Academic Press, New York) **1** 558

[120] Bricheno T and Venables J A 1976 *J. Phys. C: Solid State Physics* **9** 4095

[121] Korpiun P and Luscher E 1977 *Thermal and elastic properties at low pressure*, in *Rare Gas Solids* edited by Klein M L and Venables J A (New York: Academic Press) **II**

[122] Database of alloys *http://alloy.phys.cmu.edu/*

[123] Hirano M, Shinjo K, Kaneko R and Murata Y 1991 *Phys. Rev. Lett.* **67** 2632

[124] Hirano M, Shinjo K, Kaneko R and Murata Y 1997 *Phys. Rev. Lett.* **78** 1448

[125] Ko J S and Gellman A J 2000 *Langmuir* **16** 8343

[126] Dubois J M 1993 *Physica Scripta* **T49** 17

[127] McGrawth R, Ledieu J, Cox E J, Haq S, Diehl R D, Jenks C J, Fisher I, Ross A R and Lograsso T A 2002 *J. of Alloys and Compounds* **342** 432

[128] Hoeft J T, Ledieu J, Haq S, Lograsso T A, Ross A R and McGrawth R 2006 *Philos. Mag.* **86** 869

[129] Tsuzuki S, Uchimaru T and Tanabe K 1993 *J. Mol. Struct.* **280** 273

[130] Tsuzuki S, Uchimaru T, Tanabe K and Kuwajima S 1994 *J. Phys. Chem.* **98** 1830

[131] Califano S, Righini R and Walmsley S H 1979 *Chem. Phys. Lett.* **64** 491

[132] Chelli R, Cardini G, Ricci M, Bartolini P, Righini R and Califano S 2001 *Phys. Chem. Chem. Phys.* **3** 2803

[133] Jalkanen J-P, Mahlanen R, Pakkanen T A and Rowley R L 2002 *J. Chem. Phys.* **116** 1303

[134] Taylor C F and Taylor E S 1966 *The Internal-combustion Engine* **2** (Scranton: International Textbook Company) p 183

[135] Setyawan W, Ferralis N, Diehl R D, Cole M W and Curtarolo S 2007 *J. Phys. Cond. Matt.* **19** 016007

[136] Boese R, Weiss H-C and Bläser D 1999 *Angew. Chem. Int. Ed.* **38** 988

[137] Norman N and Mathisen H 1961 *Acta Chem. Scand.* **15** 1755

[138] Norman N and Mathisen H 1961 *Acta Chem. Scand.* **15** 1747

[139] Broadhurst M G 1962 *J. Res. Nat. Bur. Stand.* **66a** 241

[140] Merle A M, Lamotte M, Risemberg S, Hauw C, Gaultier J and Grivet J P 1977 *Chem. Phys.* **22** 207

[141] David W I F, Ibberson R M, Jeffrey G A and Ruble J R 1992 *Physica B* **180** 587

[142] Brommer P and Gahler F 2007 *Model. and Simul. in Mat. Sci. and Eng.* **15** 295

[143] Chamati H, Papanicolaou N I, Mishin Y and Papaconstantopoulos D A 2006 *Surf. Sci.* **600** 1793

[144] Foiles S M, Baskes M I and Daw M S 1986 *Phys. Rev. B* **33** 7983

[145] Zhou X W, Wadley H N G, Filhol J S and Neurock M N 2004 *Phys. Rev. B* **69** 035402

[146] Ashcroft N W and Mermin N D 1976 *Solid State Physics* (Hartcourt College Publishing)

[147] Journet C, Maser W K, Bernier P, Loiseau A, Chapelle M L de la, Lefrant S, Deniard P, Lee R and Fischer E 1997 *Nature* **388** 756

[148] Thess A, Lee R, Nikolaev P, Dai H, Petit P, Robert J, Xu C, Lee Y H, Rinzler S G, Colbert D T, Tomanek D, Fischer J and Smalley R E 1996 *Science* **273** 483

[149] Li Y, Liu J, Wang Y and Wang Z L 2001 *Chem. Mater.* **13** 1008

[150] Cantoro M, Hofmann S, Pisana S, Scardaci V, Parvez A, Ducati C, Ferrari A C, Blackburn A M, Wang K Y and Robertson J 2006 *Nano Lett.* **6** 1107

[151] Maruyama S, Kojima R, Miyauchi Y, Chiashi S and Kohno M 2002 *Chem. Phys. Lett.* **360** 229

[152] Harutyunyan A R, Awasthi N, Jiang A, Setyawan W, Mora E, Tokune T, Bolton K and Curtarolo S 2008 *Phys. Rev. Lett.* accepted

[153] Curtarolo S, Awasthi N, Setyawan W, Li N, Jiang A, Tan T Y, Mora E, Bolton K and Harutyunyan A R 2008 *Thermodynamics of carbon in iron nanoparticles at low temperature: reduced solubility and size-induced nucleation of cementite, Proc. Computer Simulation Studies in Condensed Matter Physics* **XXI** Eds. Landau D P, Lewis S P and Schüttler H-B, (Springer).

[154] Pernicone N 1991 *Cat. Today* **11** 85

[155] Klinke C, Bonard J M and Kern K 2005 *Phys. Rev. B* **71** 035403

[156] Wang W L, Bai X D, Xu Z, LiuS and Wang E G 2006 *Chem. Phys. Lett.* **419** 81

[157] Moisala A, Nasibulin A G and Kauppinen E I 2003 *J. Phys: Condens. Matter* **15** S3011

[158] Harutyunyan A R, Pradhan B K, Kim U J, Chen G and Eklund P C 2002 *Nano Lett.* **2** 525

[159] Harutyunyan A R, Mora E, Tokune T, Bolton K, Rosen A, Jiang A, Awasthi N and Curtarolo S 2007 *App. Phys. Lett.* **90** 163120

[160] Shah N, Panjala D and Huffman G P 2001 *Energy and Fuels* **15** 1528

[161] Flahaut E, Govindaraj A, Peigney A, Laurent Ch, Rousset A and Rao C N R 1999 *Chem. Phys. Lett.* **300** 236

[162] Ago H, Uehara N, Yoshihara N, Tsuji M, Yumura M, Tomonaga N and Setoguchi T 2006 *Carbon* **44** 2912

[163] Tang S, Zhong Z, Xiong Z, Sun L, Liu L, Lin J, Shen Z X and Tan K L 2001 *Chem. Phys. Lett.* **350** 19

[164] Alvarez W E, Kitiyanan B, Borgna A and Resasco D E 2001 *Carbon* **39** 547

[165] Massalski T B 1992 *Binary Alloy Phase Diagrams, ASM International* (Metals Park, OH)

[166] Villars P, Cenzual K, Daams J L C, Hulliger F, Massalski T B, Okamoto H, Osaki K, Prince A and Iwata S 2003 *Binaries Edition, ASM International* (Metal Park, OH)

[167] Omuro K, Miura H and Ogawa H 1994 *Mat. Sci. Eng. A* **181** 1281

[168] Lamouroux E, Serp P, Kihn Y and Kalck P 2007 *Appl. Catalysis A* **323** 162

[169] Kanzow H and Ding A 1999 *Phys. Rev. B* **60** 11180

[170] Francis G P and Payne M C 1990 *J. Phys.: Condens. Matter* **2** 4395

[171] Bolton K, Ding F, Borjesson A, Zhu W, Duan H, Rosen A, Harutyunyan A R and Curtarolo S 2008 *Nanoscience* in press

[172] Niu Z and Fang Y 2006 *J. Cryst. Growth* **297** 228

[173] Rivlin V G 1985 *Int. Metals Rev.* **30** 109

[174] Ettmeyer P and Suchentrunk R 1970 *Monatsh. Chem.* **101** 1098

[175] Kuo K 1953 *Acta. Metall.* **1** 301

[176] Dyson D J and Andrews K W 1964 *J. Iron Steel Inst.* **202** 325

[177] Kuo K 1953 *J. Iron Steel Inst.* **173** 363

[178] Krainer H 1950 *Arch. Eisenhuttenwes.* **21** 39

[179] Pearson W B 1958 1967 *A Handbook of lattice spacings and structures of metals and alloys* **Vol. 1,2** (Oxford, Pergamon)

[180] Janovec J, Svoboda M, Vyrostkova A and Kroupa A 2005 *Mat. Sc. Eng. A* **402** 288

Biography

The author was born in May 5th, 1978 in a Javanese village 8 miles southwest of Solo, Central Java, Indonesia. He is the last(fourth) child of Ladiya (father) and Sri Suratmi (mother). His father was an elementary school teacher and his mother is a devoted house wife. Prior to attending college education, the author won the third award in the International Physics Olympiad 1996 in Norway. The author received a B.S. degree from Institut Teknologi Bandung, Indonesia, in Electrical Engineering in 2000. In the Fall of 2000, he went to Florida State University on a research assistantship from the Physics department in which he completed a M.S. degree in 2004. In Summer 2004, he received a research assitantship to pursue a doctoral degree in Mechanical Engineering and Materials Science department from Duke University under the advisory of Dr. Stefano Curtarolo. He completed his PhD work in computational materials science in Spring 2008. In addition, he received a Graduate Certificate degree in Computational Science, Engineering, and Medicine, in Spring 2008 also from Duke University.

List of publications:

- Diehl R D, Setyawan W and Curtarolo S 2008 *J. Phys.: Cond. Mat.* in press
- Harutyunyan A R, Awasthi N, Jiang A, Setyawan W, Mora E, Tokune T, Bolton K and Curtarolo S 2008 *Phys. Rev. Lett.* inpress
- Curtarolo S, Awasthi N, Setyawan W, Li N, Jiang A, Tan T Y, Mora E, Bolton K and Harutyunyan A T 2008 *Proc. of Comp. Simul. Studies in Cond. Matt. Phys.* **XXI** Eds Landau D P, Lewis S P and Schuttler H-B (Springer, Berlin, Heidelberg)
- Setyawan W, Diehl R D, Ferralis N, Cole M W and Curtarolo S 2007 *J. Phys.:*

Cond. Mat. **19** 016007

- Diehl R D, Setyawan W, Ferralis N, Trasca R, Cole M W and Curtarolo S 2007 *Phil. Mag.* **87** 2973
- Jiang A, Awasthi N, Kolmogorov A N, Setyawan W, Börjesson A, Bolton K, Harutyunyan A R and Curtarolo S 2007 *Phys. Rev. B* **75** 205426
- Setyawan W, Ferralis N, Diehl R D, Cole M W and Curtarolo S 2006 *Phys. Rev. B* **74** 125425
- Diehl R D, Ferralis N, Pussi K, Cole M W, Setyawan W and Curtarolo S 2006 *Phil. Mag.* **86** 863
- Curtarolo S, Setyawan W, Diehl R D, Ferralis N and Cole M W 2005 *Phys. Rev. Lett.* **95** 136104
- Rao S G, Huang L, Setyawan W and Hong S 2003 *Nature* **425** 36
- Setyawan W, Rao S G and Hong S 2002 *Mat. Res. Soc. Proc.* **NN** Fall
- Mumtaz A, Setyawan W and Shaheen S A 2002 *Phys. Rev. B* **65** 020503